3 Laser-Induced Thermal Processes: Heat Transfer, Generation of Stresses, Melting and Solidification, Vaporization, and Phase Explosion

Maxim V. Shugaev, Miao He, Yoann Levy, Alberto Mazzi, Antonio Miotello, Nadezhda M. Bulgakova, and Leonid V. Zhigilei

Contents

M. V. Shugaev · M. He · L. V. Zhigilei (✉)
Department of Materials Science and Engineering, University of Virginia, Charlottesville, VA, USA
e-mail: mvs9t@virginia.edu; mh5wz@virginia.edu; lz2n@virginia.edu

Y. Levy · N. M. Bulgakova (✉)
HiLASE Centre, Institute of Physics of the Czech Academy of Sciences, Dolní Břežany, Czech Republic
e-mail: levy@fzu.cz; bulgakova@fzu.cz

A. Mazzi
Center for Materials and Microsystems, Bruno Kessler Foundation, Povo (Trento), Italy
e-mail: mazzi@fbk.eu

A. Miotello (✉)
Department of Physics, University of Trento, Povo (Trento), Italy
e-mail: antonio.miotello@unitn.it

K. Sugioka (ed.), *Handbook of Laser Micro- and Nano-Engineering*,
https://doi.org/10.1007/978-3-030-63647-0_11

Abstract

The vast field of laser-enabled material synthesis, manufacturing, and processing to a large degree relies on the ability to induce and control a range of thermal processes triggered by the laser energy deposition as well as subsequent transport processes involving electrons and phonons. This chapter provides a review of the fundamental mechanisms, thermodynamic driving forces, and kinetics of thermal processes involved in laser-material interactions, with a particular focus on the far-from-equilibrium conditions characteristic of laser processing with short and ultrashort pulses. The peculiarities of the energy redistribution under conditions of electron-phonon nonequilibrium produced by an ultrashort laser excitation are discussed first and followed by analysis of the effect of dimensionality of the heat transfer at different stages of laser-materials interactions. The generation of strong thermoelastic stresses, which may lead to photomechanical spallation, generation of crystal defects, and activation of surface processes are then outlined, along with the implications of laser-induced stresses for practical applications. The discussion of laser-induced phase transformations starts from a brief review of experimental and computational results revealing the conditions leading to transition between the heterogeneous to homogeneous melting mechanisms. The implications of rapid melting and resolidification on microstructure and surface morphology of laser-processed surfaces are considered, and the conditions leading to chemical homogenization, amorphization, and generation of extreme densities of crystal defects are elaborated. The vaporization, which may take the form of evaporation from the surface or an explosive decomposition of superheated liquid (phase explosion), is discussed as the main process responsible for the material removal from the target, that is, for laser ablation. The mechanisms responsible for the generation of nanoparticles in the course of the phase explosion and through the condensation in the ablation plume are also considered and related to the particle size distributions.

Introduction

Thermal processes play a major role at all stages of laser-materials interactions and are responsible for both macro- and microscopic structural modification of materials. All processes that stem from the laser-induced material heating are referred here as thermal ones. They include *heat transfer* and thermally induced *phase transitions* including solid-solid ones, melting, vaporization, and solidification. In particular, the material removal from the target, that is, laser ablation, can proceed via normal

vaporization, phase explosion (or explosive boiling), and/or spallation of a layer from material surface caused by laser-generated stresses. The manifestation and dominance of one or another thermal process strongly depend on the rate at which the laser energy is deposited and equilibrates in the material. Figure 1 summarizes schematically the manifestation of some of the major laser-induced thermal processes versus pulse duration and laser fluence.

The actual boundaries for onsets of these processes strongly depend on thermophysical, optical, and mechanical properties of irradiated materials. For example, to produce damage of metals, to trigger their melting and ablation, relatively low laser energy densities are usually needed despite the high reflectivity of metal surfaces that reduces absorbed energy dose. On the other hand, wide-bandgap inorganic dielectrics and polymers, though being low reflecting materials, require considerably larger laser fluences compared to metals in order to achieve their melting and/or ablation. To learn more on specific material responses to pulsed laser irradiation, we refer the readers to the book by Bäuerle (2000) and other chapters in this handbook.

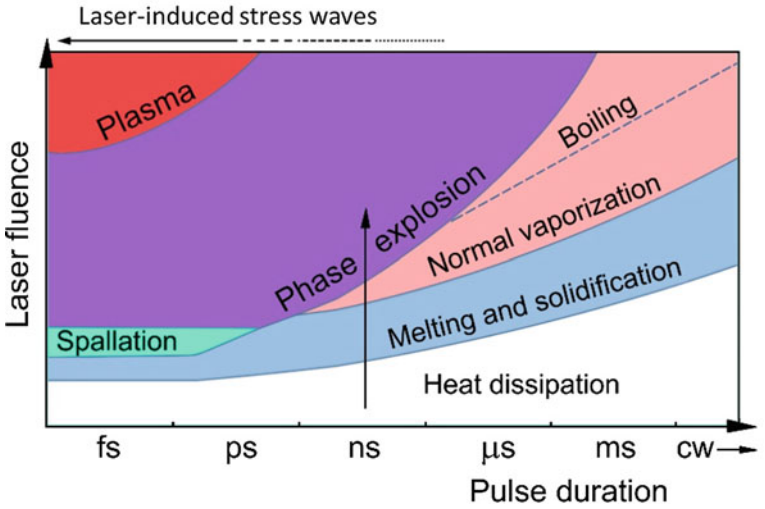

Fig. 1 Schematic diagram illustrating manifestation of thermal processes at laser fluences typical for material processing as a function of pulse duration. The lines separating different regions in the diagram mark the onset of different processes upon an increase of the laser fluence or shortening of the pulse duration. The lines for melting, spallation, and phase explosion correspond to relatively sharp thresholds for the onset of the corresponding processes, while the lines for vaporization and plasma formation are defined at a qualitative level and correspond to the conditions when vaporization makes a significant contribution to the material ejection and a substantial degree of ionization is reached in the ablation plume, respectively. Vertical arrow illustrates that, under a certain pulse duration, a laser-irradiated material can undergo a cascade of processes when the irradiation dose increases with time. As an example, during the irradiation by a single nanosecond laser pulse, a material can heat up, melt, start to vaporize, and experience phase explosion. The arrow on the top pointing to the left shows that laser-induced dynamic stresses are higher for shorter pulses due to the stress confinement and weaken for longer pulses

In Fig. 1, we would like to draw attention to the variety of thermal processes, which can occur *sequentially* during/after a single-shot laser irradiation of a particular spot on the material surface. For example, a metal irradiated by a nanosecond laser pulse can be heated to the melting point by the front part of the pulse, after which it can undergo melting, with corresponding transformation of some of the deposited energy to the latent heat of fusion, followed by vaporization of atoms from the surface (direct light-induced sublimation may also occur prior to melting). Furthermore, at a sufficiently high laser energy, melting and surface vaporization can be followed by an explosive homogeneous boiling of a surface region of the target overheated up to the limit of thermodynamic stability of the molten material, corresponding to the phase explosion mechanism of ablation discussed in section "Liquid-Vapor Transformations" of this chapter. This cascade of processes is shown in Fig. 1 by the vertical arrow.

It must also be underlined that, due to spatially inhomogeneous profile of majority of laser beams, different thermal processes may emerge simultaneously in different parts of a laser irradiation spot. As an example, we can consider a "mosaic" representation of the results of molecular dynamics (MD) simulations of an Al target irradiated by 100 fs laser pulses (Gaussian spatial profile) at different local laser fluences used for representation of the laser-induced processes at the scale of the whole laser spot (Wu and Zhigilei 2014), shown in Fig. 2. The material in the middle of the irradiation spot, where laser intensity is the largest, undergoes an explosive decomposition into a mixture of atoms and clusters/nanoparticles, while at the periphery of the irradiation spot the local conditions correspond to photomechanical spallation or simply melting and resolidification of the surface.

Due to the complex and multifaceted nature of the laser-induced processes triggered by laser irradiation at different spatial and temporal scales, after more than 50 years of intensive studies of laser-matter interactions, the complete control over material processing has not yet been achieved, while further investigations are inspired by new discoveries.

In this chapter, we provide a brief overview of the cascade of thermal processes in laser materials interactions. We mostly focus on ultrashort (femto- and picosecond) laser pulse action on metals and specify longer pulses and other materials where it is necessary. We start from considering the redistribution of the laser-deposited energy by the heat conduction in section "Laser Energy Deposition and Redistribution." The laser-induced stresses, which may lead to photomechanical spallation, generation of crystal defects, and activation of surface processes are discussed in section "Laser-Induced Stresses and Stress Waves." In section "Laser-Induced Melting and Resolidification," we address rapid melting and resolidification, which produce microstructural changes in the surface region of the irradiated target. Material ablation, which may take the form of surface vaporization, normal boiling, or an explosive decomposition of superheated matter, is discussed in section "Liquid-Vapor Transformations." The generation of nanoparticles in the course of the explosive boiling or through the condensation in the ablation plume is considered in section "Nanoparticle Formation by Pulsed Laser Ablation," and concluding remarks discussing the interconnections between different thermal processes, as

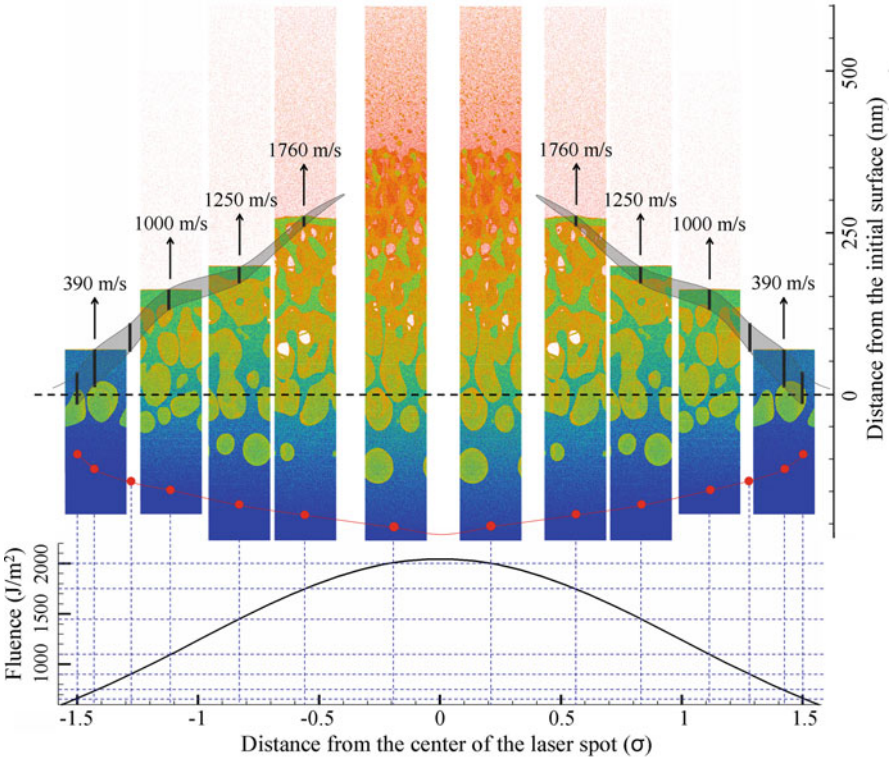

Fig. 2 The integral visual picture of melting, generation of subsurface voids, and material ejection from an Al target irradiated by a 100 fs laser pulse. The laser beam has a Gaussian spatial profile with the standard deviation σ and a peak absorbed laser fluence of 2050 J/m^2. The snapshots are taken at the same moment of time, 150 ps after the laser pulse, and are aligned with locations within the laser spot that correspond to the values of local fluence used in the simulations, as shown in the lower part of the panel. The atoms in the snapshots are colored by their potential energy, from blue for low energy atoms in the bulk of the target to red for the vapor-phase atoms. The red dots connected by the red line mark the location of the liquid-crystal interface. (The figure is reprinted with permission from Wu and Zhigilei (2014))

well as their interplay in practical applications targeting surface processing, microfabrication, and nanoparticle synthesis are provided in section "Concluding Remarks."

Laser Energy Deposition and Redistribution

As discussed in detail in the chapter of this handbook focused on laser energy deposition (Balling 2020), the energy of a laser irradiation couples mainly to electrons of the irradiated material. In metals, the presence of conduction band electrons enables the direct absorption of laser energy by electrons undergoing collisions with lattice ions,

that is, by inverse bremsstrahlung. Strictly speaking, conduction electrons in metals are always moving in the electric field of the surrounding lattice ions and, hence, they can absorb photons at any moment in a bremsstrahlung-like process. In semiconductors and dielectrics, electrons have to be excited across the bandgap before they can directly absorb photons. In any case, the ultrashort pulse laser irradiation produces a state of strong electron-phonon nonequilibrium that can be described by the two-temperature model (TTM) (Anisimov et al. 1974). In this model, two coupled heat diffusion equations for conduction band electron and phononic subsystems are introduced, and the initial energy redistribution by nonthermal (ballistic) electrons prior to the establishment of electron temperature (i.e., within $\sim 10^{-13}$ s) is usually accounted for through appropriate modification of the source term representing the laser energy deposition to the electronic subsystem (Ivanov and Zhigilei 2003a; Wellershoff et al. 1999). An additional equation accounting for the evolution of the electron density in the conduction band enables description of the evolution of the exited states in semiconductors and dielectrics (Lipp et al. 2014; Bulgakova et al. 2005). Details of these models are discussed in another chapter of this handbook (Balling 2020), and in this section, we limit our discussion to analysis of the implications of the electron-phonon nonequilibrium on the energy redistribution that follows the ultrashort laser excitation. We also provide a brief discussion of the dimensionality of the heat transfer that governs the energy redistribution in targets of different geometries at different stages of laser materials interactions.

Peculiarity of Energy Redistribution in Two-Temperature State

The state of the electron-phonon nonequilibrium generated in a target material by a short pulse laser excitation can have important implications on the initial redistribution of energy deposited by the laser pulse. These implications are related to different roles the atomic vibrations (phonons) and conduction band electrons are playing in thermal energy storage and transport: the heat capacity of all materials is largely defined by phonons, whereas the electrons are absorbing laser energy and are serving as dominant thermal energy carriers in metals. The strength of the electron-phonon interactions not only defines the rate of energy transfer from the excited electrons to phonons but, to a large extent, also controls the energy redistribution from the regions where it is deposited by the laser.

One of the clearest manifestations of the energy channeling in the state of electron-phonon nonequilibrium is provided by laser interactions with metal multilayers composed of materials with different strength of electron-phonon coupling. In cases when the top layer of the target exposed to the laser irradiation is made of a metal with weaker electron-phonon coupling, the electrons excited by the laser light in the top layer can rapidly transfer energy to the electrons in the underlying layer, where a rapid equilibration with phonons provides conditions for subsurface accumulation of the deposited energy. The first experimental evidence of the importance of the two-temperature state consideration was provided by time-resolved pump-probe thermoreflectivity measurements performed for Au-Cr layered system (Qiu

et al. 1994). It was found that the changes in the surface reflectivity observed in the experiments could only be explained by TTM calculations (Qiu and Tien 1994) that predicted much stronger heating of a subsurface Cr layer even though the initial laser energy deposition was largely confined within the top Au layer, Fig. 3. As can be seen from Fig. 3b, the electron temperature equilibrates in the multilayered system within the first picosecond after the laser pulse. At the same time, the lattice temperature increase during the first picoseconds is mostly limited to the Cr layer, Fig. 3c, thus producing the effective energy localization within this layer. Similar effect of the energy localization within a layer with stronger electron-phonon coupling has been used to explain the results of thermoreflectivity measurements

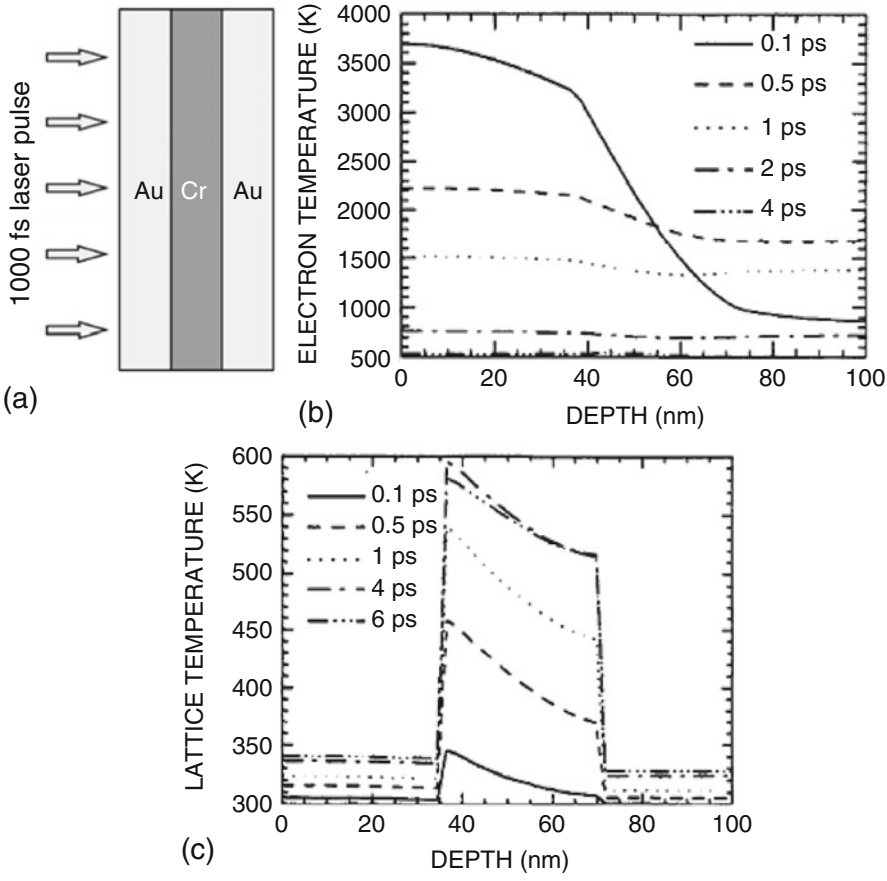

Fig. 3 The results of TTM calculations performed for 34 nm Au – 33 nm Cr – 33 nm Au three-layer film irradiated by a 100 fs pulse at a wavelength of 630 nm and a fluence of 500 J/m^2. A schematic of the computational setup is shown in (**a**), and distributions of electron and lattice temperatures along the depth of the irradiated target are depicted in (**b**) and (**c**), respectively. The results of pump-probe thermo-reflectivity measurements reported in Qiu et al. (1994) could only be explained if the preferential heating of the subsurface Cr layer is accounted for. (Panels (**b**, **c**) of the figure are adapted and reprinted with permission from Qiu and Tien (1994))

for Pt-Au/Cu layered systems (Choi et al. 2014; Wang and Cahill 2012) and, more recently, femtosecond X-ray diffraction probing of transient lattice deformation in Au-Ni bilayers (Pudell et al. 2018).

At higher laser fluences, above the threshold for target modification, the redistribution of the energy during the time of electron-phonon nonequilibrium may strongly affect the laser-induced structural and phase transformations. This has been demonstrated in atomistic simulations performed for Au and Ag films deposited on a bulk Cu substrate using a computational method combining TTM with a classical molecular dynamics (MD) technique (Wu et al. 2011; Thomas et al. 2009). The TTM-MD simulations predicted subsurface heating and melting of the Cu substrate under irradiation conditions when the overlaying Au/Ag films still retain their original crystalline structure. In the case of Ag-Cu system, the transient subsurface melting and resolidification is predicted to produce a complex structure in the interfacial region. This structure features a stacking fault pyramid structure of the mismatched interface separated from the Ag–Cu mixing region by an intermediate pseudomorphic bcc Cu layer (Wu et al. 2011).

For thin film bilayers, the effect of the subsurface melting is illustrated in Fig. 4 by the results of a TTM-MD simulation performed for a film consisting of two 50-nm-thick layers of Ag and Cu deposited on a silica glass substrate and irradiated by a 60 fs laser pulse (Naghilou et al. 2019). The higher strength of the electron-phonon coupling in Cu, as compared to Ag (Wu et al. 2011; Lin et al. 2008a), results in a preferential subsurface heating of the Cu layer, producing the electron and lattice temperatures profiles, Fig. 4c, d, similar to those discussed above and illustrated by Fig. 3 for a Au-Cr layered system. In contrast to the simulation of the Au-Cr system, the fluence used in the simulation of the Ag-Cu bilayer is sufficient to melt the Cu layer. Indeed, while the electron temperature equalizes within the two layers during the first 2 ps after the laser pulse, Fig. 4c, the difference in the lattice temperature increases with time, Fig. 4d. By 6 ps, the temperature of Cu exceeds 2000 K and causes rapid melting of the layer, while Ag remains solid at a temperature below 1000 K. This observation suggests a possible design of a layered surface structure capable of channeling the energy to the subsurface region of an irradiated target to prevent thermal damage of a heat-sensitive optically transparent coating material under conditions of high-power laser irradiation.

Another consequence of the rapid heating of the Cu layer is the generation of strong compressive pressure that reaches the level of 13 GPa just before the onset of the homogeneous melting of the layer, Fig. 4b. The buildup of high pressure in the subsurface layer triggers complex dynamics of the pressure relaxation, Fig. 4b, which, depending on irradiation conditions, may lead to the formation of internal voids, spallation of the film, or generation of a microbump by a tightly focused laser beam (Naghilou et al. 2019). The effects associated with the laser-induced stresses are discussed in section "Laser-Induced Stresses and Stress Waves," and here we just note that the stress waves propagating away from the region of laser energy deposition can also make a contribution, albeit not a major one, to the energy redistribution. For example, the results of a TTM-MD simulation of a bulk Ni target irradiated by a picosecond laser pulse in the regime of surface melting and

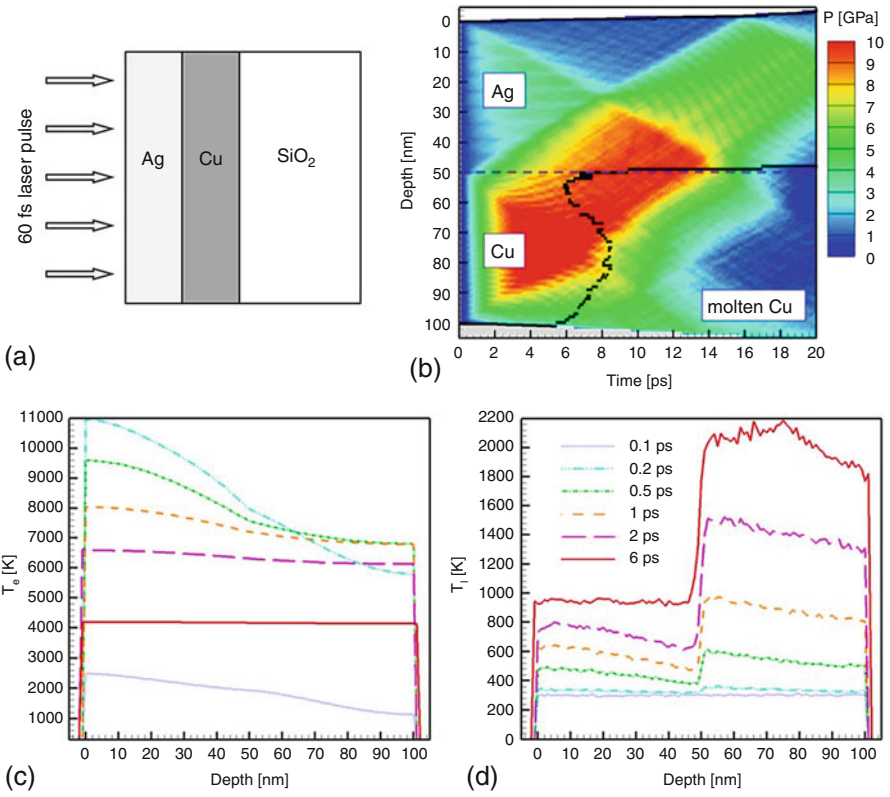

Fig. 4 The results of a TTM-MD simulation of a film consisting of two 50-nm-thick layers of Ag and Cu deposited on a silica glass substrate and irradiated by a 60 fs laser pulse at an absorbed fluence of 500 J/m^2. The schematic of the system is provided in (**a**), a contour plot of spatial and temporal evolution of pressure is shown in (**b**), and distributions of electron and lattice temperatures are plotted in (**c**) and (**d**), respectively. In (**c**) and (**d**), similar lines correspond to the same moments of time marked in (**d**). In (**b**), the dashed line marks the location of the interface between Ag and Cu layers, and the solid line shows the position of the solid-liquid interface. The results of computational and experimental study of laser interaction with Ag-Cu bilayers are reported in Naghilou et al. (2019)

resolidification (Zhigilei and Ivanov 2005) suggest that the laser-induced thermoelastic wave can carry away about 5% of the total energy deposited by the laser pulse, while another 8% of the deposited energy transiently transforms into the energy of quasi-static thermoelastic stresses associated with temperature gradient produced in the surface region of the target.

Contribution of Phonon Thermal Conductivity in Metals

Since the electronic contribution to the thermal conductivity of metals is usually 1–2 orders of magnitude higher than the phononic one (Wang et al. 2016), in most cases it is

reasonable to assume that the heat transfer occurs within the electronic subsystem, while the evolution of lattice temperature is governed by the electron-phonon coupling (Shugaev and Bulgakova 2010). The phonon heat conduction, however, can still play an important role under certain conditions and may have practical implications for the final outcome of short pulse laser processing. In particular, in short pulse laser interactions with thin films, multilayers, or surfaces covered by dielectric overlayers, the phononic contribution to the thermal conductivity may play an essential role, especially for metals with weak electron-phonon coupling, such as Ag or Au. For example, an evidence of a substantial contribution of the phonon heat transport has been revealed in an X-ray diffraction probing of the laser energy equilibration in a nanoscale Au-Ni bilayer deposited on a MgO substrate (Pudell et al. 2018).

Another example of a practical implication of the phonon thermal conductivity on laser material modification is illustrated in Fig. 5, showing the results of atomistic modeling of 10 ps laser irradiation of a Ag target covered by a silica overlayer in the regime of melting and resolidification (Shugaev et al. 2017a). The temperature profiles in Fig. 5b are shown for a time of 100 ps after the laser pulse and, due to the rapid electron heat transfer, an almost uniform electron temperature distribution is established within top 100 nm part of the target by this time. The vibrational temperature (called here the "lattice" temperature following the convention of TTM, even though the surface region is melted), however, is affected by the melting process, dynamic relaxation of laser-induced stresses, and, in the vicinity of the silica overlayer, by the phonon heat transfer to the overlayer. In particular, the temperature drop by ~$0.3T_m$ within 5–10 nm from the Ag-silica interface is mainly defined by the phonon thermal conductivity. The spatial scale of a region affected by the phononic heat transfer can be estimated as $l_{ph} \sim \sqrt{k_{ph}/g}$, where k_{ph} is the phonon thermal conductivity and g is the electron-phonon coupling factor. Within this region, the heat transfer by the phonon thermal conductivity is counterbalancing the energy transfer due to the electron-phonon coupling, thus creating a quasi-steady-state gap between the electron and phonon temperatures. The temperature gap and the spatial scale of the phononically cooled region are particularly large for metals with weak electron-phonon coupling. Note that a similar state of quasi-steady electron-phonon nonequilibrium can also be created at a rapidly propagating melting (Ivanov and Zhigilei 2007) or solidification (Chan et al. 2009) front. In such situations, the release or absorption of the latent heat of melting can produce a local temperature drop or spike that cannot be eliminated by the energy transfer from electrons due to the finite time of electron-phonon equilibration.

While the cooling due to the phononic heat transfer to the cold overlayer only affects about 10-nm-thick layer of the metal target, Fig. 5b, it can have important practical implications. In particular, as shown in Shugaev et al. (2017a), the presence of a thin region where the temperature remains below the melting point of the target material can stabilize small crystallites adjacent to the overlayer, Fig. 5c, and enable fast epitaxial regrowth from these crystallites as soon as the temperature in the target drops below T_m. The crystallization proceeding from the survived crystallites prevents the homogeneous nucleation of randomly oriented crystallites and results in the formation of a nanocrystalline interfacial region with small grain misorientation,

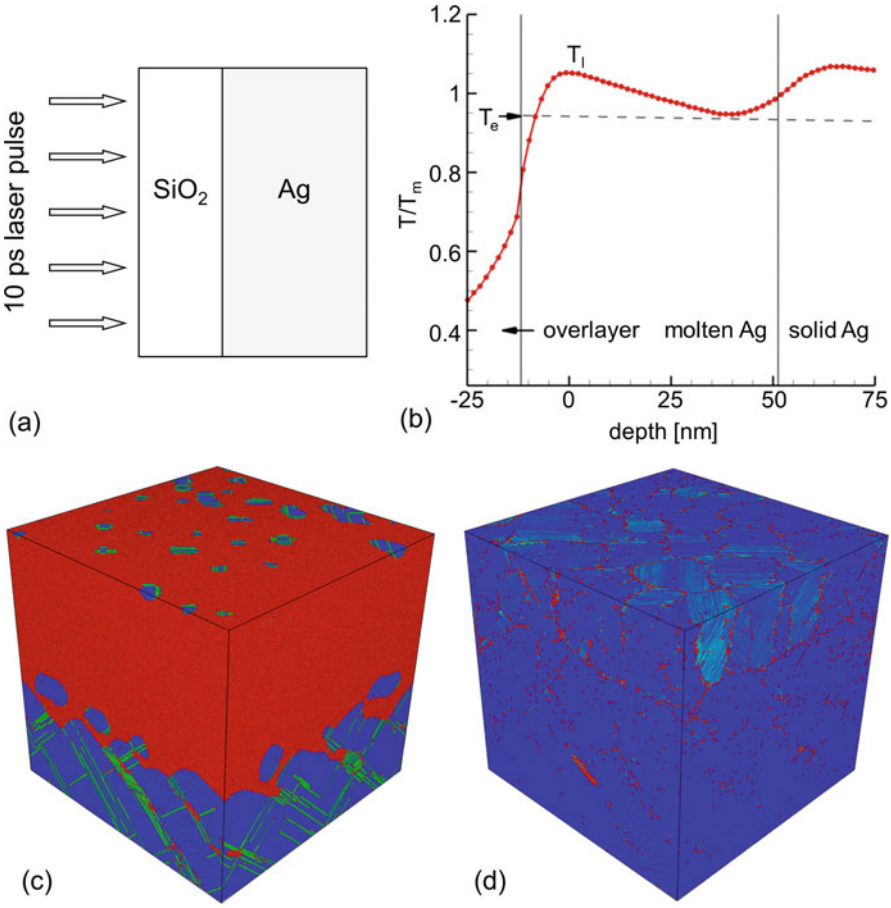

Fig. 5 The results of a TTM-MD simulation of 10 ps laser pulse irradiation of a bulk Ag target covered by a transparent silica glass overlayer. The schematic of the system is provided in (**a**), the electron and lattice temperature distributions at a time of 100 ps after the laser pulse are shown in (**b**), and snapshots of atomic configurations taken at a time when the maximum melting depth is reached, 300 ps, and after complete resolidification of the surface region, 1100 ps, are shown in (**c**) and (**d**), respectively. In (**b**), the electron and lattice temperature profiles are depicted by black dashed and red solid lines, respectively. In (**c**), the atoms are colored by their local structural environment, so that the molten part of the target is shown by red color, and the single and double green layers on a blue background correspond to twin boundaries and stacking faults in the fcc structure. In (**d**), the atoms are colored by the smallest angle between one of the ⟨111⟩ directions of the original fcc lattice and a ⟨111⟩ direction in the corresponding grain, with the blue to red color scale corresponding to misorientation angles ranging from 0° to 30°. The silica overlayer is not shown in (**c**, **d**). (Panels (**b**–**d**) of the figure are reprinted with permission from Shugaev et al. (2017a))

Fig. 5d. A similar resolidification process proceeding from crystalline parts of $Ge_2Sb_2Te_5$ (GST) film adjacent to Si substrate has been suggested by Møller et al. (2018) to explain the formation of long columnar grains in films experiencing melting and resolidification induced by 50 ps laser irradiation.

Effect of Heat Transfer Dimensionality

An important factor defining the laser energy redistribution is the dimensionality of the space domain where the heat transfer process occurs. Some of the typical laser irradiation conditions are illustrated in Fig. 6 for a bulk target and a thin film deposited on an optically transparent substrate. The laser intensity distribution within the laser spot, commonly assumed to have a Gaussian shape, can create a lateral component of the temperature gradient directed parallel to the irradiated surface. For highly absorbing materials, such as metals or semiconductors irradiated at photon energies exceeding the bandgap, however, the laser absorption depth is usually much smaller than the size of the laser spot, and the heat transfer related to the lateral component of the temperature gradient can be neglected during the initial stage of the energy redistribution. Indeed, the analysis of thermodynamic conditions created in the surface region of an irradiated target is often based on one-dimensional (1D) modeling of the laser energy deposition and heat transfer (Ivanov and Zhigilei 2003a; Thomas et al. 2009; Naghilou et al. 2019; Chan et al. 2009; Møller et al. 2018; Leveugle et al. 2004; Zhigilei et al. 2009; Karim et al. 2012; Byskov-Nielsen et al. 2011). The processes occurring at the scale of entire laser spot can then be evaluated through a "mosaic" approach based on combining the results of a series of quasi-1D simulations performed for a range of local fluences chosen from the laser beam profile (Wu and Zhigilei 2014; Shugaev et al. 2018), as briefly described above and illustrated by Fig. 2.

From the point of view of heat diffusion, the range of applicability of 1D model can be evaluated by considering the characteristic length scale of thermal diffusion, $l_{th} = \sqrt{Ak\tau/c}$ during a time of interest τ, where k and c are the thermal conductivity and heat capacity of the material, respectively, and A is a constant defined by the geometry of the absorbing region. Using the values of k and c typical for metals, we can estimate the heat diffusion length l_{th}~ 0.1–1 μm for a typical time required for melting and solidification of a surface region of a target irradiated by an ultrashort laser pulse, τ ~ 1–10 ns (Chan et al. 2009; Wu et al. 2015; Wu and Zhigilei 2016; Sedao et al. 2016). The 1D treatment, therefore, is suitable for analysis of thermodynamic conditions that may lead to surface microstructure and morphology

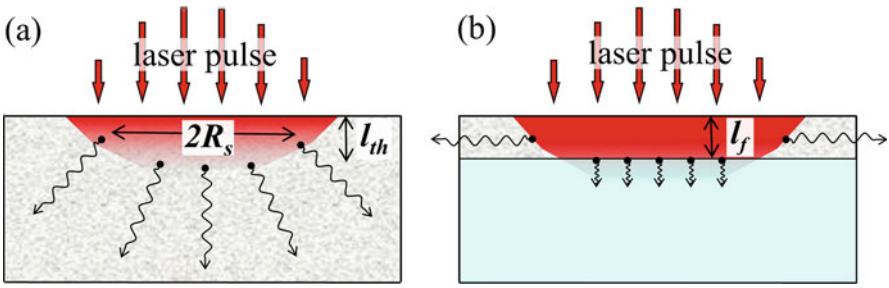

Fig. 6 Schematic representation of the laser energy deposition and redistribution in a strongly absorbing bulk target (**a**) and a film deposited on a substrate (**b**)

modification in ultrashort pulse laser processing when l_{th} is much smaller than the radius of the laser spot, R_s in Fig. 6a, which commonly is in the range from tens to hundreds of micrometers.

The 1D approximation fails, however, when l_{th} becomes comparable or even larger than R_s, for example, in cases of the laser energy deposition by a tightly focused laser beams (Naghilou et al. 2019; Pronko et al. 1995; Koch et al. 2005; Yoshiki et al. 2003; Kuznetsov et al. 2012; Ivanov et al. 2010) or energy localization though field enhancement in the vicinity of a tip of a scanning probe microscope (Hwang et al. 2009a; Huber et al. 2014) or a deposited nano/microparticle (Huang et al. 2003; Lu and Chen 2003). Even when the condition $R_s \gg l_{th}$ is satisfied, the two- or three-dimensional (2D or 3D) consideration of the heat transfer may be required by the uneven energy deposition due to the presence of surface defects or morphological features, as well as the interference of the incident laser wave and a surface scattered electromagnetic wave. The latter effect can create a periodic pattern of the absorbed laser energy along the irradiated surface (Sipe et al. 1983; Bonse et al. 2009) and lead to the formation of laser-induced periodic surface structures (LIPSS) (Buividas et al. 2014; Bonse et al. 2017; Reif et al. 2008), the phenomena where the 2D heat and mass transfer are essential (Shugaev et al. 2017b, 2018; Levy et al. 2016; Gurevich et al. 2017).

The dimensionality of the heat transfer in laser-materials interactions may also be affected by the finite size of the absorbing components of the target, for example, in the case of thin films and multilayers already discussed in section "Peculiarity of Energy Redistribution in Two-Temperature State." When l_{th} becomes comparable to the thickness of an irradiated film, l_f in Fig. 6b, the energy deposited by a laser pulse gets confined within the film, and the two channels of heat transfer and cooling of the film are the 2D heat transfer in the lateral directions and the heat transfer (1D for large R_s) to the substrate. Even though the latter can be hampered by the low thermal conductivity of the substrate and thermal boundary resistance of the film-substrate interface (Hopkins et al. 2007; Stevens et al. 2007; Cheaito et al. 2015), the contribution of this cooling channel may become dominant for sufficiently large R_s and, in particular, can control the kinetics of film resolidification and the final phase state of the resolidified material (Ehrler et al. 2018; Polushkin et al. 2018).

Very high cooling rate can, in principle, be realized in the case of short pulse laser irradiation of an absorbing nanoparticle embedded in a transparent medium, where the initial concentration of energy deposited by the laser pulse in a submicron region can be followed by an effective three-dimensional heat transfer into the medium, as schematically illustrated in Fig. 7a. In systems with large mismatch of thermal properties between the nanoparticle materials and the surrounding medium, for example, a metal nanoparticle in a liquid, the cooling of the nanoparticle can be strongly affected by the thermal resistance at the nanoparticle – medium interface, which may result in a substantial temperature drop at the interface (Baffou and Rigneault 2011; Giammanco et al. 2010; Siems et al. 2011; Hashimoto et al. 2012). Superheating of the surrounding liquid and generation of a vapor bubble around the nanoparticle can further slowdown the nanoparticle cooling process (Siems et al. 2011; Hashimoto et al. 2012; Volkov et al. 2007; Pustovalov et al. 2008). For very

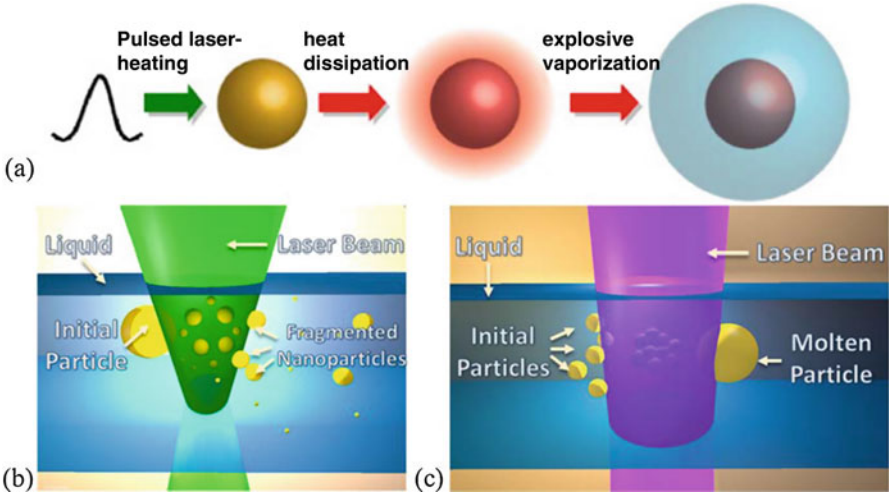

Fig. 7 Schematic representation of laser interaction with a nanoparticle in a liquid environment (**a**) and applications of this process to laser fragmentation in liquids (**b**) and laser melting in liquids (**c**). (Panels (**a**) and (**b**,**c**) are reprinted with permission from Hashimoto et al. (2012) and Zhang et al. (2017), respectively)

small (a few nanometers in diameter) nanoparticles, the formation of an insulating vapor layer, however, can be suppressed by the high curvature of the nanoparticle-liquid interface, as has been demonstrated in MD simulations of heat transfer from hot nanoparticles to a surrounding liquid (Merabia et al. 2009a, b). As a result, very high heat fluxes from nanoparticles to the environment can be sustained, leading to extreme cooling rates experienced by the nanoparticles. In particular, large-scale atomistic simulations of laser ablation in a liquid environment predicted that molten metal droplets injected into a cold liquid environment by the ablation process can be rapidly quenched, strongly undercooled, and undergo rapid solidification into highly nonequilibrium structures (Shih et al. 2017, 2018; Hu et al. 2010). Direct laser interaction with nanoparticles is in the core of a number of current and emerging applications, ranging from selective killing of cancer cells (Pitsillides et al. 2003; Lapotko et al. 2006) or bacteria (Zharov et al. 2006) to biological imaging (Lemaster and Jokerst 2017) and drug delivery (Skirtach et al. 2005), and to laser processing of colloidal solutions of nanoparticles (Giammanco et al. 2010; Hashimoto et al. 2012; Wang et al. 2010; Zhang et al. 2017; Ziefuß et al. 2018). The latter includes laser fragmentation in liquid (Giammanco et al. 2010; Hashimoto et al. 2012; Zhang et al. 2017; Ziefuß et al. 2018), where larger nanoparticles are fragmented to produce a population of smaller nanoparticles with a narrow size distribution, Fig. 7b, and laser melting in liquid (Wang et al. 2010; Zhang et al. 2017), where melting and partial vaporization of nanoparticles is used to change the size, shape, and composition of the colloidal nanoparticles, Fig. 7c.

While the dimensionality of the system is discussed above based on the heat transfer alone, other processes, such as dynamic relaxation of laser-induced stresses

and emission of the stress waves, melting and resolidification, hydrodynamic flow and redistribution/expulsion of molten material, ejection and expansion of the ablation plume, may have their own characteristic dimensionality. Moreover, the dimensionality of the laser-induced processes often changes with time, and the same processes should be considered as 1D, 2D, and/or 3D ones as they evolve following the laser excitation. The dimensionality may also change due to the appearance of spatial heterogeneities in an initially homogeneous material. For example, photomechanical spallation or phase explosion, discussed in sections "Photomechanical Spallation" and "Liquid-Vapor Transformations," involves the appearance of large density variations (subsurface voids, transient foamy structures of interconnected liquid regions, vapor-liquid mixture (Wu and Zhigilei 2014, 2016; Wu et al. 2015; Shugaev et al. 2017b; Shih et al. 2017; Zhigilei 2003; Zhigilei and Garrison 2000; Abou-Saleh et al. 2018)) on the scale of tens to hundreds of nanometers. While the overall material flow in this case may still retain its 1D nature, the fundamental understanding of processes responsible for material disintegration/damage requires a fully-3D mesoscopic treatment of the transient material dynamics.

Laser-Induced Stresses and Stress Waves

Ultrashort laser pulse energy deposition leads to a rapid localized heating of the target material and, unavoidably, results in the generation of mechanical stresses. The laser-induced stresses can be grouped into three categories: (1) dynamic transient stresses and stress waves generated due to the condition of stress confinement, (2) long-term quasi-static thermo-elastic stresses related to the temperature gradients, and (3) residual stresses due to the laser-induced structural changes (defects) in the material. In this section, we provide a brief overview of the main mechanisms responsible for generation and relaxation of laser-induced stresses.

Generation of Laser Induced Stresses

The fast rate of energy deposition by short laser pulses leads to ultrafast heating and generation of compressive stresses. The laser-generated stresses are particularly high in the regime of stress confinement (Leveugle et al. 2004; Zhigilei and Garrison 2000; Paltauf and Dyer 2003), when the time of the laser heating (defined by the laser pulse duration, τ_p, or the time of the electron-phonon equilibration, $\tau_{e\text{-}ph}$, whichever is longer) is shorter than the time required for the mechanical relaxation (expansion) of the heated volume, that is, $\max\{\tau_p, \tau_{e\text{-}ph}\} \leq L_p/C_s$, where C_s is the speed of sound in the target material and L_p is the effective depth of the laser energy deposition. The latter is equal to either the optical penetration depth or, in the case of metals, the depth of diffusive/ballistic energy transport during the time of the electron–phonon equilibration, see section "Laser Energy Deposition and Redistribution" and a chapter on laser coupling and relaxation of the absorbed energy of this handbook (Balling 2020) for more details.

As an example of the laser-induced generation of stresses, let us consider temperature and pressure evolution in a bulk Ni target irradiated by a femtosecond laser pulse, shown in the form of contour plots in Fig. 8. During the laser irradiation, the laser energy is first absorbed by conduction band electrons and then transferred to phonons during the electron-phonon equilibration, which occurs on the picosecond timescale. With $\tau_{e\text{-}ph} \approx 10$ ps (Lin and Zhigilei 2007a), $L_p \approx 50$ nm (Ivanov and Zhigilei 2004), and $C_s \approx 5080$ m/s (Billings and Gray 1972), the condition for a partial stress confinement is satisfied, and the laser heating leads to the buildup of high compressive stresses in the surface region of the target, Fig. 8b. Rapid homogeneous melting of the surface region (see section "Mechanisms and Time Scales of Melting") adds to the compression as the molten material has a higher specific volume, as can be seen from a secondary spike in the compressive stresses appearing upon melting in Fig. 8b. The strong pressure gradient drives the emission of an intense compressive wave propagating into the bulk of the target, while the expansion of the material towards the free surface creates an unloading tensile component of the stress wave which follows the compressive one (Fig. 8b). The tensile stresses associated with the unloading wave can induce cavitation in the molten part of the target followed by photomechanical spallation (Leveugle et al. 2004; Zhigilei and Garrison 2000; Paltauf and Dyer 2003) (section "Photomechanical Spallation") as well as emission of dislocations from the solid-liquid interface (Shugaev et al. 2018; Wu et al. 2014; Karim et al. 2014) (see section "Stress-Induced Generation of Crystal Defects"). These processes lead to a reduction of the amplitude of the tensile component of the stress wave. In addition, due to the acoustic impedance mismatch between the solid and molten states of the target material, the stress wave is partially reflected from the solid-liquid interface, as can be seen from Fig. 8b.

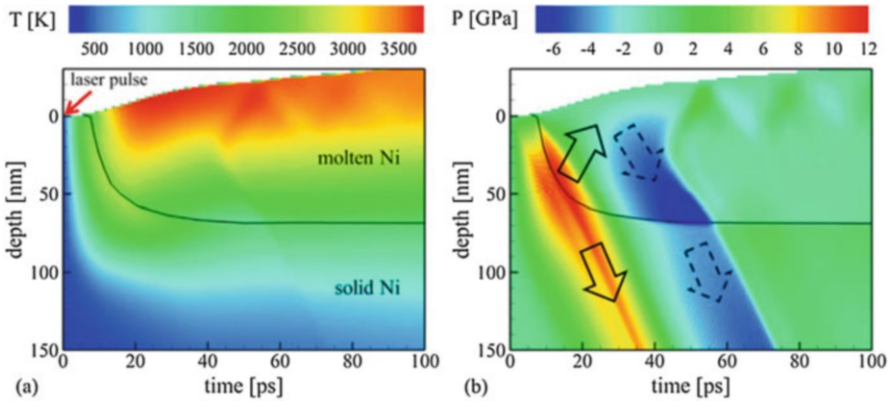

Fig. 8 Contour plots of temporal and spatial evolution of temperature (**a**) and pressure (**b**) in a bulk Ni target irradiated by a 50 fs laser pulse at an absorbed laser fluence of 1500 J/m^2, which is above the spallation threshold. Black line outlines the solid-liquid interface; solid and dashed black arrows show the direction of propagation of compressive and tensile stress waves. (The figure is adapted and reprinted with permission from Shugaev and Zhigilei (2019))

Following the initial dynamic relaxation of the laser-induced stresses, the pressure in the molten part of the target quickly relaxes down to zero. The thermoelastic stresses in the crystalline part of the target, however, cannot completely relax by uniaxial expansion in the direction normal to the free surface, while the lateral expansion of the heated part of the target is constrained by the surrounding material. As a result, some residual quasi-static compressive stresses are present below the crystal-liquid interface in Fig. 8b and remain in the target after complete resolidification of the surface region, until it is cooled to the original temperature.

The lateral compression of the crystalline part of the target can have important implications for the generation of the final microstructure, as it can increase the concentration of vacancies in the surface region of the target and facilitate generation of dislocations during the solidification. In general, both the dynamic relaxation of laser-induced stresses (stress waves) and the long-term quasi-static stresses can lead to the generation of subsurface voids (Wu et al. 2015; Savolainen et al. 2011; Ionin et al. 2011; Ashitkov et al. 2012; Starikov and Pisarev 2015) and contribute to the generation of a high density of crystal defects (Shugaev et al. 2018; Wu et al. 2014; Karim et al. 2014; Lin et al. 2008b), for example, through the emission of dislocations from the crystal-liquid interface at a time when the tensile component of the laser-induced stress wave passes through the interface (Shugaev et al. 2018; Wu et al. 2014; Karim et al. 2014). The presence of the defects may produce permanent residual stresses in the surface region of the target and strongly affect the properties of the surface processed by ultrashort pulse laser irradiation, as further discussed in section "Heterogeneous Melting" and a chapter of this handbook focused on microstructure modification (Vilar 2020).

Photomechanical Spallation

As mentioned in the previous section, the relaxation of laser-induced tensile stresses can cause nucleation of voids in the molten region, which can subsequently collapse, be trapped by the resolidification process leading to surface swelling (Wu et al. 2015; Savolainen et al. 2011) (more details can be found in another chapter of this handbook (Balling 2020)), or grow and coalesce leading to photomechanical spallation, that is, complete separation and removal of the liquid layer (Leveugle et al. 2004; Zhigilei and Garrison 2000; Paltauf and Dyer 2003). Although these processes have been extensively studied in large-scale atomistic simulations (Wu and Zhigilei 2014; Ivanov and Zhigilei 2003a; Leveugle et al. 2004; Zhigilei et al. 2009; Karim et al. 2012; Shugaev et al. 2018; Wu et al. 2014, 2015; Wu and Zhigilei 2016; Shih et al. 2017; Zhigilei and Garrison 2000; Abou-Saleh et al. 2018; Karim et al. 2014; Starikov and Pisarev 2015; Lorazo et al. 2006; Upadhyay et al. 2008; Gill-Comeau and Lewis 2011; Zhigilei et al. 2004), incorporation of the spallation process into continuum-level models remains challenging and requires special consideration. In this section, the fundamentals of cavitation in a molten material are discussed, and the threshold for the onset of cavitation is derived analytically and compared with predictions of molecular dynamics simulations.

The Gibbs free energy change due to appearance of a cavity of radius r in a molten material under tension can be expressed as $\Delta G = P_l V + \gamma_{lv} A$, where P_l and γ_{lv} are the pressure in the stretched liquid and the surface tension of liquid-vapor interface, $V = 4\pi r^3/3$ and $A = 4\pi r^2$ are the volume and surface area of the cavity, respectively. Since the magnitude of pressure variations induced in a target irradiated under conditions of stress confinement (see section "Generation of Laser-Induced Stresses" and Fig. 8b) is usually much larger than the vapor pressure inside the cavity, P_v, in a wide range of temperatures above the melting point of a target material, the contribution of the vapor pressure is neglected here to simplify the analysis. Thus, we consider the regime of photomechanical spallation, when the dominant driving force responsible for the appearance of the voids or cavities is the dynamic relaxation of the laser-induced stresses (see Leveugle et al. 2004 for the discussion of the terminology used to describe this process). As the temperature approaches the critical point, however, $P_l - P_v$ should be used in the free energy equation instead of P_l, and the release of vapor can drive the massive nucleation and growth of vapor bubbles even in the absence of any negative/tensile pressure. This scenario corresponds to the regime of "explosive boiling" or "phase explosion" that is considered in detail in section "Liquid-Vapor Transformations."

For a spherical cavity generated in the regime of photomechanical spallation, the critical radius and the free energy barrier for the onset of the cavitation can be obtained from the condition $d(\Delta G)/dr|_{r_c} = 0$, yielding $r_c = -2\gamma_{lv}/P_l$ and $G_0 = \Delta G(r_c) = 16\pi\gamma_{lv}^3/3P_l^2$. For a liquid under tension ($P_l < 0$), the rate of void nucleation can then be written as $R = R_0 \times \exp(-G_0/k_B T) = R_0 \times \exp\left(-16\pi\gamma_{lv}^3/3P_l{}^2 k_B T\right)$, where k_B and T are the Boltzmann constant and temperature. The prefactor R_0 is expressed in units of nuclei per second per cubic meter and can be estimated as $R_0 \approx k_B T/hV_a$ (Turnbull and Fisher 1949), where V_a is the atomic volume and h is Planck's constant.

For a typical metal, R_0 is on the order 10^{42} s^{-1} m^{-3}, and a more accurate consideration of the prefactor accounting for the number of surface atoms in the critical nucleus (Turnbull and Fisher 1949) increases R_0 up to 10^{43}–10^{44} s^{-1} m^{-3}. According to large scale atomistic simulations of laser-induced spallation of Al and Ag targets (Wu and Zhigilei 2014; Wu et al. 2015), the propagation of the unloading tensile wave through molten parts of the irradiated targets generates approximately 100 voids within a volume of about 100 × 100 × 50 nm^3 during 20 ps, which suggests a nucleation rate of R~10^{34} s^{-1} m^{-3}. To match this rate, the nucleation free energy barrier should reach the value of $G_0^{th} \sim 23\, k_B T$, which gives the criterion for evaluation of the temperature dependence of the threshold tensile pressure for the onset of cavitation in short pulse laser spallation:

$$P_{th}^2 = a\gamma_{lv}^3(T)/k_B T, \tag{1}$$

where $a = 16\pi/3\ln(R_0/R) \approx 0.7$ is estimated based on the nucleation rates in the photomechanical spallation regime observed in the atomistic simulations. The temperature dependence of surface tension of a liquid-vapor interface can be approximated as $\gamma_{lv}(T) = \gamma_0(1-T/T_c)^{\mu}$, where γ_0 is a material dependent parameter, T_c is the

critical temperature, and μ can be approximated as 1.26 based on the value of surface tension critical exponent obtained using the renormalization group technique (Goldenfeld 1992). The experimental values of the surface tension at the melting point and the corresponding temperature slops are available for a wide range of materials (Egry et al. 2010; Lu and Jiang 2005). In the following analysis, the values of γ_0 and μ are directly calculated in atomistic MD simulations for several interatomic potentials using the test area method (Gloor et al. 2005).

The analytically derived criterion for the onset of cavitation, Eq. 1, has been tested in a series of small-scale atomistic simulations for several interatomic potentials. In particular, Fig. 9d illustrates the dependence of the cavitation threshold on temperature in Ni described by Embedded Atom Method (EAM) potential parametrized by Mishin (2004). The functional dependence given by Eq. (1) is able to describe the simulation results quite well with the proportionality coefficient $a = 0.66$, which is close to the value of 0.7 obtained based on the theoretical consideration and the number of voids generated during spallation in large scale atomistic simulations. Similar computational analysis has been performed for Al, Ag, and Cr, giving a equal to 0.61, 0.85, and 1.00, respectively (Shugaev and Zhigilei 2019). The corresponding minimum free energy barriers for the onset of cavitation are 27.7, 25.5, 19.7, and 16.8 k_BT, for Al, Ni, Ag, and Cr model systems, respectively. These values of the free energy barrier are distributed around the value of 23 k_BT obtained through the order of magnitude estimation discussed above, and the deviation from the estimated value does not exceed 20% for all considered materials.

Figure 9a illustrates the temporal evolution of the cavitation free energy barrier within Ni target irradiated by a 50 fs pulse at a fluence above the threshold for photomechanical spallation. The corresponding temperature and pressure contour plots are shown in Fig. 8. As discussed in section "Generation of Laser-Induced Stresses," the fast laser energy deposition results in the generation of a strong pressure wave propagating from the surface to the bulk of the target, Fig. 8b. When the tensile component of the pressure wave propagates through the molten part of the target, the free energy barrier for cavitation drops down to a minimum value of ~24.8 k_BT (Fig. 9a, c), which is sufficient to induce nucleation of multiple voids in the subsurface region of the target given the threshold for the onset of cavitation in Ni is 25.5 k_BT (see density contour plot in Fig. 9b and an atomic snapshot Fig. 9e). Following the nucleation, the voids grow, coalesce, and eventually percolate leading to the separation/spallation of the top liquid layer from the bulk of the target. It is interesting to note that the depth where the free energy barrier reaches its minimum value, Fig. 9c, and the voids nucleate, Fig. 9b, does not coincide with the depth where the maximum tensile stresses are generated, Figs. 8b and 9c. While the tensile stresses are increasing with depth and reach their maximum value close to the solid-liquid interface, the temperature decreases with the depth and, as a result, the ability of the material to support transient tensile stresses increases. The theoretical equation, Eq. (1), accounts for the interplay of these two factors and predicts the onset of the cavitation at an intermediate depth of ~10–40 nm below the original surface, where the free energy barrier drops below

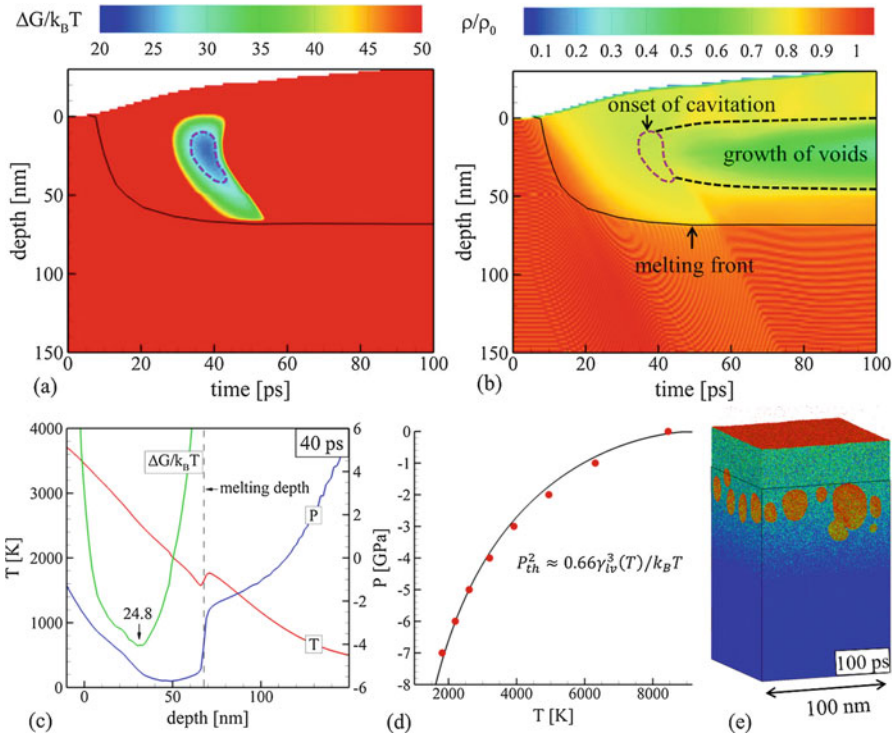

Fig. 9 (**a**, **b**) Contour plots showing spatial and temporal evolution of the free energy barrier for cavitation (**a**) and density (**b**) in a Ni system irradiated by a 50 fs laser pulse at an absorbed laser fluence of 1500 J/m^2, which is above the spallation threshold. Green color in (**b**) indicates the onset of cavitation. (**c**) The spatial profile of lattice temperature (red), pressure (blue), and the free energy barrier (green) at the moment when the barrier reaches its minimum level. The scale of the free energy is from 20 to 50 k_BT. (**d**) The dependence of the cavitation threshold on temperature predicted in MD and fitted to an analytical function provided in the plot. (**e**) An atomic configuration at a time of 100 ps, when the cavitation bubbles are clearly seen. The atoms are colored based on their potential energy, with blue color corresponding to solid, colors between light blue and green depicting liquid, and orange and red colors showing free surfaces. (The figure is adapted and reprinted with permission from Shugaev and Zhigilei (2019))

the threshold value for the rapid onset of the cavitation. This observation is consistent with the results of earlier MD simulations of photomechanical spallation of molecular targets (Zhigilei and Garrison 2000; Leveugle and Zhigilei 2004), Ni (Leveugle et al. 2004; Zhigilei et al. 2009), Cr (Karim et al. 2012; Abou-Saleh et al. 2018), Al (Wu and Zhigilei 2014), and Ag (Wu et al. 2015; Wu and Zhigilei 2016).

The spalled liquid layer leaves behind a rough surface morphology that forms as a result of rapid solidification of transient liquid structures generated as this layer separates from the bulk of the target (Wu and Zhigilei 2016; Abou-Saleh et al. 2018), for example, Fig. 10. The unique nanoscale surface morphology generated by laser

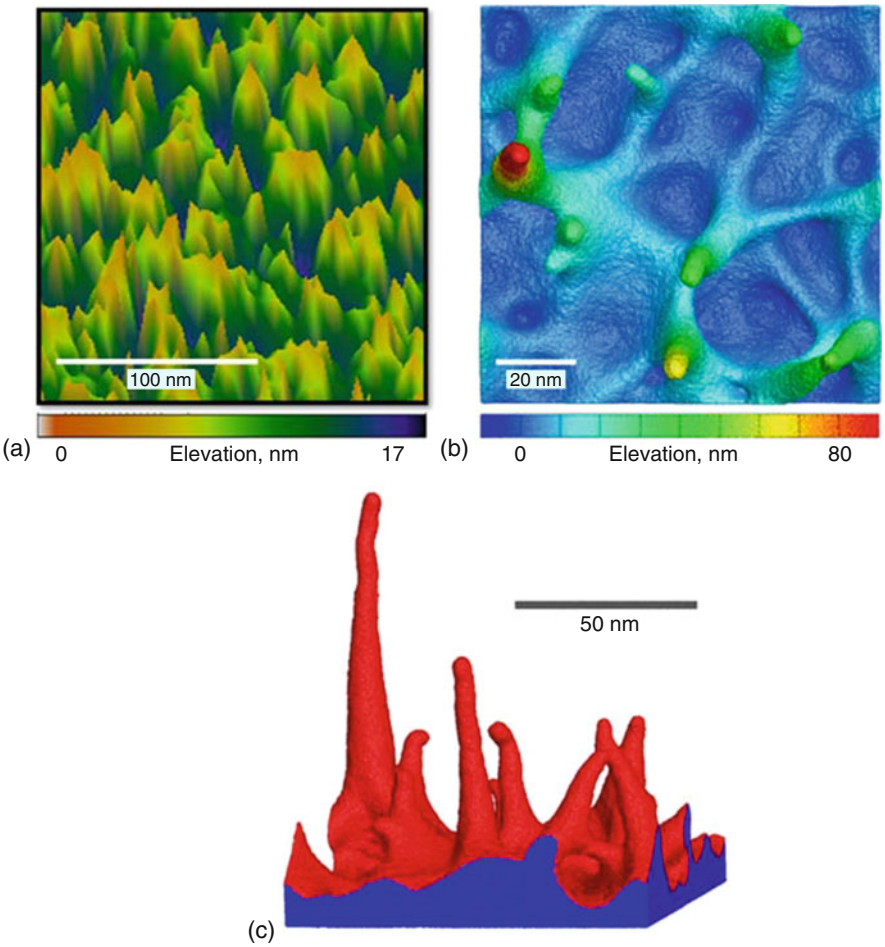

Fig. 10 Surface morphology of a Cr (100) target irradiated by a single 50 fs laser pulse at a laser fluence just above the spallation threshold obtained in experiment (**a**) and in a TTM-MD simulation (**b**, **c**). The atomic force microscope image in (**a**) is shown for the center of the laser-modified region. The top **(b)** and side (**c**) views of the frozen surface morphology are shown for the atomic configuration obtained by the end of the simulation, about 1 ns after the laser pulse. (The figure is adapted and reprinted with permissions from Abou-Saleh et al. (2018))

processing can strongly affect various properties of the surface, including optical absorption (e.g., fabrication of "black" metal surfaces with strongly enhanced broadband absorption (Vorobyev and Guo 2008a) or colored surfaces with wavelength-selective reflection (Vorobyev and Guo 2008b)), hydrophobicity (tuning the surface wetting behavior from superhydrophobic (Papadopoulou et al. 2009) to superhydrophilic (Vorobyev and Guo 2009, 2010)), or enhanced photoelectron and thermal emission (Hwang et al. 2009b).

Stress Induced Generation of Crystal Defects

The spallation or generation of subsurface voids discussed above is not the only way the laser-induced stresses can produce structural modification of an irradiated target. The shear stresses created in the crystalline part of the target by the stress wave passing through the melting front and propagating deeper into the target may be sufficiently strong for generation of dislocations. As an example, the process of gradual accumulation of crystal defects in a polycrystalline Ni target irradiated by 50 fs laser pulses at a fluence close to the melting threshold can be seen in the Electron Backscatter Diffraction (EBSD) maps shown in Fig. 11 (Sedao et al. 2014a). The band slope map in Fig. 11b reflects the degree of lattice distortions and reveals the presence of crystal defects, mainly dislocations. Moreover, the

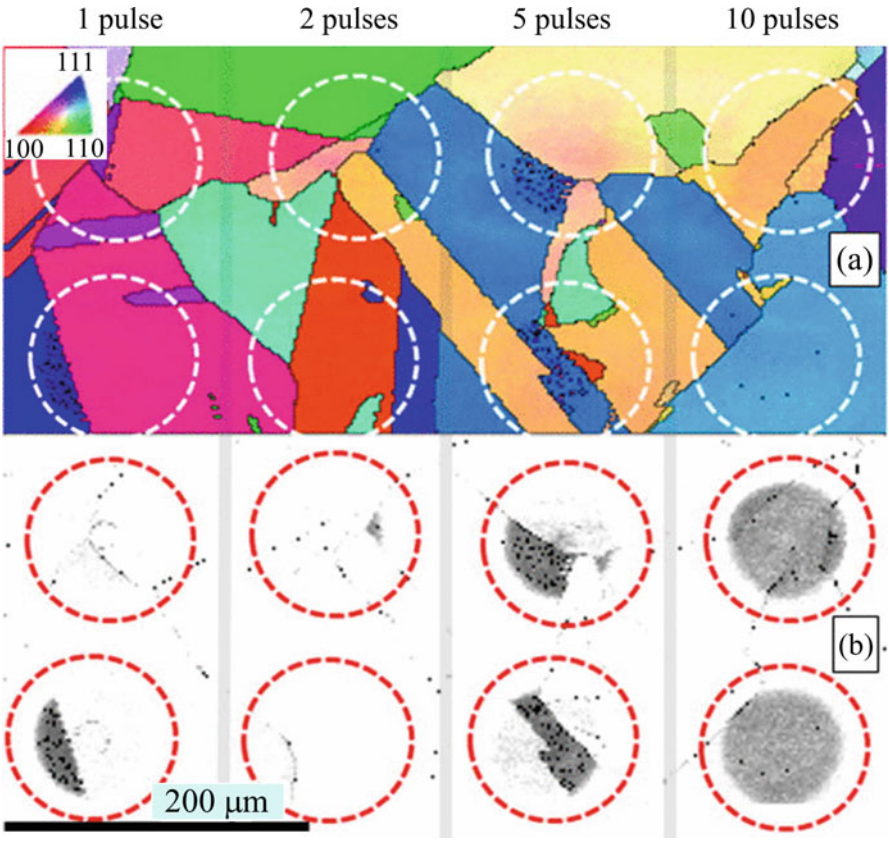

Fig. 11 Electron Backscatter Diffraction (EBSD) orientation map (**a**) and band slope map (**b**) reflecting the presence of defects in a polycrystalline Ni target irradiated by 50 fs laser pulses at incident fluence of 0.3 J/cm^2. The number of pulses applied to spots shown in each row is indicated at the top of the figure. (The figure is adapted and reprinted with permission from Sedao et al. (2014a))

generation of defects shows a clear correlation with crystallographic orientation of grains in the polycrystalline target, as can be seen by comparing the EBSD map shown in Fig. 11a with band slope map shown for the same laser spots in Fig. 11b. One can see, in particular, that the laser-induced lattice distortions are much more pronounced for grains with (111) surface orientation (blue color in Fig. 11a) as compared to the ones with (100) surface orientation (red color in Fig. 11a).

The importance of the grain orientation in the generation of dislocations can be clarified by considering results of TTM-MD simulations of laser irradiation of Ni targets with (111), (011), and (100) surface orientations (Shugaev and Zhigilei in preparation). The simulations were performed in the same irradiation regime that was used in the experiments illustrated in Fig. 11, that is, in the regime of surface melting and resolidification. The snapshots from the simulations taken at a time of 50 ps, shortly after the tensile component of the laser-induced stress wave passed through the melting front, are shown in Fig. 12. The snapshots reveal massive emission of partial dislocations from the melting front in targets with (011) and (111) surface orientations, but not for the target with (100) surface orientation. The Shockley partial dislocations leave behind stacking faults that appear as green planes in Fig. 12. The stacking faults can be erased by trailing partial dislocations that follow the leading dislocation, forming pairs of Shockley partial dislocations connected by stacking faults (correspond to green stripes in Fig. 12).

The results of the simulations can be explained based on analysis of shear stress resolved on slip systems (sets of slip directions and slip planes) that can be activated in the material – the dislocations can be emitted when the resolved shear stress reaches a critical level. Slip in an fcc crystal occurs along close packed planes,

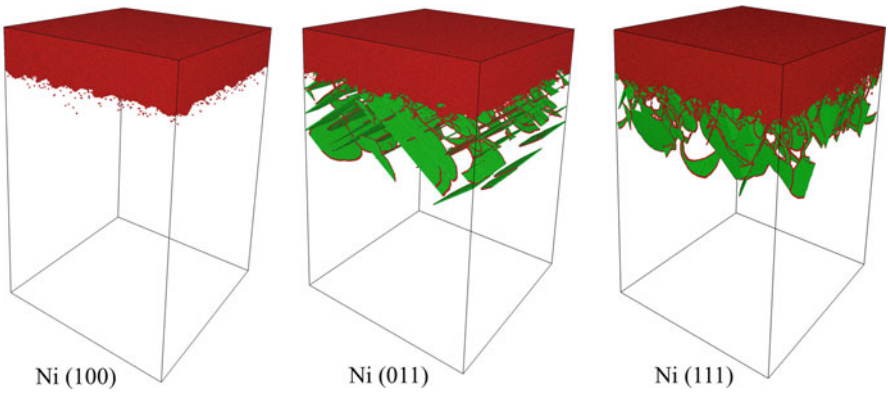

Fig. 12 Snapshots of atomic configurations generated in TTM-MD simulations of Ni (100), Ni (011), and Ni (111) targets irradiated by 50 fs laser pulses at an absorbed laser fluence of 600 J/m^2, just above the melting threshold. The snapshots are taken at 50 ps after the laser pulse. Atoms with face centered cubic (fcc) local structural environment are blanked to expose the defect structures. Green color shows atoms that belong to stacking faults, and red color is used for atoms in the molten parts of the targets and in dislocation cores. Details on the system setup and model parameters are provided in Sedao et al. (2016)

{111}, in ⟨100⟩/2 and ⟨112⟩/6 directions for perfect and Shockley partial dislocations, respectively (Kelly 2000). Each {111} slip plane has three directions for perfect and 3 for Shockley partial dislocations, with the latter having substantially lower barrier for the emission. Theoretical analysis shows that the maximum resolved shear stress in (100) target is almost twice lower than that in the case of (011) and (111) targets if the same strain is applied along z direction. Moreover, the shear stress resolved on the slip systems grows faster in (011) and (111) targets and reaches the maximum values earlier, when the high temperature of the crystalline side of the melting front reduces the critical stress required for the emission of the dislocations. The combined effect of the higher resolved shear stresses and more pronounced thermal softening of the crystal explains the difference in the dislocation activity produced in the three targets by the laser-induced stress wave.

After the initial stage of the dynamic stress relaxation, the level of the resolved shear stress in the surface region of the targets drops down, leading to the retreat of some of the Shockley partial dislocations to the melting front. Other partial and split dislocations react with each other and form a stable network anchored by immobile dislocation segments generated by the reactions among the dislocations propagating on different slip planes. The dislocation network remains in the target after it cools down to the original temperature, producing residual stresses (see section "Generation of Laser-Induced Stresses") and explaining the lattice distortions illustrated in Fig. 11.

Acoustic Activation of Atomic Level Processes

The relaxation of laser-induced stresses on the scale of entire laser spot is accompanied not only by the emission of bulk longitudinal waves discussed in sections "Generation of Laser-Induced Stresses," "Photomechanical Spallation," and "Stress-Induced Generation of Crystal Defects" but also by generation of shear and surface acoustic waves (SAWs). The partitioning of energy between the different components of the acoustic emission, and the corresponding magnitudes of the waves, depends on the system geometry and irradiation conditions (Miller and Pursey 1955). In particular, under favorable conditions, pulse laser irradiation has been shown to be capable of producing quite intense, up to several percent strain, SAWs (Kozhushko et al. 2007). One interesting feature of SAWs is that they can propagate along a thin surface layer of a substrate with little dissipation and, thus, are able to transfer energy far from the laser spot. This characteristic of SAWs has been utilized in many practical applications, including signal processing (Hashimoto 2000), chemical sensing (Buvailo et al. 2011; Schmera and Kish 2003), nondestructive evaluation of mechanical properties (Kozhushko et al. 2007; Lomonosov et al. 2001), and microscale manipulation of fluid flow in microfluidics devices (Jo and Guldiken 2013; Yeo and Friend 2014).

There is also growing experimental evidence of the ability of SAWs to affect surface processes at the atomic/molecular level (Zhigilei and Helvajian 2019). In particular, SAWs and bulk acoustic waves interacting with surfaces have been shown

to be able to substantially enhance the rates and selectivity of heterogeneous catalytic reactions (Inoue et al. 1989; Watanabe et al. 1996; Kelling et al. 1997, 1998; Kelling and King 1998; Saito et al. 2001; Reese et al. 2006; Inoue 2007, 2019; Nishiyama et al. 2000), desorb molecules, atoms, and ions from surfaces (Nishiyama et al. 2000; Denison 1969; Krischer and Lichtman 1973; Golovlev et al. 1997a, b; Lindner and Seydel 1985; Zinovev et al. 2007; Dow et al. 2012; Ma et al. 2019), and facilitate surface diffusion of small atomic clusters (Shugaev et al. 2015; Manzo and Helvajian 2014). Several examples of the acoustic activation of surface processes are illustrated in Figs. 13 and 14a. In particular, a considerable increase in the conductivity of ZnO surface exposed to ethanol is observed when the SAWs are generated, Fig. 13a, suggesting that the surface density of the adsorbed ethanol molecules and the efficiency of the charge transfer to the substrate are enhanced by SAWs (Nishiyama et al. 1999). A gentle desorption of thermally sensitive molecules has been demonstrated in a setup where strong acoustic waves generated by laser irradiation of a rear surface of an Al foil are causing ejection of molecules of interest for mass spectrometry analysis from the top surface (Ehlert et al. 2013), Fig. 13b. A clear evidence of the acoustic activation of surface diffusion is provided in Fig. 14a, where the mean square displacement (MSD) of Au_8 clusters moving on a (111) silicon substrate with and without SAWs is plotted. The SAWs in this experiment (Shugaev et al. 2015) were generated by irradiating the substrate with 6 ns laser pulses at 355 nm wavelength and 100 Hz repetition rate. The motion of individual atomic clusters located at a substantial distance from an elongated laser spot produced with a cylindrical lens

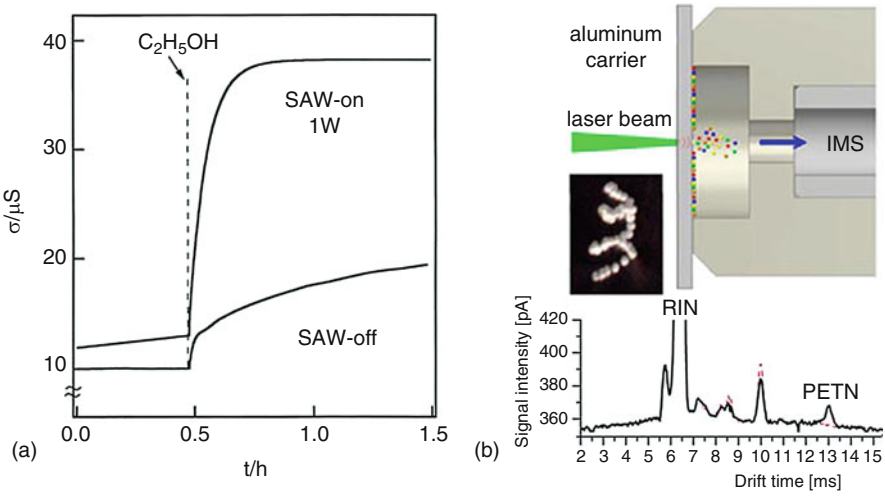

Fig. 13 Experimental evidence of the acoustic activation of surface processes: (**a**) the effect of SAWs on surface conductivity of ZnO due to the ethanol adsorption and (**b**) schematic of a basic setup of laser-induced acoustic desorption mass spectrometry and a mass spectrum of pentaerythritol tetranitrate (PETN) obtained for a small (10 ng) amount of PETN present on the Al foil. (Panels (**a**, **b**) of the figure are adapted and reprinted with permission from Nishiyama et al. (1999) and Ehlert et al. (2013), respectively)

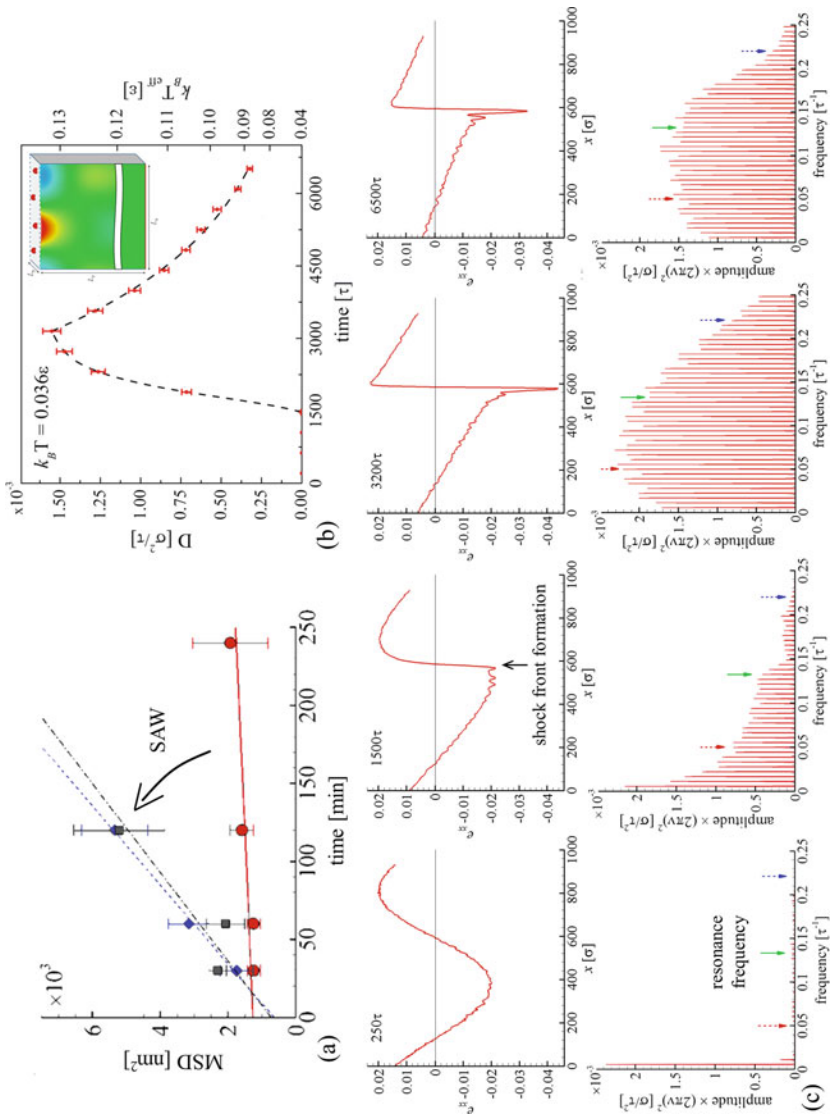

Fig. 14 (continued)

was tracked with fluorescence microscopy. The slope of the MSD versus time dependence is proportional to the surface diffusion coefficient, and the data shown in Fig. 14a demonstrate a 19-fold increase in the cluster mobility in the presence of laser-generated SAWs.

The observations of the acoustic activation of atomic/molecular-level processes are rather unexpected, as there is a large mismatch between the relatively low frequencies of the acoustic waves generated in experiments, typically less than 100 MHz, and the vibrational frequencies characteristic of atoms and molecules on the surface, which are on the order of terahertz. This frequency mismatch calls into question the contribution of the dynamic resonant coupling of the acoustic wave to surface vibrational states (Lindner and Seydel 1985; Golovlev et al. 1997b; Dzegilenko et al. 1996; Almeida and Hood 1992). In a search for alternative explanations, several hypotheses have been suggested. These include the presumed presence of mesoscopic-scale substructures/domains (Kelling et al. 1997; Kelling and King 1998) that can effectively couple to a long-wavelength acoustic excitation, nanoscale stressed surface features that can release the stored strain energy in response to an acoustic activation, thus providing the needed extra energy for the desorption of molecules (Zinovev et al. 2007), or acoustically induced variation of the spatial distribution of adsorbates to affect the surface reaction rates (Reese et al. 2006). Modification of the binding energies and diffusion barriers of adsorbed species induced by the surface strain (Roland and Gilmer 1992; Ratsch et al. 1997; Mavrikakis et al. 1998; Schroeder and Wolf 1997) has also been considered as a mechanism responsible for the acoustic activation of surface processes (Inoue 2007; Wu and Metiu 2000; Wu et al. 2013).

The results of large scale atomistic simulations of surface diffusion of atomic clusters in the presence of nonlinear SAWs reported by Shugaev et al. (2015) have suggested an alternative mechanism of the acoustic activation of surface processes. As shown in Fig. 14b, c, at the initial stage of SAW propagation, when the wave profile is close to a sine function, the diffusion coefficient remains low. Starting from around 1500τ (τ is the Lennard-Jones unit of time, which becomes $\tau \approx 0.366$ ps when the parameters of the model system are mapped to Si (Shugaev et al. 2015)), however, the diffusion coefficient rapidly increases and reaches a maximum value

Fig. 14 (Figure caption is continued on the next page) Acoustic activation of surface diffusion of small atomic clusters (Au_8) by SAWs observed experimentally (**a**) and explained based on the results of a series of large-scale MD simulations (**b**). The explanation of the mechanism of acoustic activation of surface diffusion is based on the formation of a shock front and generation of high frequency harmonics capable of direct energy transfer to the clusters adsorbed on the surface. The plot in (**a**) shows the evolution of mean square displacement (MSD) of individual Au_8 clusters moving on a (111) silicon substrate as a result of thermally activated diffusion (no SAWs, red circles) and SAW-assisted diffusion in regions located 6 mm (blue rhombi) and 12 mm (black squares) from the SAW source. The plot in (**b**) shows the changes of the cluster diffusion coefficient with time of SAW propagation. The insert depicts a schematic representation of the computational system. In (**c**), the temporal evolution of the SAW profile and corresponding harmonics in the wave spectrum predicted in the simulations are shown. Lennard-Jones reduced units are used in (**b**, **c**). (The figure is adapted and reprinted with permission from Shugaev et al. (2015))

that is more than 4500 times higher than the value of thermal diffusion at the temperature of the substrate. This enhancement of surface diffusion corresponds to an equivalent increase of the substrate temperature by a factor of about 3.7. The plots of the wave profiles shown in the upper panels of Fig. 14c demonstrate that the large mobility enhancement coincides with sharpening of the SAW profile and generation of a shock front. The pronounced cusp formed on the compressive side of the wave profile at 3200τ is related to the nonlocal nonlinearity of SAWs (Hamilton et al. 1995; Shugaev et al. 2020), which is an intrinsic feature of SAWs. During the following wave propagation, the wave amplitude and the shock front sharpness are decreasing due to the strong dissipation near the wave front, which also results in an exponential decrease of the cluster mobility. However, despite the substantial attenuation of the wave by the moment of 6500τ, the diffusion coefficient at this time still remains almost 1000 times higher than the one corresponding to thermally activated diffusion.

The physical origin of the acoustic enhancement of surface diffusion can be revealed by considering the evolution of the frequency spectrum that corresponds to the evolving profile of the SAW (lower panels in Fig. 14c). The nonlinear sharpening of the wave front is associated with the generation of high frequency harmonics, which can reach the cluster resonance frequency (green arrows) and lead to an effective dynamic coupling between the SAW and the cluster vibrational modes. The following dissipation of the wave is accompanied by pronounced decrease of the amplitude of high frequency components of the spectrum that coincides with decrease of the cluster mobility. This direct correlation between the evolution of the high frequency components of the wave spectrum and the diffusion enhancement suggests that the latter can be attributed to the dynamic coupling of the high frequency harmonics with the cluster vibrational modes that facilitates an effective transfer of the acoustic energy to the cluster motion.

In order to make a quantitative connection to the experiment discussed above and illustrated by Fig. 14a, the number of wave fronts passing through the diffusion region per unit time (defined by the frequency of the continuous wave generated in the simulations, 15 GHz) should be mapped to the laser repetition rate used in the experiment, 100 Hz. This mapping yields a 22-fold enhancement that is close to the 19-fold diffusion enhancement observed in the experiment (Shugaev et al. 2015). Meanwhile, an extrapolation of the experimentally observed diffusion enhancement to higher repetition rates, which can be readily achieved in experiments, suggests that the SAW-induced athermal increase of the diffusion coefficient by a factor of 10^2–10^3 may be feasible. This estimation suggests that the acoustic activation of surface processes may be sufficiently strong to enable an efficient substitution for thermal activation in applications where heating must be avoided or rapid switching of surface conditions is required.

Laser-Induced Melting and Resolidification

Surface modification by laser irradiation is in the core of many modern processing and fabrication techniques, including laser surface alloying, annealing, hardening, and amorphization, for example (Bäuerle 2000; Molian 1989; Elliott et al. 1972; Lin

et al. 1984; MacDonald et al. 1989; Spaepen and Lin 1984; Lin and Spaepen 1983, 1986; Woychik et al. 1985; Fröhlingsdorf and Stritzker 1986; von Allmen and Blatter 1998; Kaspar and Luft 2001; Biswas and Chattopadhyay 2007; Yang et al. 2007). The improvement of surface properties is achieved by structural and compositional modification of a surface layer through the formation of metastable phases, grain refinement, generation/annealing of crystal defects, redistribution of the alloying elements, and changes in the phase segregation patterns. Most of the methods of laser surface modification involve melting and subsequent resolidification of a surface region. Molten metals have high atomic mobility and usually unlimited solubility, enabling a rapid mixing and homogenization of the alloy. As a result, a range of unusual nonequilibrium surface phases that are not available from pure solid-state reactions can be produced. Similarly, the microstructure (shapes/sizes of grains and arrangement of crystal defects in a crystalline material) of the subsurface region can be drastically altered by laser irradiation, often leading to remarkably fine grain size distribution and high density of crystal defects (Thomas et al. 2009; Shugaev et al. 2017a; Wu et al. 2015; Sedao et al. 2014a, 2016; Ivanov et al. 2010; Vincenc Oboňa et al. 2014). In this section, we provide a brief discussion of the kinetics and mechanisms of ultrashort-laser-induced melting and resolidification, usually occurring under conditions of strong overheating and undercooling, as well as the implications of these processes on surface microstructure modification. In the discussion of melting, we only consider thermal melting occurring after or at the end of electron-phonon equilibration. A more rapid nonthermal melting occurring in covalently bonded materials in direct response to strong electronic excitation on a subpicosecond timescale, for example (Shank et al. 1983; Saeta et al. 1991; Siders et al. 1999; Rousse et al. 2001), are discussed, along with corresponding theoretical interpretations, in (Silvestrelli et al. 1996; Dumitrica et al. 2004; Jeschke et al. 2009; Zier et al. 2015), as well as in another chapter of this handbook (Naghilou et al. 2020).

Mechanisms and Timescales of Melting

Although melting is a common and well-studied phenomenon, the nature of the structural instability of a superheated crystal and the microscopic mechanisms of rapid melting that can be induced by ultrashort pulse laser irradiation are still subjects of active scientific discussions (Wang et al. 1997; Lu and Li 1998; Dash 1999; van der Veen 1999; Chan et al. 2008; Siwick et al. 2003; Oguz Er et al. 2012; Mo et al. 2018). Conventionally, melting starts from heterogeneous nucleation of liquid phase at surfaces and internal crystal defects at temperatures around the equilibrium melting temperature, T_m, and proceeds through the propagation of melting front(s) with minimum superheating above T_m. However, under ultrashort (pico- and femtosecond) pulse laser irradiation, extremely high heating rates of 10^{14} K/s and even higher can be achieved in the targets, suggesting that the contribution of the heterogeneous melting can be kinetically limited (Ivanov and Zhigilei 2007), and a superheating that is sufficiently strong for triggering a rapid

onset of homogeneous nucleation of liquid phase inside the superheated crystal (Cahn 1989, 2001; Rethfeld et al. 2002; Jin et al. 2001; Ivanov and Zhigilei 2003b; Lin and Zhigilei 2006, 2007b) can be achieved. The understanding of the relative contribution of different mechanisms of laser-induced melting requires reliable information on the kinetics of the melting front propagation and homogeneous nucleation of liquid regions under conditions of strong superheating of a solid above T_m.

The application of time-resolved electron and X-ray diffraction (Chan et al. 2008; Siwick et al. 2003; Oguz Er et al. 2012; Mo et al. 2018; Lin and Elsayed-Ali 2002; Williamson et al. 1984), as well optical pump-probe techniques (Chan et al. 2008; Sokolowski-Tinten et al. 1998; Agranat et al. 1999), has provided important information on the kinetics of ultrafast phase transformations with sub-picosecond time resolution. The experimental investigations have revealed that, depending on irradiation conditions and properties of the material, the melting process can take from several picoseconds to nanoseconds for strongly absorbing films or bulk targets irradiated by femtosecond or picosecond laser pulses. In particular, it was reported that the time required to completely melt a 25-nm-thick Al film by picosecond laser irradiation decreases exponentially from 1 ns at $1.4F_{\mathrm{melt}}$ to 20 ps at $2.6F_{\mathrm{melt}}$, where F_{melt} is the laser fluence corresponding to the melting threshold (Williamson et al. 1984). Recent result obtained in ultrafast electron diffraction experiments performed for Au films irradiated by 130 fs laser pulses (Mo et al. 2018) is consistent with these earlier observations. As can be seen from the plot of the melting time measured at different laser energy densities, Fig. 15, it takes more than 1 ns to melt a 35-nm-thick single-crystalline Au film at the threshold energy density for complete melting. The melting time of 800 ps is reported for $1.6F_{\mathrm{melt}}$, and it drops down to 17 ps when the energy density is increased to the maximum value of $5.3F_{\mathrm{melt}}$.

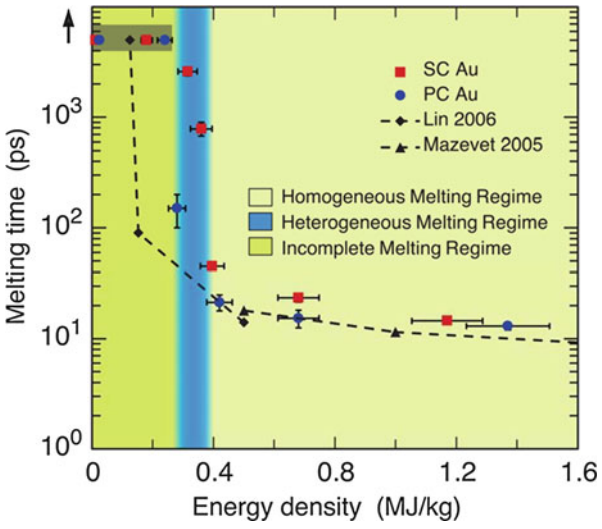

Fig. 15 Energy density dependence of ultrafast laser-induced melting times measured for single-crystalline (SC) and polycrystalline (PC) Au films in ultrafast electron diffraction experiments. The black data points are results from TTM-MD simulations by Lin and Zhigilei (2006) and Mazevet et al. (2005). (This figure is reprinted with permission from Mo et al. (2018))

The melting time on the scale of several hundreds of picoseconds and longer (Mo et al. 2018; Lin and Elsayed-Ali 2002; Williamson et al. 1984; Sokolowski-Tinten et al. 1998) is consistent with the conventional picture of heterogeneous nucleation of liquid phase at the irradiated surface and propagation of the melting front into bulk of the crystal (Spaepen and Turnbull 1979; Jackson and Chalmers 1956; Jackson 2002). The melting time of several picoseconds (Siwick et al. 2003; Oguz Er et al. 2012; Mo et al. 2018; Agranat et al. 1999; Schmidt et al. 2000), however, is too short to be explained by the heterogeneous melting mechanism and implies the contribution of fast homogeneous nucleation and growth of liquid regions in the bulk of the superheated crystal (Chan et al. 2008; Cahn 1989, 2001; Rethfeld et al. 2002; Jin et al. 2001; Ivanov and Zhigilei 2003b; Lin and Zhigilei 2006, 2007b). Therefore, depending on the irradiation conditions, optical and thermal properties of the material, and the time of the electron-phonon equilibration in the system, the dynamics of laser melting is defined by either or both propagation of the melting front from the surface and homogeneous nucleation of the liquid phase in the bulk of the superheated crystal. In order to elucidate the factors that control the relative contribution of different mechanisms of laser-induced melting, below we provide a brief overview of the theoretical descriptions of the heterogeneous and homogeneous melting, followed by a discussion of additional insights provided by atomistic simulations of the melting process.

Heterogeneous Melting

The heterogeneous melting mechanism is generally described as the propagation of melting front from the irradiated surface into bulk of the crystal. Under conditions of slow heating, when the heating time is longer than the time needed for the melting front to pass through the heated region, the melting process starts from surfaces and internal crystal defects under rather minor superheating conditions or even below the equilibrium melting temperature (Dash 1999; van der Veen 1999). The latter effect of surface premelting is observed when the free surface wetted by a thin liquid layer has a lower free energy as compared to the ordered solid surface. The premelting, in particular, makes ice surface slippery and enables skating at temperatures significantly below $T_m = 0$ °C (Rosenberg 2005). After heterogeneous nucleation of the liquid phase, the melting process proceeds by propagation of melting fronts from the surfaces and defect regions, precluding any significant superheating of the remaining crystalline parts of the material and eliminating the possibility for an alternative mode of melting, that is the homogeneous nucleation of liquid in the bulk of a superheated crystal, under conditions of slow heating. In ultrashort pulse laser processing of materials, however, the heating rates can be very high, and the contribution of heterogeneous melting is determined by the distance that the melting front can cover before the temperature in the superheated crystal reaches the threshold for the onset of rapid homogeneous melting (discussed later in this section). The velocity of the melting front propagation, therefore, is a key parameter that plays a decisive role in the underlying physics of melting. Thus, the temperature dependence of the melting front velocity is considered next.

According to the phenomenological transition state theory (Jackson and Chalmers 1956; Jackson 2002), kinetic representation of the steady-state propagation of a crystal-liquid interface during melting/solidification under conditions of overheating/undercooling can be provided based on the difference between the rates of particle transfer from the liquid to the crystal and from the crystal to the liquid, leading to the general equation for the temperature dependence of the velocity of a planar crystal-liquid interface:

$$v(T_i) = v_0(T_i)[1 - \exp(-\Delta G_{sl}(T_i)/k_B T)], \tag{2}$$

where $\Delta G_{sl}(T_i) = G_l(T_i) - G_s(T_i)$ is the difference in the Gibbs free energy between the liquid and solid phases at the interface temperature T_i and $v_0(T_i)$ is the kinetic prefactor that corresponds to the maximum interface velocity. Negative velocity of the interface corresponds to melting, and positive values represent solidification.

Two approaches have been suggested to approximate the temperature dependence of the kinetic prefactor $v_0(T_i)$ based on the microscopic processes responsible for the movement of the interface: diffusion-limited and collision-limited approximations. The first approximation is based on the assumption of significant structural rearrangement during melting or solidification, so that the propagation of the solid-liquid interface is controlled by the diffusivity in the liquid phase with associated Arrhenius temperature dependence:

$$v_0(T_i) = \frac{6aDf_0}{\Lambda^2} \exp(-\Delta S_{sl}/k_B), \tag{3}$$

where $D = D_0 \exp(-Q/k_B T_i)$ is the diffusion coefficient in the liquid, Q is an activation energy associated with atomic diffusion in the liquid, Λ is the average diffusion jump distance, a is the cubic root of the atomic volume (adding an atom to the interface locally shifts it by a distance a), factor $f_0 < 1$ accounts for the fact that some of the atomic rearrangements do not lead to the motion of the interface (Jackson and Chalmers 1956; Jackson 2002), and ΔS_{sl} is the change of entropy upon melting. The analysis based on the diffusion-limited kinetics of the interface, Eqs. (2) and (3), is in a good agreement with experimental results (Stolk et al. 1993) and MD simulations of crystallization in Si (Grabow et al. 1988) and metals (Ashkenazy and Averback 2010).

In another approximation, the kinetics processes at the interface are not thermally activated but are controlled by the frequency of collisions of atoms at the interface. This leads to the collision-limited kinetics of the interface suggested by Turnbull et al. (1962, 1981) and Coriell and Turnbull (1982). In the absence of thermal activation, Turnbull suggested the speed of sound in the liquid to be used as a limiting velocity of the crystal-liquid interface. Early MD simulations of crystallization performed by Broughton et al. (1982) and Burke et al. (1988) with Lennard-Jones interatomic potential supported the collision-limited kinetics of the interface, but suggested that the average thermal velocity of the atoms, $(3k_B T_i/m)^{1/2}$, rather than speed of sound, is more suitable as the kinetic prefactor:

$$v_0(T_i) = \frac{af_0}{\lambda}\sqrt{\frac{3k_BT_i}{m}}\exp\left(-\Delta S_{sl}/k_B\right), \tag{4}$$

where λ is the distance an atom moves to join the crystal and m is atomic mass. The best fit to the results of MD simulations reported in Broughton et al. (1982) gives $\lambda = 0.15\ a$ and $f_0 = 0.27$ (Jackson 2002). The MD simulations of melting and crystallization in metals performed with EAM potential (Jackson 2002; Hoyt and Asta 2002; Sun et al. 2004) predict interface velocities that are in a good quantitative agreement with Eq. (4), although the $\sqrt{T}$ dependence is found to be too weak to describe the temperature dependence of the solidification front velocity under conditions of deep undercooling in Ashkenazy and Averback (2010), where the diffusion-limited approximation is found to be suitable for temperatures above the glass transition temperature.

In the vicinity of T_m, the equation describing the velocity of the solid-liquid interface, Eq. (2), can be approximated by a linear relationship:

$$v(T_i) \approx \mu \cdot (T_m - T_i), \tag{5}$$

where μ is the kinetic coefficient. This approximation provides a description of the kinetics of solid-liquid interface that matches well the results of MD simulations performed at moderate values of superheating/undercooling above/below the equilibrium melting temperature (Jackson 2002; Hoyt and Asta 2002; Sun et al. 2004; Baskes and Stan 2003). Moreover, the linear approximation may be sufficient for the kinetic description of heterogeneous melting at any temperatures, as the maximum superheating before the onset of rapid homogeneous melting is estimated in Luo et al. (2003) to be between 8% and 43% for a broad range of materials heated at an extreme rate of 10^{12} K/s. The maximum velocity of the melting front propagation is further reduced by the local drop of the lattice temperature at the melting front, determined by the kinetic balance between the transfer of thermal energy to the latent heat of melting, the electron heat conduction from the overheated solid to the interface, and the electron-phonon coupling. In particular, TTM-MD simulations accounting for these effects (Ivanov and Zhigilei 2007) predict the maximum velocity of the melting front in Ni to be below 3% of the room temperature speed of sound in the crystal. This maximum velocity is more than an order of magnitude lower than that assumed in early interpretations of pump-probe laser melting experiments (Rousse et al. 2001; Tsao et al. 1986; Ashitkov et al. 2002; Dwyer et al. 2006) and in theoretical investigations (Rethfeld et al. 2002).

Note that for sufficiently long laser pulses, when the rate of thermal energy supply to the liquid-solid interface is slow compared to the interface kinetics, the melting process is *heat flow limited,* and the overheating/undercooling at the interface is often neglected. In this case the velocity of the interface can be described within the framework of the Stefan problem, by a simple energy balance equation at the interface, which, in the absence of convection in the liquid, can be formulated as

$$v\rho_s \Delta H_m = k_s \left.\frac{\partial T}{\partial x}\right|_i - k_l \left.\frac{\partial T}{\partial x}\right|_i, \tag{6}$$

where k_s and k_l are the thermal conductivities in the solid and liquid phases, respectively, ρ_s is the density, and ΔH_m is the latent heat of melting. The temperature at the interface is assumed to be continuous and equal to the melting temperature, $T_i = T_m$. While this model is physically flawed (there should be no motion of the interface if $T_i = T_m$), it has been successfully used in most of the computational studies of materials processing involving melting and resolidification. Indeed, the values of overheating/undercooling are typically very small in most of the conventional methods of heat treatment, and Eq. (6) predicts the velocity of the interface rather accurately. For laser processing with nanosecond and longer laser pulses, in particular, the difference between the melting front propagation predicted by the Stefan model and the kinetic equations has been shown to be relatively small (Černý et al. 1991; Xu et al. 1999; Kapat et al. 1998), and the assumption of the heat flow limited propagation of the interface is reasonable. In laser irradiation by shorter, picosecond or femtosecond laser pulses, however, much faster thermal energy flow to/from the liquid-solid interface can be induced by very steep temperature gradients, creating conditions for significant superheating/undercooling of the interface. The kinetics of melting process in this case is *interface limited,* and the nonequilibrium kinetic description based on Eqs. (2), (3), (4), and (5) is necessary.

Homogeneous Melting

According to MD simulations, the maximum velocity of the melting front propagation in a metal can be as high as several hundreds of m/s (~500 m/s for Ni (Ivanov and Zhigilei 2007)) at the limit of crystal stability for the onset of massive homogeneous melting (see below). Due to the local drop of the lattice temperature at the melting front related to the development of electron-phonon nonequilibrium, however, the actual maximum steady-state melting front propagation velocity is lower, ~100 m/s. Using this value of the melting front propagation velocity and the typical depth of melting induced by an ultrashort laser pulse in a strongly absorbing target of the order of 100 nm, one can estimate that it would take around a nanosecond for the melting front to propagate from the irradiated surface down to the melting depth. This estimation suggests that, for laser pulses with sub-nanosecond pulse duration, the heterogeneous melting process would not be able to keep up with the heating rate. As a result, the material in the surface region of the target can be superheated up to the limit of crystal stability against a rapid onset of melting. Indeed, the results of TTM-MD simulations of ultrashort pulse laser interactions with metal targets reveal that a massive homogeneous nucleation of liquid regions inside the superheated crystal occurs at ~(1.20–1.25) T_m for Au (Ivanov and Zhigilei 2003a; Lin et al. 2010), Ag (Wu et al. 2015), Ni (Ivanov and Zhigilei 2003a, b, 2007; Zhigilei et al. 2009), as well as Ni-Fe and Ni-Cr solid solution alloys (He et al. 2019), resulting in the fast phase transformation in the superheated region within just several

picoseconds. Moreover, the simulations predict that the lattice distortions and stress gradients induced by the fast laser heating can reduce the level of superheating required for the initiation of homogeneous melting down to as low as $1.05T_m$ (Ivanov and Zhigilei 2003b).

Theoretically, the limit of superheating for the onset of rapid homogeneous melting can be estimated based on the classical nucleation theory (Turnbull and Fisher 1949; Rethfeld et al. 2002; Volmer and Weber 1926; Turnbull and Cech 1950). Let us consider the nucleation of small liquid regions in a superheated crystal, followed by their growth and coalescence leading to complete melting of the crystal. The nucleation rate required to completely melt a bulk crystal within a melting time of τ_m can be estimated as $R \approx (2v\tau_m)^{-3}{\tau_m}^{-1}$, where v is the velocity of propagation of crystal-liquid interfaces generated by the nucleation. Assuming that the duration of the rapid homogeneous melting at the limit of superheating is ~10 ps (Ivanov and Zhigilei 2003b; Lin and Zhigilei 2006; Lin et al. 2010) and using a maximum value of v of the order of 500 m/s (Ivanov and Zhigilei 2007), the nucleation rate at the limit of superheating can be estimated to be $\sim 10^{35}$ s^{-1} m^{-3}. Similarly to the discussion of cavitation in section "Photomechanical Spallation," the nucleation rate can be expressed as $R = R_0 \times \exp(-G_0/k_BT)$, where G_0 is the nucleation barrier and R_0 is a prefactor weakly dependent on temperature.

The nucleation barrier can be found by considering the change in the Gibbs free energy upon the formation of a nucleus with a radius r, $\Delta G = \Delta G_{sl}V + \gamma_{sl}A$, where γ_{sl} is the solid-liquid interfacial free energy and ΔG_{sl} is the difference in volumetric free energy between solid and liquid phases, see Fig. 16. Analysis similar to that discussed in section "Photomechanical Spallation" for the onset of the cavitation suggests that ΔG reaches its maximum value (nucleation barrier) of $G_0 = \Delta G(r_c) = 16\pi\gamma_{sl}^3/3\Delta G_{sl}^2$ at a critical radius of $r_c = 2\gamma_{sl}/\Delta G_{sl}$. Neglecting the difference in heat capacities of liquid and solid phases in the vicinity of the melting temperature, we can express the volumetric free energy difference (driving force for the phase transformation) through the enthalpy of melting, ΔH_m, and the level of superheating above the equilibrium melting temperature, $\Delta T = T^* - T_m$, as $\Delta G_{sl} \approx \Delta H_m \Delta T/T_m$.

Taking Au as an example, with $T_m = 1338$ K, $\Delta H_m = 1.2 \times 10^9$ Jm^{-3}, and $\gamma_{sl} = 132 \times 10^{-3}$ Jm^{-2} (Howe 1997), we can calculate the critical nucleation barrier that is consistent with the results of MD simulations, which predict the maximum temperature reached before the onset of rapid homogeneous melting within ~10 ps to be $T^* = 1.25T_m$ for Au (Ivanov and Zhigilei 2003a; Lin and Zhigilei 2006; Lin et al. 2010). At $T^* = 1.25T_m$, the volumetric free energy difference is $\Delta G_{sl} \approx 3 \times 10^8$ Jm^{-3} (Fig. 16b), and the threshold value of the nucleation barrier is ${G_0}^{th} \approx 17.4\ k_BT^*$ (Fig. 16c). To match the nucleation rate at the limit of superheating, estimated above as $R = R_0 \times \exp\left(-G_0^{th}/k_BT^*\right) \approx 10^{35}$ s^{-1} m^{-3}, the pre-factor R_0 should be of the order of $\sim 10^{42}$–10^{43} s^{-1} m^{-3}, which matches well the estimation discussed above, in section "Photomechanical Spallation."

The sharp, threshold-like onset of the homogeneous melting observed in MD simulations (Ivanov and Zhigilei 2003b; Lin and Zhigilei 2006; Lin et al. 2010) is consistent with a very steep temperature dependence of the nucleation rate R on the degree of superheating ΔT, $R \sim \exp\left(-A/(\Delta T)^2\right)$, where A is a parameter weakly, as

compared to $(\Delta T)^2$, dependent on temperature. This sharp dependence of the nucleation rate, illustrated in Fig. 16d, results in a relatively weak sensitivity of the limit of superheating to the exact values of the material parameters and approximations used in the analysis of the nucleation kinetics.

Note that the value of critical radius r_c evaluated for the threshold temperature of T^* is only ~0.9 nm (Fig. 16c), that is, only a few interatomic distances. Taken together with the fact that the distance the melting front can propagate during the melting time of $\tau_m = 10$ ps is less than 5 nm, the physical picture of nucleation and growth of spherical liquid regions, assumed in the analysis outlined above and illustrated in Fig. 16a, is not expected to be valid up to the limit of crystal stability against homogeneous melting. Indeed, the results of MD simulations indicate that the melting at the limit of superheating proceeds through simultaneous formation of a large number of interconnected small liquid regions within entire superheated volume, leading to the collapse of the crystal lattice within several picoseconds (Ivanov and Zhigilei 2003b; Lin and Zhigilei 2006; Lin et al. 2010).

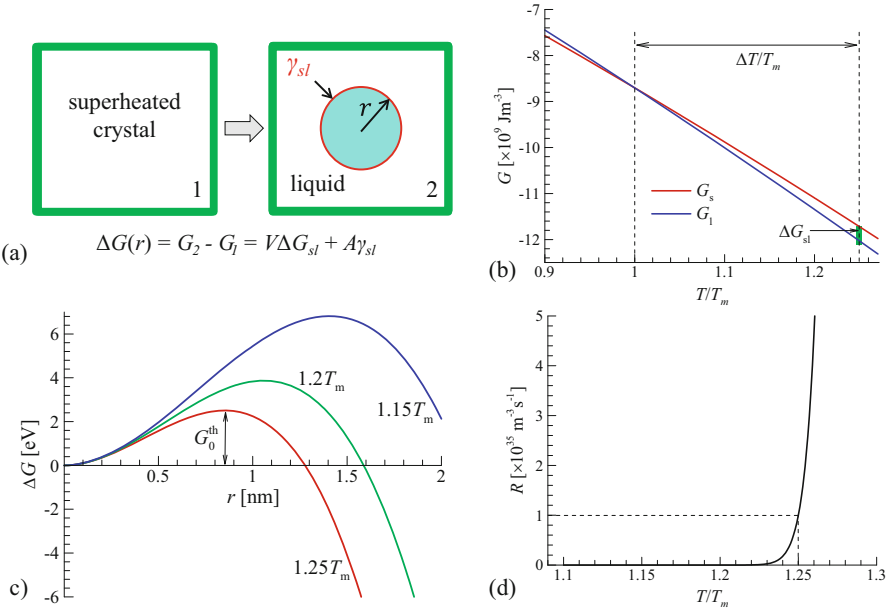

Fig. 16 The application of the classical nucleation theory to analysis of thermodynamic conditions leading to the onset of rapid homogeneous melting: (**a**) Schematic illustrating the free energy change $\Delta G(r)$ due to the appearance of a spherical liquid region of radius r inside a superheated crystal, (**b**) the volumetric free energy change ΔG_{sl} associated with melting at a temperature of $T_m + \Delta T$, (**c**) $\Delta G(r)$ plotted for three different levels of superheating, with the threshold value of the nucleation barrier G_0^{th} marked for $T^* = 1.25T_m$, and (**d**) the temperature dependence of the nucleation rate. All thermodynamic relations are calculated using the experimental thermodynamic properties of Au (Howe 1997; Arblaster 2016)

Homogeneous Versus Heterogeneous Melting

Based on the discussion of the kinetics of heterogeneous and homogeneous melting provided above, we can now perform analysis of the relative contributions of these two mechanisms to laser-induced melting. A schematic map of different mechanisms of melting is provided in Fig. 17a, which is based on the results of MD simulations performed for Ni represented by an EAM potential (Zhigilei et al. 2010). Heterogeneous melting starts from the free surface(s) of the target as soon as the temperature exceeds the equilibrium melting temperature, T_m. The value of T_m changes with pressure according to the Clapeyron equation, and this pressure dependence can be

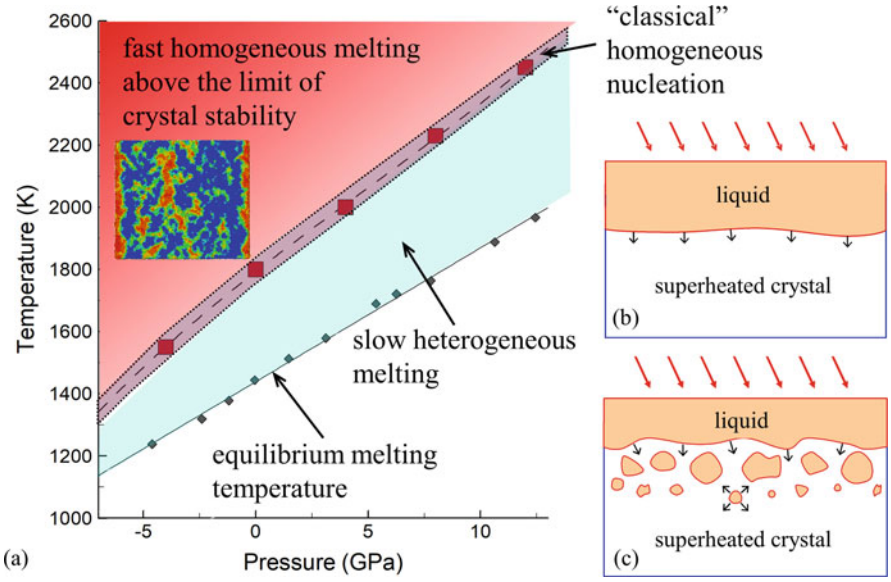

Fig. 17 (**a**) Schematic map of pressure/temperature conditions for equilibrium and nonequilibrium melting predicted in MD simulations of EAM Ni (Zhigilei et al. 2010). Black diamonds, corresponding to the equilibrium melting temperature, are obtained in liquid-crystal coexistence simulations, where the interface does not move under conditions of controlled constant temperature and pressure. Red squares connected by the dashed line correspond to the temperature of the maximum superheating of a crystal as a function of pressure, which is defined as the temperature at which melting starts within tens of picoseconds in a simulation performed for a perfect crystal with 3D periodic boundary conditions and constant hydrostatic pressure. The areas of the pressure-temperature field corresponding to the ultrafast homogeneous melting above the limit of superheating, classical homogeneous melting by nucleation and growth of individual liquid regions, and heterogeneous melting by the melting front propagation from the surface are shown by red, pink-gray, and light blue colors, respectively. The snapshot in the red field is from a TTM-MD simulation of femtosecond laser melting of an Au film (Lin and Zhigilei 2007b). (**b**) Schematic illustration of laser-induced heterogeneous melting process. (**c**) Schematic illustration of laser-induced melting, where homogeneous nucleation of liquid regions ahead of the melting front takes place. The red and black arrows in (**b, c**) indicate the directions of laser irradiation and propagation of liquid-crystal interface, respectively

evaluated in MD simulations of liquid-crystal coexistence. The results of such simulations are shown by small black diamonds connected by the solid line in Fig. 17a. Under conditions that are shown as a blue area above the equilibrium melting line in Fig. 17a, the melting proceeds through the propagation of the melting front into the superheated crystal, as schematically depicted in Fig. 17b. The velocity of the melting front increases with increasing degree of superheating, as described by Eqs. (2), (3), (4), and (5), but is limited by a maximum steady-state velocity of ~100 m/s that can be reached before the onset of homogeneous nucleation of melting regions ahead of the propagating melting front (Ivanov and Zhigilei 2007), Fig. 17c.

For a metal or strongly absorbing semiconductor target irradiated by an ultrashort laser pulse, the depth of a surface region heated during the time of electron-phonon equilibration is on the order of 100 nm. Since the time of the electron-phonon equilibration does not exceed a few tens of picoseconds even for metals with weak electron-phonon coupling, the melting front can only cover a few nanometers during the time of the lattice heating. This suggests that the heterogeneous melting mechanism does not make any substantial contribution to the melting process at laser fluences significantly exceeding the threshold for surface melting. The crystal below the irradiated surface can be readily superheated up to the limit of crystal stability against melting, leading to the rapid homogeneous melting within several picoseconds, as discussed above in section "Homogeneous Melting." Indeed, the limited contribution of heterogeneous melting has been confirmed in TTM-MD simulations of laser interactions with bulk Ni (Zhigilei et al. 2009; Sedao et al. 2016; He et al. 2019), Ag (Wu et al. 2015), and Cr (Karim et al. 2012; Abou-Saleh et al. 2018) targets irradiated by femtosecond and picosecond laser pulses. Comparable contributions of the homogeneous nucleation and growth of liquid regions and heterogeneous propagation of melting fronts from free surfaces have only been observed for Au films (relatively week electron-phonon coupling) irradiated close to the melting threshold (Lin et al. 2010). The results of recent ultrafast electron diffraction experiments probing the melting time for 30-nm-thick Au films (Mo et al. 2018), shown in Fig. 15, confirm that the melting time at the threshold for complete melting can be in the range of hundreds of picoseconds, which provides a sufficient time for the melting fronts to pass through the 30-nm-thick film studied in these experiments.

Note that the sharp (threshold-like) temperature dependence of the nucleation rate in the homogeneous melting, discussed in section "Homogeneous Melting" and illustrated in Fig. 16d, essentially eliminates the possibility for "classical" homogeneous melting occurring through the nucleation and growth of well-defined spherical liquid regions. In MD simulations, such process was only observed for systems with no surfaces or internal defects (modeled using 3D periodic boundary conditions) slowly heated up to the limit of superheating. The corresponding data points are shown in Fig. 17 by red squares connected by dashed line. Under conditions of ultrashort pulse laser irradiation, the thermodynamic trajectory of the rapidly heated material can readily overshoot the narrow region where the classical homogeneous nucleation may occur (narrow pink-gray region in Fig. 17) and enter the red region above the limit of crystal stability, where a catastrophic collapse of the crystal structure occurs in the entire superheated region (see section "Homogeneous Melting").

For the nanosecond and longer laser pulses, the lower heating rates may provide a sufficient time for the melting front to pass through the region of the material heated by the laser pulse without reaching the levels of superheating required for the onset of homogeneous nucleation. The melting process in this case occurs in the blue region of Fig. 17 and can be described by either the kinetic equations, Eqs. (2), (3), (4), and (5), or even by the heat flow limited model given by Eq. (6).

Rapid Solidification and Implications on Surface Microstructure and Morphology

The laser melting of a surface region of the irradiated target is normally followed by cooling due to the heat conduction to the bulk of the target and resolidification. The shallow melt depths, typically produced by ultrashort pulse laser irradiation, and the high thermal conductivity in the case of metals, may lead to very high cooling rates reaching 10^{12} K/s, strong undercooling, and very rapid resolidification. In particular, optical pump-probe measurements performed for a single crystal Zn target irradiated by a 1 ps laser pulse have yielded the time of re-crystallization as short as 100–300 ps (Agranat et al. 1999). Similar solidification time was measured using optical third harmonic generation for Ag films of various thickness deposited on MgO substrate (Chan et al. 2009), as illustrated for an 800-nm-thick film in Fig. 18a. These results are also consistent with earlier observations for metal films and multilayers deposited on a sapphire substrate and irradiated by 20 ps pulse (Chan et al. 2009), Fig. 18b.

The interpretation of the experimental data in terms of the mechanisms and kinetics of the solidification process occurring under conditions of strong undercooling below the equilibrium melting temperature may be assisted by computer simulations. In agreement with experimental observations, the results of atomistic modeling of laser-material interactions predict that complete solidification of metal targets irradiated by femtosecond and picosecond pulses takes, depending on the material and irradiation conditions, from 250 ps to ~3 ns in melting and resolidification regime (Zhigilei et al. 2009; Karim et al. 2012; Sedao et al. 2016; He et al. 2019), and several nanoseconds in the regimes of spallation and phase explosion (Wu et al. 2015; Wu and Zhigilei 2016; Shugaev et al. 2017b; Abou-Saleh et al. 2018). More importantly, the simulations are capable of revealing the connections between the solidification conditions and the microstructure generated in the surface regions of targets undergoing rapid melting and resolidification, as is illustrated by several examples provided below.

While the time-resolved pump-probe experimental studies discussed above are capable of revealing information on the kinetics (characteristic timescales) of solidification, they provide virtually no information on the evolution of the microstructure in the irradiated targets. A rare exception is a study where the time-dependence of the integrated X-ray intensity from a 150-nm-thick Au (111) film excited by a 100 fs laser pulse (see Fig. 18c) was interpreted in terms of the generation of a nanocrystalline "mosaic" structure that "fuses" into the original single crystal within only 100 ps (Chen et al. 2011). A surprisingly short time of the solidification and

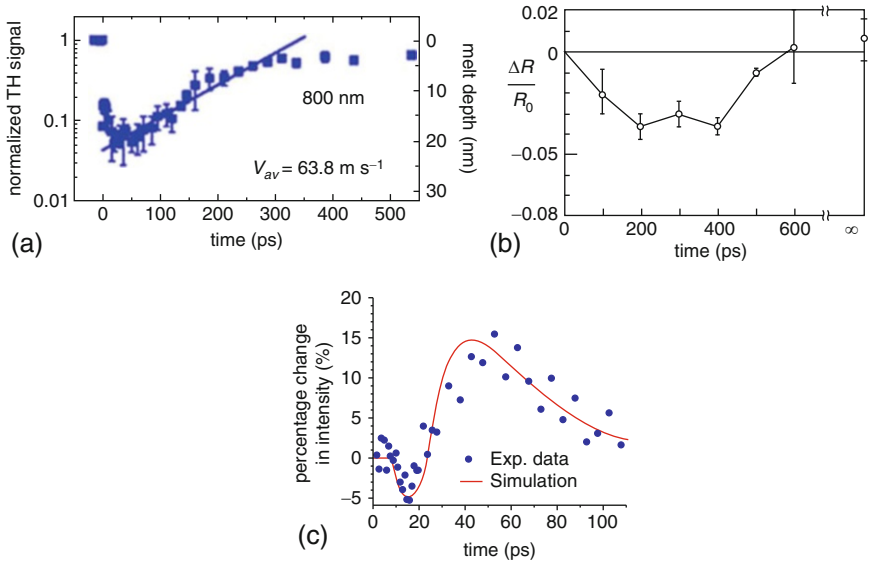

Fig. 18 The results of time-resolved probing of the solidification kinetics: (**a**) The optical third-order harmonic (TH) signal and the corresponding estimated melt depth measured for an 800-nm-thick film deposited on a MgO substrate and irradiated by a 140 fs laser pulse (Chan et al. 2009); (**b**) relative reflectivity change measured for a 20-nm-thick Au film on a sapphire substrate, irradiated by a 20 ps laser pulse (MacDonald et al. 1989); (**c**) time dependence of the integrated X-ray intensity measured for a 150-nm-thick Au (111) film irradiated by a 100 fs laser pulse (Chen et al. 2011). (Adapted and reprinted with permission from Chan et al. (2009) (**a**), MacDonald et al. (1989) (**b**), and Chen et al. (2011) (**c**))

recrystallization calls for additional investigation and, perhaps, revisiting the interpretation of the experimental data.

The *ex situ* characterization of microstructural changes produced by short-pulse laser irradiation has also been challenging due to the confinement of the laser-induced structural modifications within a surface region that can be as shallow as tens to hundreds of nanometers (Sedao et al. 2014a; Chen et al. 2011; Feng et al. 2005; Picard et al. 2004; Margetic et al. 2003; Le Harzic et al. 2002). Nevertheless, the results of EBSD measurements (Sedao et al. 2014a, b; Vincenc Oboňa et al. 2014) have provided important information on the local crystallographic orientation of nanoscale surface features generated by femtosecond laser irradiation of metal targets, for example, Fig. 19a, b. In particular, the local crystal misorientation map generated for a cross-section of a Ni target irradiated by a 50 fs laser pulse (Sedao et al. 2014b), Fig. 19a, reveals the presence of lattice distortions that can be associated with high densities of dislocations generated in the course of surface resolidification. The results of EBSD probing of the frozen spikes generated by irradiation of a Cu surface by a 6.7 ps laser pulse (Vincenc Oboňa et al. 2014), shown in the inset in Fig. 19b, are indicative of a random crystallographic orientation of the heads of the frozen spikes with respect to the underlying grains in the target. These

EBSD results, combined with the observations of contrast changes along the spikes in high-resolution transmission electron microscopy (TEM) images (Vincenc Oboňa et al. 2014), suggest a nanocrystalline structure of the nanospikes and indicate that homogeneous nucleation of new crystallites is likely to be involved in the crystallization process. Such a conjecture is supported by the results of atomistic modeling of laser spallation of Ag targets (Wu and Zhigilei 2016), where the homogeneous nucleation of crystallites in a strongly undercooled liquid bridges generated in the spallation process is observed. As a result, the frozen nanospikes produced in the

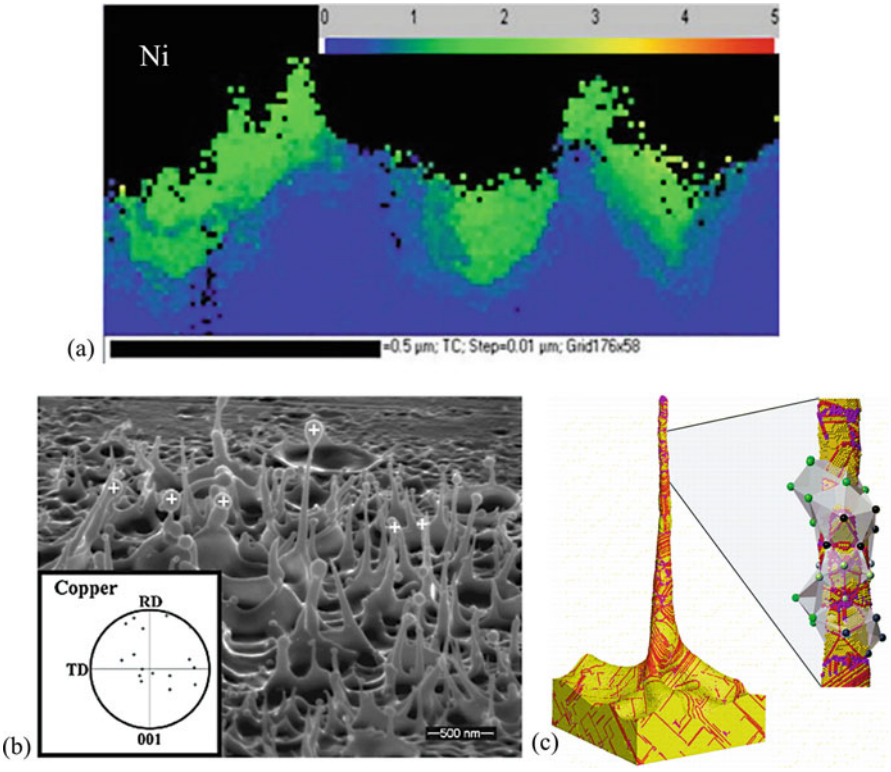

Fig. 19 The results of EBSD measurements (**a**, **b**) and atomistic modeling (**c**) of the microstructure generated by rapid solidification of laser irradiated surface. (**a**) Local crystal misorientation map (units of color scale are degrees) determined by EBSD for a cross-section of Ni target irradiated by a 50 fs laser pulse (Sedao et al. 2014b). (**b**) Scanning electron microscopy (SEM) micrograph and the results of EBSD measurements (pole figure in the inset) suggesting a random orientation of the heads of frozen spikes generated by irradiation of a Cu surface by a 6.7 ps laser pulse (Vincenc Oboňa et al. 2014). (**c**) Frozen nanospike with polyicosahedral structure generated in an atomistic simulation of an Ag target irradiated by a 100 fs laser pulse above the spallation threshold (Wu and Zhigilei 2016). The atoms in (**c**) are colored so that the atoms that belong to regions with fcc structure are yellow, stacking faults and twin boundaries are red, and other defects are purple. (Adapted and reprinted with permission from Sedao et al. (2014b) (**a**), Vincenc Oboňa et al. (2014) (**b**), and Wu and Zhigilei (2016) (**c**))

spallation process are featuring random crystallographic orientation of nanograins as well as unusual structural motifs composed of truncated interpenetrating icosahedra, Fig. 19c.

The kinetics and mechanisms of solidification have major implications on the final microstructure and morphology of laser-processed surfaces. These implications are discussed in details in a chapter of this handbook focused on laser-induced generation of crystal defects and phase transformations (Vilar 2020). Therefore, here we only provide a brief overview of four general types of surface modification directly controlled by the rapid solidification, namely, (1) modification of surface phase composition and homogenization, (2) generation of crystal defects in the course of the solidification, (3) modification of grain size and shape distribution, and (4) formation of complex surface morphology due to the rapid freezing of molten structures produced by laser-induced melt splashing and flow.

An important implication of the high cooling rates realized in laser processing is the ability to prevent phase separation in the course of the rapid solidification, leading to the formation of metastable amorphous or solid solution phases. In particular, metallic glass formation for systems not previously considered being glass formers has been achieved by ns- and ps-pulse laser quenching, for example (Lin et al. 1984; MacDonald et al. 1989; Spaepen and Lin 1984; Lin and Spaepen 1983, 1986; Woychik et al. 1985; Fröhlingsdorf and Stritzker 1986; von Allmen and Blatter 1998). Although the cooling rates in short and ultrashort pulse laser quenching exceed the ones realized in conventional techniques of metal glass production (such as the melt spinning or splat-cooling) by five or more orders of magnitude, it is not the only factor that determines the outcome of the competition between crystallization and glass formation. The shallow depth of the melted layer makes the effects of the crystalline substrate and free surface on the solidification process non-negligible even at the highest cooling rates, whereas the short time of solidification introduces constraints on the number of crystal phases that can compete with the glass formation. In particular, compounds that require nucleation and growth of structurally complex ordered phases are excluded from the competition due to the insufficient time for atomic rearrangement, and only disordered solid solutions can be formed. A new definition of the glass forming ability that would take into account not only the thermodynamic and kinetic factors, but also the specifics of the laser quenching method, is needed.

Surface amorphization by laser processing has been demonstrated to significantly improve the surface corrosion resistance by eliminating surface defects and secondary phases often responsible for the initiation of pitting corrosion (Hashimoto and Masumoto 1983). An example of the generation of a metastable corrosion-resistant amorphous surface layer on a bulk crystalline Al-Co-Ce alloy processed by nanosecond laser pulses (Hoekstra et al. 2005) is provided in Fig. 20. Note that the laser-induced surface amorphization is not a necessary condition for improving the corrosion resistance of the metallic alloys. The formation of homogeneous crystalline supersaturated solid solution phases and elimination of intermetallic particles can also result in significant improvement of the corrosion resistance, as have been demonstrated for Mg alloys processed by nanosecond lasers (Melia et al. 2016, 2017).

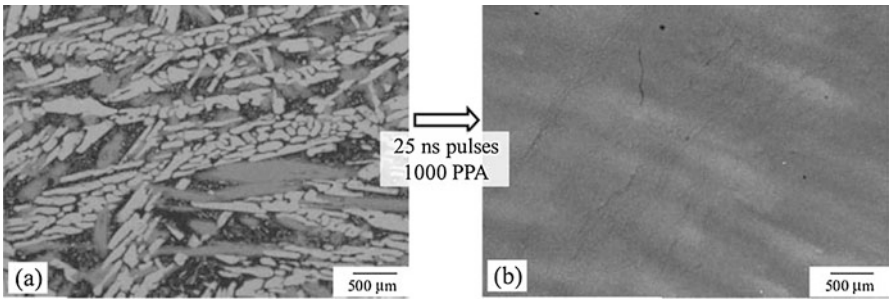

Fig. 20 Backscattered electron images of $Al_{84}Co_{7.5}Ce_{8.5}$ samples before (**a**) and after (**b**) irradiation by 25 ns laser pulses at a fluence of 0.75 J/cm^2 and 1000 pulse per area (PPA). The polycrystalline surface region is turned into homogeneous layer with amorphous structure and enhanced corrosion resistance. (Adapted and reprinted with permission from Hoekstra et al. (2005))

In addition to chemical homogenization and generation of metastable phases, rapid solidification proceeding under conditions of deep undercooling of the molten material can produce a high concentration of crystal defects in the resolidified part of the target. For example, the presence of nanoscale twinned domain has been observed in a subsurface region of a polycrystalline Cu target irradiated by a single picosecond laser pulse in the regime of surface melting and resolidification (Vincenc Oboňa et al. 2014), Fig. 21a. The high density of twin boundaries has also been observed in single crystal Ni targets with (111) surface orientation (Sedao et al. 2016), Fig. 21b. The atomistic- and continuum-level simulations performed for experimental irradiation conditions reproduce the generation of twinned domains, Fig. 21c, and establish the conditions leading to the formation of growth twin boundaries in the course of the rapid melting and epitaxial regrowth of the surface regions of the irradiated targets. In particular, the simulations supported by theoretical analysis of the mechanisms of {111} solid-liquid interface propagation predict the onset of the growth twinning at a well-defined threshold level of undercooling and establish the connection between the degree of undercooling and the density of twins generated at the rapidly advancing solidification front (Sedao et al. 2016).

The atomistic simulations also predict generation of a strong vacancy supersaturation in a region subjected to laser melting and resolidification (Wu et al. 2014; Karim et al. 2014; Lin et al. 2008b; He et al. 2019). The vacancies are generated as "errors" during the process of building the crystal structure at the solid-liquid interface, while the rapid propagation of the solidification front leaves insufficient time for atomic rearrangements at the front needed to correct these "errors." As a result, very high vacancy concentrations, substantially above the equilibrium values at the melting temperature, can be generated, as illustrated for a $Fe_{50}Ni_{50}$ solid solution system in Fig. 22. As one can see from a snapshot of atomic configuration shown in Fig. 22a and the spatial distribution of vacancies shown in Fig. 22b, the transient melting followed by the rapid solidification creates a vacancy concentration (ratio of the number of vacancies to the number of lattice sites) as

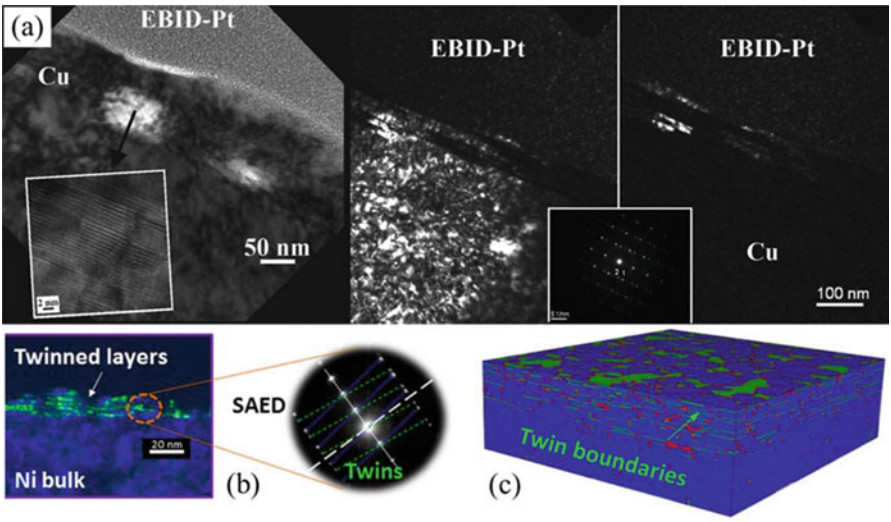

Fig. 21 Experimental observation (**a**, **b**) and computational prediction (**c**) of the generation of twinned domains in the surface regions of a Cu target irradiated by a 6.7 ps laser pulse (Vincenc Oboňa et al. 2014) (**a**) and a Ni target irradiated by 50 fs laser pulses (Sedao et al. 2016) (**b**, **c**) in the regime of melting and resolidification. In (**a**), the high-magnification TEM image of the highlighted location shows the details of the material twinning, while the dark field TEM images to the right reveal the presence of subsurface twins. In (**b**), two superimposed TEM images highlighting the epilayers (blue) and twinned domains (green) in the laser-processed surface region of a Ni (111) target, and the results of the selected-area electron diffraction (SAED) analysis confirming the presence of twinned domains are shown. In the simulated system shown in (**c**), the coherent and incoherent twin boundaries generated within the top 30 nm region of the irradiated target are shown as green atomic layers and red regions within the blue fcc crystal, respectively. (Adopted and reprinted with permission from Vincenc Oboňa et al. (2014) (**a**) and Sedao et al. (2016) (**b**, **c**))

high as ~2×10^{-4}, which exceeds the equilibrium concentration at the melting temperature. Interestingly, the analysis of the first atomic shell surrounding the vacancy site reveals the preference for vacancy sites to be surrounded by Fe atoms (even though the addition of Fe decreases the total vacancy concentration as compared to pure Ni by almost a factor of 5). This can be seen in Fig. 22c, where the distribution of the number of Ni atoms surrounding vacancies is shown. The pronounced shift of the distribution towards lower number of Ni atoms, as compared to the random distribution of the two components, reflects this preference. This observation is the simplest example of the ability of crystal defects to create atomic-scale chemical heterogeneities and to affect local thermodynamic stability of alloys, which may have important practical implications. Moreover, the high vacancy supersaturation in the subsurface regions of laser-processed targets may foster atomic diffusion and play an important role in redistribution of impurities or mixing/alloying in multicomponent systems.

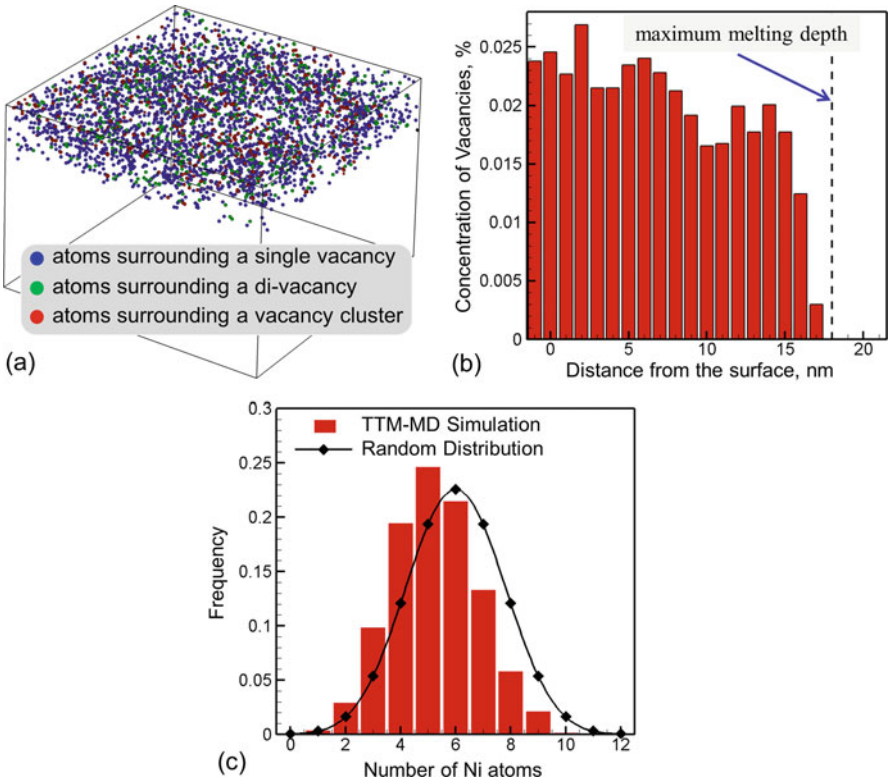

Fig. 22 Results of a TTM-MD simulation of a $Fe_{50}Ni_{50}$ target irradiated by a 100 fs laser pulse at an absorbed fluence of 400 J/m^2, in the regime of melting and resolidification. The atomic configuration (**a**), spatial distribution (**b**), and local environment (**c**) of vacancies generated in a surface region of the irradiated target are shown. The atoms with local surrounding that correspond to fcc lattice are blanked in (**a**) to expose the crystal defects. The dashed line in (**b**) marks the maximum melting depth reached after the laser irradiation. (Adapted and reprinted with permission from He et al. (2019))

Modification of sizes and shapes of crystal grains and different phases in multiphase systems is another important consequence of laser processing involving melting and resolidification. In material processing with long laser pulses or continuous wave irradiation, the solidification microstructure is determined by the combination of heterogeneous nucleation and growth processes, which in turn are controlled by the temperature evolution in the molten pool and composition of the material. In particular, the levels of undercooling required for the onset of heterogeneous nucleation are defined by the presence of thermally stable nucleation sites, while the growth morphologies (e.g., columnar vs. equiaxed) are sensitive to the local temperature, heat flow conditions, and composition at the solidification front. *Ex situ* analysis of the laser-treated surface layer can provide information on the

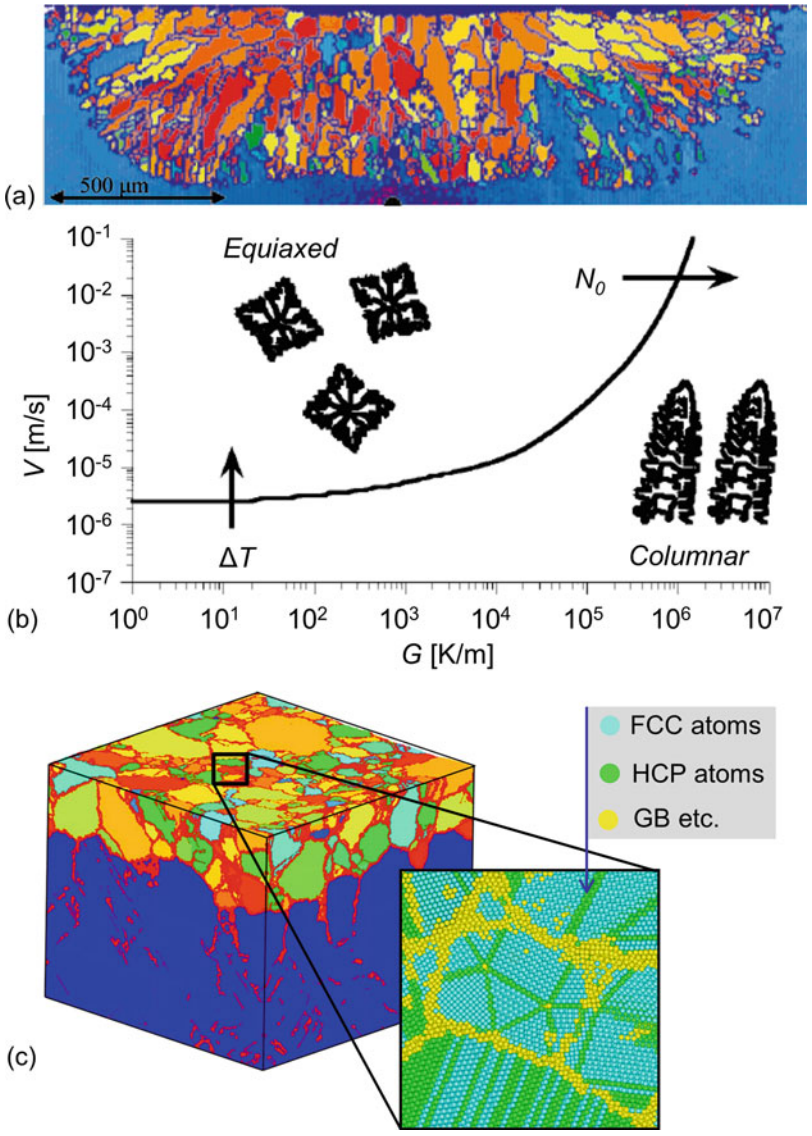

Fig. 23 Micro (**a**, **b**) and nano (**c**) scale grain morphology generated by laser processing. In (**a**) an EBSD map of a cross-section of a continuous laser trace produced in a Ni-base superalloy target is shown. The microstructure in (**a**) is generated under irradiation conditions that lead to equiaxed dendritic growth, as predicted by the Solidification Microstructure Processing Map (**b**) showing the domains of columnar and equiaxed solidification in the space of solidification front velocity, V, and temperature gradient at the crystal-melt interface, G. In (**c**), a nanocrystalline structure of a thin surface region of a Ag target irradiated by a 100 fs laser pulse below the spallation threshold and an enlarged view of the atomic structure of one of the grains are shown. The grains are colored according to their crystallographic orientation, and the atoms in the atomic view of the structure are colored so that the single and double green layers on a light blue background correspond to twin

microstructure and phases generated in the course of rapid solidification, for example, Fig. 23a, which, in turn, may be related to the kinetics and mechanisms of the partitioning of the alloy components at the liquid-crystal interfaces, solidification front velocity, as well as nucleation and growth of new phases. For long laser pulses or continuous laser treatment, the laser-affected zones are large (on the order of mm) and microstructures can be easily studied by optical or transmission electron microscopy. Indeed, a detailed and systematic analysis of sections of the laser traces has been performed and resulted in Solidification Microstructure Processing Maps developed for a number of binary and ternary systems (Kurz 2001; Gill and Kurz 1995; Gäumann et al. 1997; Pan et al. 1997, 1998; Hunziker and Kurz 1997). These maps can take form of diagrams depicting crystal growth modes, phases and microstructures generated at different growth rates, temperature gradients, and/or alloy composition, for example, Fig. 23b.

In the case of ultrashort pulse laser irradiation, the surface layer subjected to laser melting and resolidification can be as small as tens of nanometers, for example, (Sedao et al. 2016; Cangueiro et al. 2016), making experimental characterization of laser-induced microstructural changes challenging. Large-scale atomistic modeling (Shugaev et al. 2017a; Wu et al. 2015), however, predicts that the steep temperature gradients generated by the ultrashort laser pulse irradiation may create conditions for reaching the levels of deep undercooling in the transiently melted surface region of the target sufficient for the onset of massive homogeneous nucleation of new crystallites. As a result, a thin nanocrystalline surface region can be produced (Wu et al. 2015), as illustrated in Fig. 23c. Moreover, the surface nanocrystallization can be facilitated by performing laser processing under conditions of spatial confinement by solid or liquid overlayer, as has been demonstrated in MD simulations (Shugaev et al. 2017a). The nanocrystalline layers generated by rapid nucleation and growth under conditions of deep undercooling are characterized by a random crystallographic orientation of nanograins, as well as a high density of stacking faults, twin boundaries, point defects, and nanoscale twinned structural elements with fivefold symmetry, as can be seen on the enlarged view of atomic structure in Fig. 23c. The possibility of the generation of thin nanocrystalline layers with high density of twins is highly attractive, as such layers can exhibit an unusual combination of high strength and ductility (Valiev et al. 2002; Meyers et al. 2006; Fang et al. 2011), as well as enhanced catalytic activity (Trudeau and Ying 1996; Nørskov et al. 2008) and tunable surface reflectance spectra (Lu et al. 2005).

Finally, one more implication of the rapid solidification that stems from the localized nature of the laser energy deposition is the freezing of the transient liquid structures generated due to the dynamic relaxation of laser-induced stresses in laser spallation (see section "Photomechanical Spallation") and an explosive release of

Fig. 23 (continued) boundaries and stacking faults in the fcc structure, while the atoms at the grain boundaries are colored yellow. (Panels (**a**, **b**) are reprinted with permission from Kurz (2001), and panel (**c**) is adopted and reprinted with permission from Wu et al. (2015))

vapor in the explosive boiling (see section "Phase Explosion or Explosive Boiling"). The solidification of the surface layer proceeding simultaneously with active motion and redistribution of molten material can produce complex surfaces morphology that has a profound effect on optical, mechanical, chemical, and other properties of the laser-processed surfaces (Vorobyev and Guo 2008a, b, 2009, 2010; Papadopoulou et al. 2009; Hwang et al. 2009b). While the final surface morphologies of solidified surfaces, such as the ones shown in Fig. 10a for Cr, Fig. 19b for Cu, and Fig. 24 for Au, W, and Pt, are determined by a combination of the irradiation conditions and properties of the target material (surface tension, viscosity, thermal conductivity, among others), the kinetics of the solidification process itself plays an important role as well. For example, the dependence of the surface roughness generated on single-crystal Cr targets by femtosecond laser irradiation in the spallation regime on the crystallographic orientation of the irradiated surface has been attributed by Abou-Saleh et al. (2018) to the dependence of the velocity of the solidification front propagation on the crystallographic orientation of the crystal-liquid interface. The velocity of crystallization front propagation is faster for (100) crystal-liquid interface as compared to more densely packed (111) or (110) interfaces, leaving less time for the surface tension to smooth out the molten surface features generated in the spallation process and producing higher and more refined nanoscale surface roughness on the (100) surface.

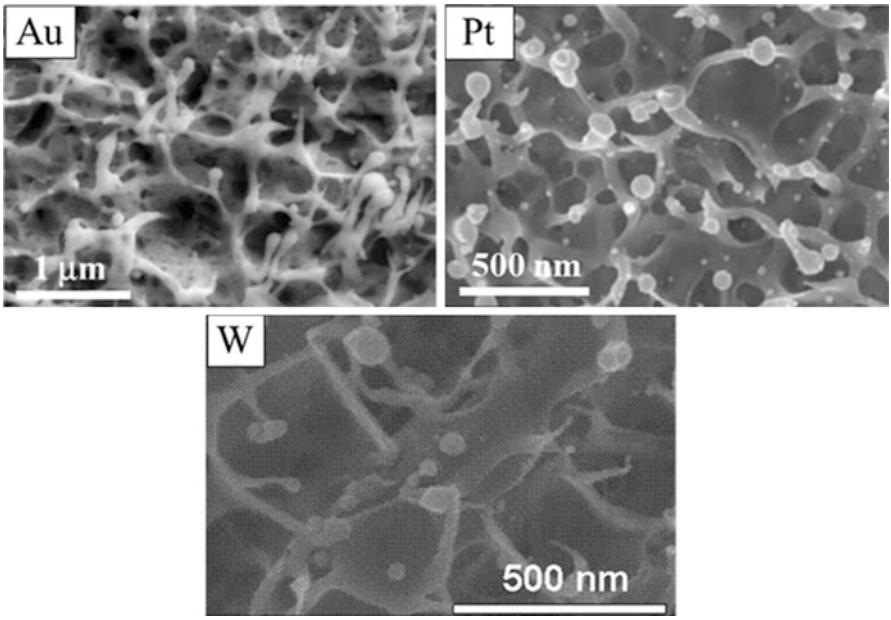

Fig. 24 Nanoscale surface morphology generated in femtosecond laser ablation of metals: two-shot irradiation of Au (Vorobyev and Guo 2005) and Pt (Vorobyev and Guo 2007) and 100-shot irradiation of W (Zhao et al. 2007). (Adopted and reprinted with permission from Vorobyev and Guo (2005, 2007), and Zhao et al. (2007))

Liquid-Vapor Transformations

Laser-induced removal of a material from an irradiated target, called laser ablation, can proceed via different thermal mechanisms, such as normal vaporization (or evaporation), spallation, explosive boiling (usually called phase explosion), and normal boiling. Laser ablation is a common phenomenon in laser micro-/nano-engineering and often is a requirement of a technological process, scientific experiment, or laser-assisted medical treatment.

With an exception of spallation, which is considered in section "Photomechanical Spallation" and represents ejection of a layer of molten and sometimes solid material from the irradiated samples driven by the relaxation of photomechanical stresses, the other thermal mechanisms of laser ablation involve material transformation into a gaseous phase or a mixture of gas, atomic/molecular clusters, and liquid particles (droplets). As the ablation plume expands and cools down, the clusters and droplets can grow and solidify, while new clusters may nucleate and grow into nanoparticles through condensation from the vapor phase. We note that the boundaries between the terms "clusters," "nanoparticles," and "droplets" are fuzzy. Commonly, clusters are assumed to consist of a small number of atoms, usually up to tens, while nanoparticles refer to particulates with diameters ranging from one nanometer to a micrometer. Liquid nanoparticles are often referred to as nanodroplets.

The specific mechanisms of laser ablation strongly depend on irradiation conditions, mostly on the pulse duration and laser fluence, as outlined in Fig. 1. With relatively long laser pulses and under CW irradiation, normal vaporization and normal boiling can be activated, while at short laser pulses, nano- and microsecond ones, vaporization can give turn to phase explosion with increasing laser energy density. For ultrashort (femto- and picosecond) laser pulses, phase explosion is the dominant ablation mechanism, while normal vaporization and normal boiling become practically irrelevant due to the short timescales of material heating and cooling, as discussed below, in sections "Normal Vaporization," and "Normal Boiling."

The ablation mechanism has direct implications for the composition of the ablation plume and the dynamics of the plume expansion in the ambient atmosphere, which can strongly affect technological processes in applications. Ultrashort laser pulses can cause massive material ejection from the target on subnanosecond timescale, and the initial expansion of laser ablation plume is directional along the normal to the target (Fig. 25a; Zeng et al. 2005). Additionally, because of a high intensity of the ablating laser beam, air breakdown occurs along the beam path toward the target that facilitates ablation product expansion in the forward direction, as clearly seen from the figure. This feature is usually absent in the nanosecond irradiation regime, which yields a semispherical plume expansion (Fig. 25b; Zeng et al. 2005). For long laser pulses, the ablation plume resembles a quasistationary jet (Fig. 25c; Kasuya et al. 2001) whose typical structure is shown in Fig. 25d (Bulgakov and Bulgakova 1998). Such regime of vaporization is characteristic of surface processing with laser pulse durations of hundreds of microseconds and longer, when stationary stage of the surface recession can take hold during the laser pulse.

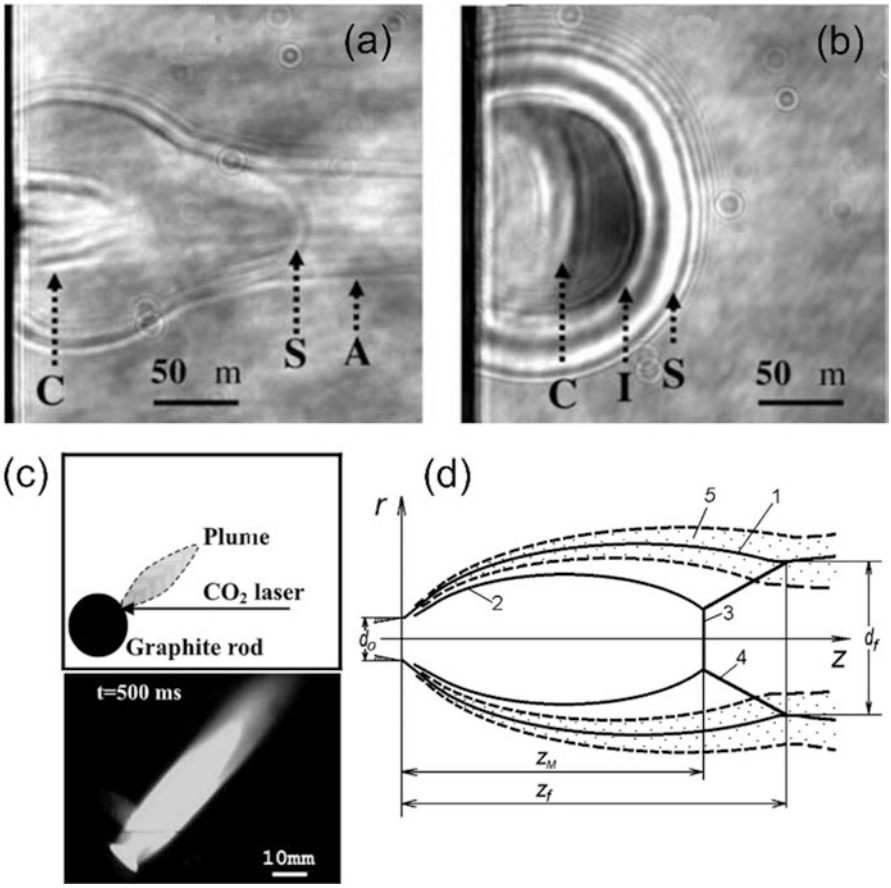

Fig. 25 (**a**, **b**) Plume images obtained by laser shadowgraphy for (**a**) femtosecond (100 fs, 800 nm wavelength) and (**b**) nanosecond (3 ns, 266 nm) laser ablation of Si at 10 ns after laser shot (Zeng et al. 2005). The shock front (S), ionization front (I), contact front between the ablation products and air (C) and air breakdown plasma (A) are labeled in the figures. Ablation was performed at 1 atm air. (**c**) Configuration of a graphite rod, CO_2 laser beam (wavelength of 10.6 μm), and laser plume in experiments (top) and the image of emission of laser-vaporized carbon species produced at 150 Torr in Ar gas at room temperature upon laser irradiation at power density of ~20 kW/cm^2 and pulse duration of 500 ms (bottom) (Kasuya et al. 2001). (**d**) Typical structure of an underexpanded jet emitted from a sonic or supersonic nozzle (Bulgakov and Bulgakova 1998), where z is the jet axis; d_0 is the diameter of the nozzle exit; (1) is the conventional boundary of the jet; (2) is the internal shock wave (barrel shock); (3) is the Mach disc; (4) is the reflected shock wave; (5) is the mixing layer; z_M is the distance between the nozzle exit and the Mach disc; z_f is the distance between the nozzle exit and the narrowest section of the jet beyond the Mach disc (the intersection point of the reflected shock wave and the jet boundary); d_f is the diameter of this section. In the images (**a**–**c**), the laser beam is directed from the right side. (The images are adapted and reprinted with permission from Zeng et al. (2005) (**a**, **b**), Kasuya et al. (2001) (**c**), and Bulgakov and Bulgakova (1998) (**d**))

Below we consider in detail the three types of vaporization from the molten state of a material: vaporization from the surface, which we also call normal vaporization, vaporization in the bulk of the melt with formation of vapor bubbles, and their diffusion to the surface, which we call normal boiling, and phase explosion (explosive boiling), which manifests itself in an explosive/rapid material decomposition into vapor, atomic clusters, and droplets. The conditions at which each type of vaporization becomes dominant are analyzed.

Normal Vaporization

We start from the normal vaporization mechanism, which is the dominant mechanism of material removal (ablation) for laser pulses of moderate intensities and durations from nanoseconds and longer (Fig. 1). Normal vaporization is a process of thermally activated particle emission from the outer surface of a target. The velocities of atoms or molecules constituting a molten surface region of the target obey the Maxwell-Boltzmann distribution. During laser pulse exposure, the temperature of the surface increases, the distribution shifts towards higher velocities/energies. An increasing fraction of the particles in a high-energy tail of the distribution acquires a sufficient energy to overcome the potential barrier defined by their interaction with the surrounding particles, making it possible for them to eject from the surface. Normal vaporization has no temperature threshold (Kelly and Miotello 1996; Fucke and Seydel 1980) and occurs transiently for any kind of laser-molten solids at any laser fluence and pulse length. However, to have a substantial particle emission, it is necessary to bring the surface to a sufficiently high temperature and to maintain it for a sufficiently long time, as detailed in the analysis provided below.

On an atomistic/molecular level, the processes of evaporation and condensation involve individual atoms or molecules (referred below as particles) escaping from a surface and reattaching to it. Under equilibrium conditions, the number of particles evaporating from the molten surface is equal to that of particles condensed from the vapor phase. Under nonequilibrium conditions inherent for laser-induced vaporization into vacuum or low-pressure ambient gas, a net mass flow across the liquid-vapor interface is developed. To calculate the flux of vaporized particles from an irradiated surface, J, the Hertz-Knudsen equation is usually used (Bäuerle 2000; Kelly and Miotello 1996; Fucke and Seydel 1980):

$$J = \alpha(P_v - P_a)(2\pi m k_B T_s)^{-1/2}. \tag{7}$$

Here, the flux is measured in particles per unit area per unit time, α is the condensation coefficient, which accounts for the fraction (between 0 and 1) of particles condensing to the surface when colliding with it; P_v is the saturated vapor pressure corresponding to the surface temperature T_s, P_a is the partial pressure of gas permanently present in the ambient atmosphere; m is the particle mass.

The velocity of the liquid-vapor interface (recession of the surface due to evaporation of the material) can be obtained from Eq. (7) by multiplying the flux by m/ρ (equivalent to λ^3, with ρ being the material mass density and λ being the interatomic spacing in the material), which yields the following expression for a one-dimensional case:

$$v_{lv} = \alpha P_v (2\pi m k_B T_s)^{-1/2} \lambda^3. \tag{8}$$

Note that, when deriving Eq. (8), it is assumed that $P_a = 0$ for vacuum and $P_a << P_v$ for an ambient gas that is typical for intense laser-vaporization conditions. Using the Clausius-Clapeyron equation for P_v, Eq. (8) can be rewritten as

$$v_{lv} = \alpha P_b \exp\left(\left\{\frac{\Delta H_v}{k_B}\left(\frac{1}{T_b} - \frac{1}{T_s}\right)\right\}\right)(2\pi m k_B T_s)^{-1/2} \lambda^3, \tag{9}$$

where ΔH_v is the latent heat of vaporization and T_b is the boiling temperature under the reference pressure P_b. The parameters P_b and T_b are usually taken for normal atmospheric conditions. They serve only as normalizing values and do not imply the boiling vaporization mechanism. Equation (8) can also be expressed in units of *monolayers per second,* which enables a transparent intuitive evaluation of the efficiency of vaporization at a given temperature T_s (Kelly and Miotello 1996):

$$v_{lv}^{\text{mono}} = \alpha P_v^{\text{atm}} \left(\frac{1000}{T_s} \times \frac{100}{M}\right)^{1/2} 5.28 \times 10^7, \tag{10}$$

where P_v^{atm} is equal to P_v expressed in atmospheres. Table 1 reports the data on the number of atomic layers vaporized within time intervals of 1 and 100 ns for several metals at two temperatures, below and above the boiling temperature at normal pressure P_b, evaluated using Eq. (10). It should be noted that, under real laser irradiation conditions, the surface temperature is dynamically changing and can transiently achieve levels that are substantially higher than those used in the calculations reported in Table 1 (Bulgakova and Bulgakov 2001; Bulgakova et al. 2004), yielding an efficient surface recession through normal vaporization before the material experiences overheating toward a deep metastable state required for the transition to the phase explosion regime.

It is worth mentioning that, upon laser irradiation even at low to moderate intensities, the vaporization behavior is not as ideal as presented above. This is due to the fact that other processes and peculiarities can influence on surface recession, such as:

(i) Absorption of laser energy by the material evaporated during laser action, thus affecting the energy deposition on the material surface and, hence, the evaporated particles flux
(ii) Spatial inhomogeneity of irradiation/absorption (spatial variation of laser intensity within the laser spot, surface roughness) and the development of the Knudsen layer
(iii) Development of a back flux of particles recondensing on the liquid surface, especially after the formation of the Knudsen layer

Table 1 Atom layers (λ) removed by normal vaporization at temperatures below and above T_b for various substances listed in order of increasing melting temperature T_m (Kelly and Miotello 1999). Unless otherwise indicated, the information is given for metal (l) → metal (g) transition, where l refers to liquid and g refers to gas. The evaluations were made with Eq. (10), where the data on the vapor pressures P_v^{atm} were taken from Hultgren et al. (1973), Knacke et al. (1991), Chase et al. (1985), Barin and Platzki (1995). The table reprinted with permission from (Kelly and Miotello 1999)

Substance	T (K)	Atom layers in 1 ns	Atom layers in 100 ns	T_b (K)	T_s (K)	Atom layers in 1 ns	Atom layers in 100 ns
Na	1000	0.020	2.0	1156	1500	0.78	78
Bi[a]	1000	0.000	0.000	1837	2000	0.058	5.80
Sb[b]	1000	0.000	0.002	1860	2000	0.047	4.7
Ag	2000	0.002	0.24	2435	3000	0.31	30.5
U	4000	0.005	0.48	4404	5000	0.069	6.9
Nb	4500	0.003	0.27	5017	5500	0.069	6.9
Mo	4000	0.001	0.092	4912	5000	0.028	2.8
W	5000	0.000	0.041	5828	6000	0.010	1.04

[a]The sum of two processes, involving Bi(g) and Bi_2(g), was considered
[b]The sum of three processes, involving Sb(g), Sb_2(g), and Sb_4(g) was considered

These three facets of the normal vaporization phenomenon are briefly discussed below.

Laser Interaction with the Laser Ablation Plume

The interaction of the laser pulse with the ablation plume can be significant when the laser pulse duration is of the order of dozens of picoseconds or longer, so that the laser-irradiated material starts to expand already during the laser action (Wu and Zhigilei 2014; Semerok and Dutouquet 2004). As shown in Bulgakova and Bulgakov (2001), Schmidt et al. (1998), and Bulgakov and Bulgakova (1999) for nanosecond laser pulses, substantial shielding of laser light by laser-produced plasma is developed. This effect leads to a saturation of the ablation efficiency (Bulgakova and Bulgakov 2001; Bulgakova et al. 2004) and, under certain conditions, can create a positive feedback to ablation via hot plasma formation, which radiates in UV spectral range, thus supplying more energy to the target than provided by intrinsic absorptivity of the target material (Bulgakova et al. 2011). However, in these cases, it is also important to consider the possible increase in pressure (its role in vaporization is seen in Eq. (7)) exerted by the plasma on the surface of the material.

Knudsen Layer

The evaporation of the liquid surface is releasing atoms/molecules into the half space above it, at random angles with respect to the direction normal to the surface, and with the velocities distributed according to a *half*-Maxwellian velocity distribution at the temperature of the surface T_s

$$f_s = n_s\left(\frac{m}{2\pi k_B T_s}\right)\exp\left(-\frac{m}{2k_B T_s}\left(v_x^2+v_y^2+v_z^2\right)\right), v_x \geq 0. \quad (11)$$

Here n_s denotes the equilibrium number density of vaporized particles at T_s. If the flux of evaporated particles is sufficiently dense, the collisions among the particles result in evolution of the velocity distribution into a full Maxwell-Boltzmann distribution within a few mean free paths at a distance L from the surface,

$$f_L = n_L\left(\frac{m}{2\pi k_B T_L}\right)\exp\left(-\frac{m}{2k_B T_L}\left(v_x-u_L\right)^2+v_y^2+v_z^2\right), \quad (12)$$

where the index L refers to the flow parameters at this distance and u_L is the center-of-mass velocity of the particle flow directed off the surface. The region adjacent to the surface, where this transformation of the velocity distribution occurs, is called the Knudsen layer (KL) (Kelly and Dreyfus 1988; Sibold and Urbassek 1993). In the course of the transformation of the velocity distribution from a half-Maxwellian to full-Maxwellian form, the values n_L and T_L experience strong change, often described as a jump of the flow parameters across this layer (Knight 1979), which is important for an adequate gasdynamic simulation of the laser ablation plume expansion (Gusarov and Smurov 2005).

Back Flux to the Laser Vaporizing Surface

The coefficient α in Eqs. (7), (8), (9), and (10) accounts for the fact that, due to the collisions in the vapor phase, a fraction of vaporized atoms/molecules is scattered back to the vaporizing surface, and their recondensation takes place even if the evaporation proceeds in vacuum. An approximate solution of a gaskinetic problem for laser ablation of a metal gives the fraction of recondensing atoms (back flux) of ~18% for the case of absence of a noticeable absorption of laser light by the metal vapor (Anisimov 1968). This yields $\alpha = 0.82$ that is widely used in modeling of laser ablation of different materials. More exact solutions can be achieved by using the direct simulation Monte-Carlo (DSMC) method (Sibold and Urbassek 1993; Morozov 2004, 2006). Figure 26 presents the DSMC results on the back flux dynamics for different vaporization fluxes (different surface temperatures) from a graphite surface. By the end of vaporization, the back flux is saturated at approximately 16.3% for the cases of strong ablation, when hundreds of monolayers are vaporized. The results were obtained for atomic vaporization. For molecules or small clusters emitted from the surface, back flux can increase due to energy supply to the expanding vapor from the internal degrees of freedom of vapor particles (Morozov 2006). However, by the end of the laser pulse (active vaporization), the back flux is still within 20% (Morozov 2006), thus supporting the assumptions made in Anisimov (1968). Note that, after the initial quasi-1D expansion, the plume expansion becomes substantially three-dimensional and, for this stage, the back flux cannot be predicted within a 1D approach, such as the one used to obtain Fig. 26. Due to the transition to 3D expansion, the back flux is expected to saturate at a level only slightly exceeding that achieved within the 1D expansion stage.

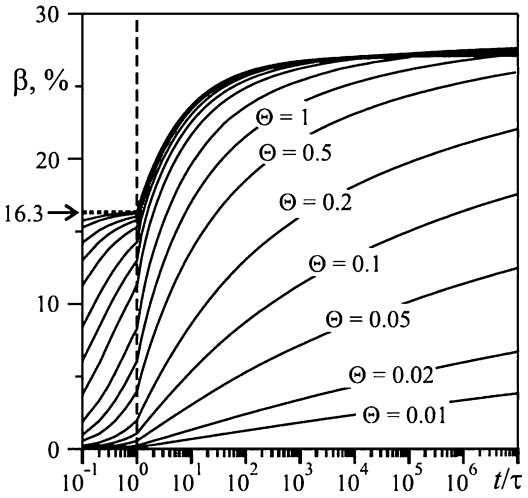

Fig. 26 Results of direct Monte Carlo simulations showing temporal evolution of the back flux β for various values of the number of evaporated monolayers Θ = 0.01, 0.02, 0.05, 0.1, 0.2, 0.5, 1, 2, 5, 10, 20, 50, 100, 200, 500, 1000 (Morozov 2004). Results were obtained for the one-dimensional case of graphite vaporization at a constant rate during a time interval τ, after which the vaporization was stopped. Surface temperature was set to ensure vaporization of corresponding number of monolayers. (Reprinted with permission from Morozov (2004))

Normal Boiling

Normal boiling involves *heterogeneous* nucleation of the vapor phase in liquid. Heterogeneous nucleation is a process where vapor bubbles nucleate at imperfections present on interfaces of the liquid phase with other phases, for example, on scratches, cavities, pits on adjacent solid surfaces. In the case of laser ablation, vapor bubble formation can also be triggered inside a molten material by a variety of disturbances such as dissolved gas or solid impurities. Hence, bubbles can form both at the walls of a solid container (made of a material with higher melting temperature) and in the bulk of the liquid. Upon laser energy deposition, liquid becomes superheated with respect to the pressure-dependent boiling temperature, creating conditions for active formation of vapor bubbles and their growth. Once formed, the bubbles tend to diffuse and can, given enough time of continued maintenance of the state of superheating, $T > T_b$, escape through the outer surface of the liquid. Taken together, all these processes, that is, heterogeneous nucleation of vapor bubbles, their growth and diffusion through liquid volume, and finally their release into surrounding ambient atmosphere, represent the normal boiling phenomenon.

Upon short and ultrashort laser pulse exposure of solid materials, the liquid phase exists for a limited time, from laser-induced melting to solidification. The latter occurs shortly after the laser pulse (at hundreds of nanoseconds or shorter), being determined by material cooling via heat diffusion from the laser-affected zone. For the normal boiling to occur, vapor bubbles need enough time to be released from the

medium where they are generated. This can occur either by their growth until their boundaries touch the interface with an ambient gas or by their diffusion to the interface. Migration of bubbles inside the liquid volume can be governed by gravity and temperature gradients (due to variation of surface tension and viscosity of liquid across the bubble location). In such convective processes, bubble migration velocity depends on temperature, temperature gradient, bubble diameter, as well as the temperature dependence of the parameters of the melt (Narasaki 1983) and is usually below or substantially below 1 m/s. Hence, bubble convection can manifest itself only at microsecond and longer laser pulse durations or CW laser operation. At shorter laser pulses, this process can be neglected (see Fig. 1), as solidification happens faster than bubbles can migrate toward the laser-molten surface. There are some other processes that can contribute to the bubble migration, which are related to atomic diffusion on the bubble surface and through its volume, as well as to vaporization and condensation inside the bubble (Kelly and Miotello 1999). However, it was established (Kelly and Miotello 1999) that these bubble migration mechanisms cannot be efficient at nanosecond timescales, supporting the conclusion that the normal boiling is only relevant for relatively long laser pulses (Fig. 1). For nanosecond and shorter laser pulses, the kinetic limitations on the bubble growth and diffusion eliminate any possibility of normal boiling occurring during the short time the liquid exists in the superheated state, thus making the phase explosion discussed below the dominant thermal mechanism of laser ablation.

Phase Explosion or Explosive Boiling

Under conditions when the normal boiling is kinetically limited (see section "Normal Boiling"), the molten material can be heated far beyond its boiling point (*i.e.*, it becomes superheated into a metastable thermodynamic state). In the volume of strongly superheated liquid, homogeneous nucleation occurs at a high rate, leading to a rapid phase transition to a vapor phase, which resembles explosion and is called *explosive boiling* in thermodynamics. This process has long been known for various kinds of liquids, including molten metals (Skripov et al. 1974). Explosive boiling, traditionally called *phase explosion* in the field of laser-matter interaction (Kelly and Miotello 1996; Bulgakova and Bulgakov 2001; Miotello and Kelly 1995, 1999) and metallic wire explosion (Martynyuk 1974, 1977, 1983), can be achieved in different ways: when liquid is suddenly heated to a high temperature (e.g., by laser heating or by propagation of a shock wave) or when the liquid experiences sudden decompression (e.g., liquid ejected into vacuum). These possible scenarios are schematically shown in the *p-T* phase diagram in Fig. 27.

The principles of *phase explosion* in metals upon discharging a capacitor into a wire were developed in the works by Martynyuk (1974, 1977, 1983). It is known that homogeneous nucleation in liquid metals is not obtained even at large levels of superheating (Skripov et al. 1974). As a result, the metals can be heated very close to the thermodynamic critical temperature (up to $\geq 0.9\ T_c$), where the thermodynamic properties of liquid/melt start to behave anomalously with strongly fluctuating

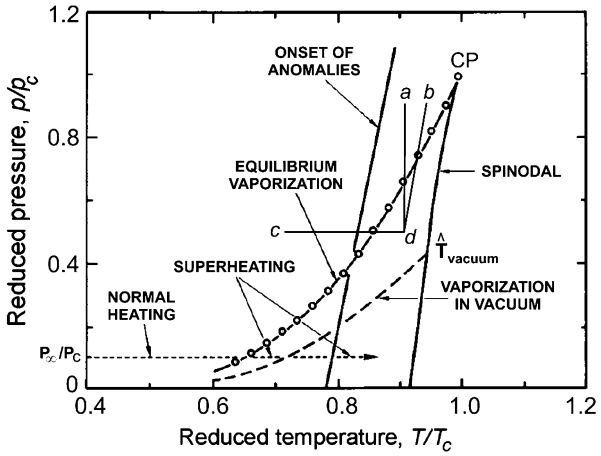

Fig. 27 Pressure-temperature phase diagram of a metal (Cs). CP is the critical point. The region between the spinodal and the line of equilibrium vaporization corresponds to the metastable states of matter. Lines *ad*, *bd*, and *cd* illustrate the different ways to get into a metastable state *d*: *ad* corresponds to isothermal pressure reduction and the line *cd* shows isobaric heating. Due to the low compressibility of the liquid, the line of adiabatic expansion *bd* is close to *ad* (the effect of adiabatic cooling is small). The curve marked "onset of anomalies" indicates an *approximate* temperature at which a number of properties of a melt start to behave anomalously. The rate of homogeneous nucleation of the vapor phase in a superheated molten metal is increasing dramatically at $T/T_c \geq 0.9$, leading to the onset of the phase explosion. (Adapted and reprinted with permission from Miotello and Kelly (1999))

parameters, especially the density which gives rise to homogeneous nucleation of vapor bubbles (Fig. 27).

In thermodynamic treatment, the nucleation of spherical vapor bubbles in a labile equilibrium with the metastable liquid depends on several parameters related to both liquid and vapor phase. In particular, the change in the Gibbs free energy due to the nucleation of a bubble with radius r can be expressed as follows:

$$\Delta G(r) = 4\pi r^2 \gamma_{lv} - (P_v - P_l)\frac{4}{3}\pi r^3 + (\mu_v - \mu_l)\frac{P_v}{k_B T}\cdot\frac{4}{3}\pi r^3. \qquad (13)$$

Here, γ_{lv} is the surface tension of the growing bubble, while $(P_v - P_l)$ and $(\mu_v - \mu_l)$ are the differences in pressure and chemical potential between the vapor and liquid phases, respectively. All quantities are clearly pertinent to the local temperature. The first term in Eq. (13) describes the energy required to form the liquid-vapor interface, the second represents the work necessary to overcome the pressure forces, and the third gives the chemical potential driving force for the bubble formation. For small r, the surface term prevails leading to a positive ΔG, thus avoiding bubble formation. Only for sufficiently large r, ΔG can be negative. The maximum of the function $\Delta G(r)$ defines the critical radius r_c that, under condition of mechanical and thermodynamic equilibrium, has the same expression as that reported in section "Photomechanical Spallation" for photomechanical spallation.

The nucleation rate for the near-critical vapor nuclei per unit volume is given by the expression reported by Skripov et al. (1974):

$$R = \frac{\rho_l}{m}\sqrt{\frac{6\gamma_{lv}}{(3-d)\pi m}}e^{-\Delta H_v/k_BT}e^{-\Delta G(r_c)/k_BT}, \tag{14}$$

where $d = 1 - P_l/P_v$ and ρ_l is the density of the liquid phase. Under extreme thermodynamic conditions, when temperature T approaches T_c, the enthalpy of vaporization ΔH_v, appearing in Eq. (14), may be evaluated by the empirical relation proposed by Watson in 1943 (Watson 1943), which can be applied in a broad temperature range, from the melting temperature T_m to T_c:

$$\Delta H_v = \Delta H_{v0}(\Delta T/\Delta T_0)^{0.38}. \tag{15}$$

Here $\Delta T = T_c - T$, and the values ΔT_0 and ΔH_{v0} are generally associated with the normal boiling point, so that $\Delta T_0 = T_c - T_b$ and $\Delta H_{v0} = \Delta H_v(T_b)$. Equation (15) was proved to provide a reliable estimation for many organic and inorganic pure substances (Skripov et al. 1974) as well as transition metals (Viswanath and Kuloor 1966). The temperature dependence of surface tension in Eq. (13) can be approximated by the empirical formula proposed in 1945 by Guggenheim (1945):

$$\gamma_{lv} = \gamma_{lv0}(1 - T/T_c)^{11/9}. \tag{16}$$

The parameter γ_{lv0} can be estimated from the condition that the expression $\gamma_{lv0}V_c^{2/3}/T_c$ (V_c is the volume of one mole of the liquid phase at the critical point) is a universal value and lies in the range of (4–4.5) erg/(K·mol$^{2/3}$) (Guggenheim 1945), while the liquid and vapor densities at the phase coexistence regions can be modeled as two power series, with the universal exponents and material-dependent coefficients, as fully described in Mazzi et al. (2015).

Regarding the nucleation rate R given by Eq. (14), Martynyuk (1977, 1983) underlines that it becomes significant (i.e., $R \gg 1$ cm^{-3} s^{-1}) only near T_c and gives as an example the values for Cs: $R = 1$ cm^{-3} s^{-1} at $T = 0.874T_c$ and $R = 10^{26}$ cm^{-3} s^{-1} at $T = 0.905T_c$. Such strong temperature dependence of the nucleation rate makes phase explosion to resemble a threshold-like process.

In response to the rapid nucleation of vapor bubbles, a strongly superheated region near the surface swiftly breaks into vapor and liquid droplets (Bulgakova and Bulgakov 2001; Miotello and Kelly 1995, 1999). Experimentally, the transition from normal vaporization to phase explosion is usually identified from a sudden increase of the ablation volume per laser pulse with increasing laser fluence (Fig. 28) (Bulgakova and Bulgakov 2001; Yoo et al. 2000) or from the onset of droplet ejection (Fig. 29) (Porneala and Willis 2009). In particular, the presence of nanodroplets in the ablation plume is clearly seen in Fig. 29, which shows the result of time-resolved imaging of the phase explosion of an aluminum target exposed to irradiation by a Nd:YAG laser at a pulse duration of 5 ns (Porneala and Willis 2009).

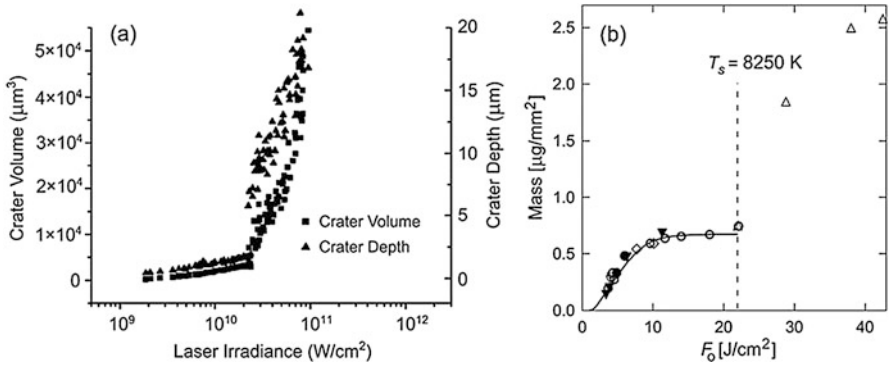

Fig. 28 Illustrations of the transition from normal vaporization to phase explosion. (**a**) Crater volume and depth on silicon surface as a function of laser irradiance, showing an abrupt increase at laser intensity of 2.23×10^{10} W/cm^2 (3 ns pulse duration, wavelength of 266 nm) (Yoo et al. 2000). (**b**) Mass removal per pulse as a function of laser fluence for graphite irradiated by a Nd:YAG laser (13 ns pulse duration, wavelength of 1064 nm). Experimental points have been obtained with different spot diameters: Δ – 0.2 mm, ▲ – 0.3 mm, ○ – 0.4 mm, – 0.5 mm, – 0.6 mm, ▼ – 0.7 mm, ∇ – 0.8 mm, ● – 1 mm (Bulgakova and Bulgakov 2001). The solid curve represents theoretical results obtained based on the revised thermal model (Bulgakova et al. 2004) with evaluated temperature of the onset of transition from normal vaporization to phase explosion marked by vertical dashed line. (Reprinted with permission from Yoo et al. (2000) (**a**) and Bulgakova and Bulgakov (2001) (**b**))

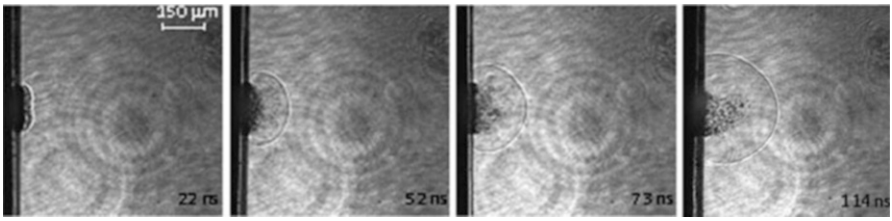

Fig. 29 Time-resolved images of ablation of aluminum by a Nd:YAG laser (pulse duration of 5 ns, wavelength of 1064 nm) at a laser fluence of 5.2 J/cm^2 under atmospheric conditions. (Adapted and reprinted with permission from Porneala and Willis (2009))

The thermal model in its several variations is a common tool for studies of nanosecond laser ablation of different materials, which enables prediction of the ablation thresholds and ablation rates in a wide range of laser fluences (Kelly and Miotello 1996; Bulgakov and Bulgakova 1999, 2001; Bulgakova et al. 2004, 2011; Gusarov and Smurov 2005; Anisimov 1968; Morozov 2004, 2006; Kelly and Miotello 1999; Prokhorov et al. 1990). The theoretical description of such a complicated phenomenon as phase explosion, however, is still challenging. For ultrashort laser ablation, phase explosion has been proven and widely simulated via application of the molecular dynamics method, for example, (Zhigilei et al. 2009; Zhigilei 2003; Zhigilei and Garrison 2000), but for longer laser pulses such

computationally-expensive models are not applicable. Several attempts are known to describe phase explosion at nanosecond laser pulses (see, e.g., Marla et al. 2014). Below we will discuss one of the modeling approaches, which provides insights into general features of the phase explosion process for metals irradiated by relatively long laser pulses (Mazzi et al. 2018). The model was developed in an attempt to quantitatively predict ejection of droplets upon pulsed laser ablation, usually attributed to phase explosion. The thermodynamic approach used in the model is valid for the timescales when the concept of local thermal equilibrium can be applied. The pressure acting on the molten surface is evaluated from the side of the vaporized material starting from the surface temperature (of the order of $0.90T_c$), while the ambient gas pressure is generally negligible. Under pulsed laser ablation of metals in vacuum, the metastable liquid may reach pressures of the order of 10^8 Pa due to the recoil vapor pressure.

In Mazzi et al. (2015), the dynamics of vapor bubble expansion in a metastable liquid was described on the basis of an original method proposed by Lee and Merte (1996). The phase explosion occurs, with vapor and liquid nanodroplets emission, when the volume fraction occupied by vapor bubbles (V_{vap}) reaches the value $\eta_{\max} = V_{\mathrm{vap}}/V_{\mathrm{tot}} = 0.3$ (V_{tot} is the total volume affected by the homogeneous nucleation). This value corresponds to a closely packed random distribution of bubbles, as explained in Mazzi et al. (2015), with additional numerical details provided in Mazzi et al. (2017), and Mazzi and Miotello (2017). Figure 30 presents an example of such simulations for the case of irradiation of a pure aluminum target by a 20 ns Gaussian laser pulse centered at 25 ns. The ablation yield as a function of the energy density *absorbed* by the target is shown in Fig. 30a, while the dynamics of ablation process for an absorbed laser fluence of 3.5 J/cm^2 is illustrated by Fig. 30b. The plots of the contributions of vaporization and phase explosion to the total ablation yield demonstrate how the vapor–nanoparticle mixture is generated as a function of time. First, normal vaporization takes place, while homogeneous nucleation needs some time to develop. As a result, phase explosion occurs at a delay with respect to the start of normal vaporization but still during the laser pulse, yielding the ejection of liquid nanoparticles. The droplet size histogram is presented in Fig. 30c in a log-log scale, showing a power law scaling for particles containing 10^3–10^4 atoms, while Fig. 30d shows a graphic representation of the spatial 3D distribution of the identified liquid nanodroplets obtained in the simulation performed at 3.5 J/cm^2. The droplet size distribution can be fitted to $f(N) \propto N^{-1.9}$, where N is the number of atoms per cluster. The exponent is quite independent on laser fluence since its value remains almost constant at fluences between 3.0 and 6.0 J/cm^2. The power law nanoparticle size distribution was also observed in molecular dynamics simulations of femtosecond laser ablation of aluminum (Wu and Zhigilei 2014). In the size distributions of aluminum nanoparticles, predicted at laser fluences of 3–4 J/cm^2, the average number of atoms per cluster is ~450, while the average particle size, calculated as the diameter of a spherical equivalent particle at room temperature, was of ~ 3.2 nm. This average size of the liquid nanodroplets directly ejected from the target is consistent with the experimental observations of pure metal nanoparticles synthesized by pulsed laser deposition in high vacuum using nanosecond laser pulses (Murray and Shin 2008; Alonso et al. 2009).

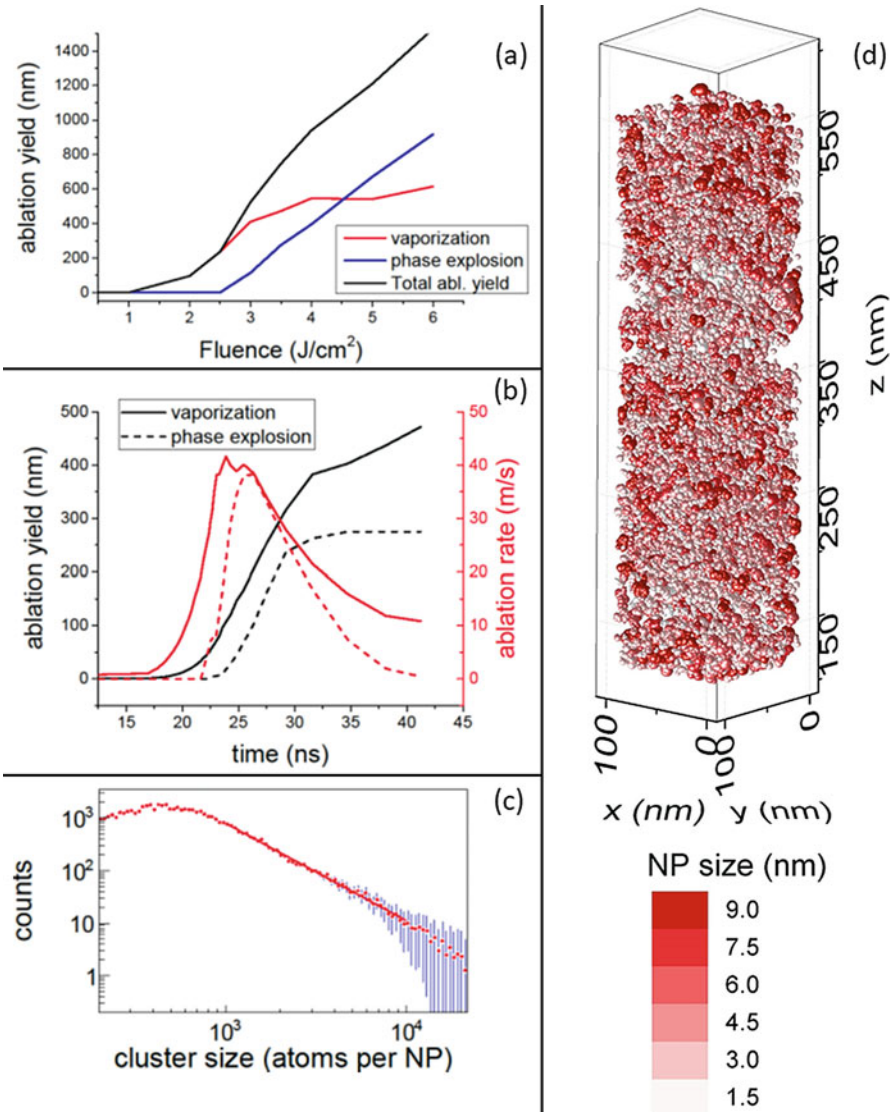

Fig. 30 (**a**) Ablation yield as a function of laser fluence calculated for single laser shots (20 ns FWHM) on aluminum. Red and blue lines indicate the contributions of normal vaporization and phase explosion, respectively. (**b**) Ablation yield (black lines, left axis) and ablation rate (red lines, right axis) as a function of time obtained at 3.5 J/cm^2 (absorbed energy density). The contributions of vaporization and phase explosion are shown by solid and dashed lines, respectively. (**c**) Size distribution of liquid nanodroplets identified in the simulations for the conditions of (**b**).Vertical blue lines are error bars, evaluated according to the Poisson statistics. (**d**) 3D distribution of liquid nanodroplets obtained in the simulations for the conditions of (**b**, **c**). The nanodroplets are presented as clusters of spheres. The droplet color depends on the cluster size. (Adapted from Mazzi et al. (2018))

Nanoparticle Formation by Pulsed Laser Ablation

As discussed in the previous Section, the formation of nanoparticles (NPs) is an essential part of pulsed laser ablation, which is directly correlated with the thermodynamic state of irradiated materials and the conditions in the laser ablation plume. Hence, the generation of nanoparticles by laser ablation is primarily a thermally driven process. As the size of NPs ranges between nanometers and several hundreds of nanometers, they can consist of several hundreds to millions of atoms/molecules. Nowadays, NPs constitute building blocks of nanotechnologies. Their optical, electrical, magnetic, catalytic, and other properties are unique compared to bulk materials and strongly depend on the size and size distribution of NPs, their composition, purity, and structure. Unique properties of NPs enable development of new nanostructured thin films and nanomaterials with desired functional characteristics. To achieve these goals, NPs synthesis must be controllable. Several techniques are commonly employed for NPs production such as wet chemical methods, mechanical grinding/milling of solids, arc discharge, combustion flame, and pulsed laser ablation (Su and Chang 2018). Among them, pulsed laser ablation has demonstrated a high flexibility and capacity for production of NPs of *any materials with high purity,* free of unwanted chemical residues.

Nanoparticles formation with the average size of ~10 nm by CW CO_2 laser action on solid oxide materials is known since 70s of twentieth century (Kato 1976). Interestingly, this phenomenon first attracted attention in astrophysics and planetary science communities (Hashimoto et al. 1979), and only later the potential of nanoparticle generation by laser ablation was realized by the laser-matter interaction community. Since that time, it was demonstrated that NPs can be formed in very different regimes of laser irradiation of solids, for example, Fig. 31. The applications utilizing NPs produced by laser ablation range from catalysis, imaging, energy, and environmental research and engineering to biomedicine, where NPs are used in both diagnostics and therapy.

In general, methods to produce nanoparticles and their aggregates can be classified from the viewpoint of two opposite strategies, *bottom-up* and *top-down*. In the bottom-up strategy, individual atoms or molecules are assembling into larger and more organized clusters and nanoparticles. In the top-down approach, large pieces of material are decomposed into smaller particles to create the required nanostructures. Schematically, the two strategies are shown in Fig. 32 (Su and Chang 2018).

In the pulsed laser ablation method of nanoparticle synthesis, both top-down and bottom-up processes are involved. As discussed above, phase explosion (a *top-down* process of material disintegration into the mixture of small droplets, clusters, and atoms/molecules) is one of the main thermal mechanisms of ablation at ultrafast laser pulses. This ablation mechanism can also be dominant at longer pulses above a certain laser fluence specific for each material, laser wavelength, and pulse duration (Fig. 1). The particles ejected in the course of phase explosion are growing further in the expending ablation plume via their coalescence with other particles and atomic/molecular components (*bottom-up* processes) (Zhigilei 2003). Additionally, individual atoms/molecules can condense in the vapor phase, thus forming clusters that can

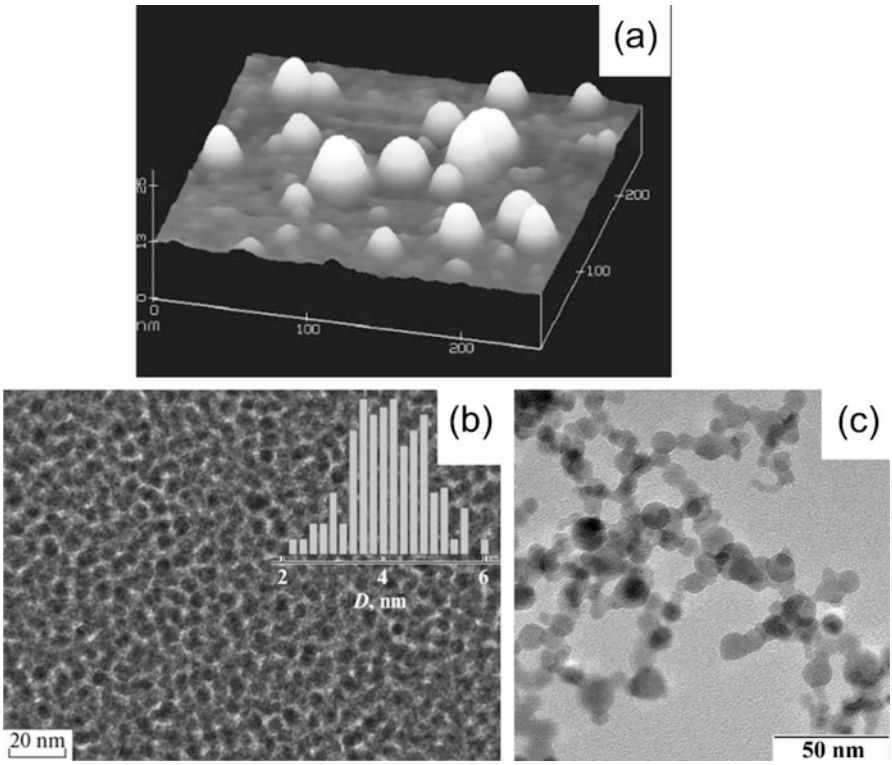

Fig. 31 Images of nanoparticles formed upon material ablation with femto-, nano-, and microsecond laser pulses. (**a**) Atomic force microscopy image of Al NPs deposited onto a silicon substrate using Ti:sapphire laser (50 fs pulse duration, 800 nm wavelength) (Eliezer et al. 2004). Scan size is 250 × 250 nm, the *z* range is 25 nm. (**b**) TEM images of gold NP films deposited onto amorphous carbon substrates in vacuum using Nd:YAG laser (532 nm wavelength, 7 ns pulse duration, laser fluence of 6 J/cm^2, 10,000 pulses, substrate temperature of 295 K) (Starinskiy et al. 2016). The inset shows the NP size distribution histogram. (**c**) Image of NPs obtained in the optimal pulse-periodic regime of evaporation of Nd:YAG targets by a ytterbium fiber laser LS-07N (wavelength of 1.07 μm, pulse duration of 120 μs, intensity of 0.4 MW/cm^2, velocity of beam scanning over the sample surface of 84 cm/s) (Osipov et al. 2018). (Reprinted with permission from Eliezer et al. (2004) (**a**), Starinskiy et al. (2016) (**b**), and Osipov et al. (2018) (**c**))

grow into nanoparticles. Theoretically, the insight into nanoparticle formation in the regime of phase explosion can be gained via molecular dynamic simulations (Wu and Zhigilei 2014; Zhigilei 2003; Zhigilei and Garrison 2000) or modeling based on the theory of homogeneous nucleation in a metastable liquid (see section "Phase Explosion or Explosive Boiling" and (Mazzi et al. 2015, 2017; Mazzi and Miotello 2017).

Laser irradiation with nanosecond and longer laser pulses, at laser fluences below the threshold for phase explosion (Fig. 1), results in thermal disintegration (vaporization) of most of the ejected material into individual atoms or molecules. During

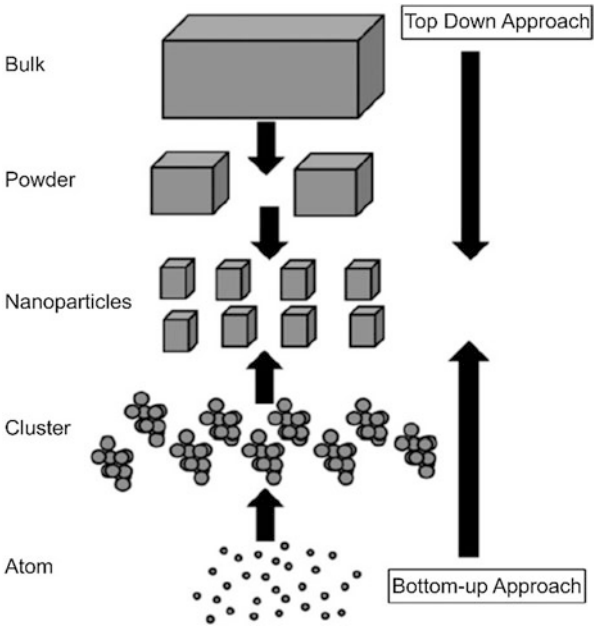

Fig. 32 Top-down and bottom-up strategies for NP production. (Reprinted with permission from Su and Chang (2018))

expansion into vacuum, gas environment at different pressures, or liquids (for review of nanoparticle generation in liquids see another chapter of this handbook (Gökce et al. 2020)), the atomic and molecular species experience condensation into clusters/nanoparticles. It must be noticed, however, that laser ablation of some materials (primarily semiconductors as well as carbon, phosphorus, and some others) at relatively small laser fluences, slightly above the ablation threshold, can produce a nonthermal ejection of small clusters, which serve as building blocks for nanoparticle growth in the ablation plume (Gaumet et al. 1993; Kanasaki et al. 1995; Bulgakov et al. 2000, 2010). Interestingly, an increase in laser fluence (still below the phase explosion threshold) may result in a reduction in the cluster emission or even in complete atomization of the ablation products (Gaumet et al. 1993). The nonthermal cluster emission can be followed by cluster growth via gas phase condensation, which is essentially a *thermal* process, making the complicated laser-induced synthesis of nanoparticles even more challenging for the theoretical description.

The condensation of the ablation products in the expanding laser-produced plume can be modeled on the basis of Zeldovich and Raizer theory of condensation (Kuwata et al. 2001; Zeldovich and Raizer 1966). For this purpose, a gasdynamic model of laser ablation plume expansion in vacuum or an ambient gas is supplemented by equations describing kinetics of cluster growth. Initially, upon vaporization from a laser-irradiated surface, the ablation vapor is hot and dense. As the vapor cools down during the expansion, the vapor becomes supersaturated,

which initiates the condensation process. The condensation kinetics is governed by the degree of undercooling, which is defined as

$$\theta = \frac{T_{eq} - T}{T_{eq}}. \tag{17}$$

Here T_{eq} is the equilibrium (or saturation) temperature, which is determined from the Clausius-Clapeyron relation involving the equation-of-state of the vapor (Zeldovich and Raizer 1966). The condensation can be considered as a two-step process: (1) formation of critical nuclei (or centers of condensation), which are able to further grow, and (2) their subsequent growth. These two steps are described by two equations, for the rate of nucleation R (number of viable nuclei created in unit volume per unit time) and for the rate of cluster growth, which is equal to the difference in the rates of sticking of molecules to a growing cluster and evaporation back from the cluster surface to the vapor phase. The dependence of the rate of nucleation on the degree of undercooling can be expressed as (Zeldovich and Raizer 1966)

$$R = C \exp\left(-b/\theta^2\right), \tag{18}$$

where $C = 2n\bar{v}V_a\sqrt{\gamma_{lv}/k_BT}$ and $b = 16\pi\gamma_{lv}^3V_a^2/(3k_BT\Delta H_v^2)$. Here n and $\bar{v}$ are the number density of vapor particles and their average velocity, respectively. The rate of cluster growth also depends on the degree of undercooling and can be written as (Zeldovich and Raizer 1966)

$$\frac{dg}{dt} = 4\pi r^2 n\bar{v}(1 - \exp(-\Delta H_v\theta/k_BT)), \tag{19}$$

where g is number of atoms or molecules in the growing cluster and r is the radius of the growing cluster.

The approach described above enables a quantitative description of the nanoparticle formation in pulsed laser ablation of relatively simple substances, which do not form particles with "magic" numbers of atoms upon condensation in the vapor phase. One of the most striking examples of the "magic clusters" is fullerene that can be produced in laser ablation cluster source (Kroto et al. 1985). It was also found that laser ablation of phosphorus results in "magic clusters" observed in time-of-flight spectra (Bulgakov et al. 2000) whose hollow (fullerene-type) structures were predicted theoretically (Kosyakov and Vasil'eva 1979). For the clusters with "magic" numbers of atoms, Smoluchowski rate equations (Smoluchowski 1916), which govern the nanoparticle evolution, allow reproducing the major features of the cluster size distributions observed experimentally for laser ablation (Bernholc and Phillips 1986; Creasy 1990; Bulgakova and Bulgakov 2007)

$$\frac{dn_j}{dt} = \frac{1}{2}\sum_{l=1}^{j-1} K_{l,j-l}n_l n_{j-l} - n_j\sum_{l=1}^{N} K_{l,j}n_l. \tag{20}$$

Here n_j is the density of the clusters with j atoms per cluster. The reaction rates for cluster formation as a result of collision of clusters consisting of l and j atoms are

written as $K_{j,l} = A_s^{j+l} \sigma_{j,l} u_{\text{rel}}$, where u_{rel} is the relative velocity of the colliding particles, A_s^{j+l} is the reaction efficiency of the colliding particles with respect to the production of a cluster with the number of atoms $(j + l)$, and $\sigma_{j,l}$ is the cross section for elastic collisions of the reacting clusters, which is usually determined from the known experimental data (Bulgakova and Bulgakov 2007; von Helden et al. 1993) or calculated based on geometry of the clusters (Nerushev and Sukhinin 1995).

As mentioned above, high purity nanoparticles of various compositions can be synthesized by pulsed laser ablation due to the high flexibility of this technique with respect to the choice of irradiation conditions and the possibility of avoiding any contamination. However, the gas-phase NP synthesis by laser ablation still calls for more research to achieve a better control over particle size distribution, which is usually rather broad. The rate of NP production and size distribution of the laser-generated nanoparticles can be varied by changing the air pressure or airbrushing that provides quenching of NP growth (Barcikowski et al. 2007). Upon gentle nanosecond laser ablation, when only small clusters consisting of a few atoms are formed in the plume, nanoparticles can nucleate on a substrate upon deposition, thus forming nanostructured films (Starinskiy et al. 2016; Dolbec et al. 2004). The mechanism of nanoparticle formation on the surface is explained by migration of energetic atoms and ions arriving to the substrate. The critical radius for the nucleation on the substrate strongly depends on its temperature, which provides one more degree of freedom for controlling nanoparticle average size and size distribution. However, at present, the most efficient method for synthesis of NPs by laser ablation is the formation of colloidal solution of NPs with relatively narrow size distribution through pulsed laser ablation in a liquid environment. This method is discussed in detail in another chapter of this handbook (Gökce et al. 2020).

Concluding Remarks

This chapter provides a broad overview of a range of thermal processes that can be triggered in different types of materials by short and ultrashort laser pulse irradiation. While the mechanisms of laser excitation and relaxation of the excited states have strong dependence on the electronic structure of irradiated materials and on the strength of the electron-phonon coupling, the processes that follow the thermalization of the deposited energy are usually less material-specific and may have similar general characteristics. The sequence of laser-induced thermal processes may include the generation of thermoelastic stresses, melting and solidification, vaporization and, at sufficiently high laser fluences, phase explosion and plasma formation. A clear understanding of the microscopic mechanisms, thermodynamic driving forces, and kinetics of each of these processes is critical for achieving control over the practical outcomes of laser irradiation, such as the generation (or annealing) of crystal defects, formation of amorphous or metastable crystalline phases, as well as complex surface morphology produced by the interplay of phase explosion, melt flow driven by ablation recoil pressure and gradients of surface tension, and

resolidification. Moreover, the growing number of applications based on the generation of nanoparticles by laser ablation in different environments (vacuum, controlled atmosphere, or liquid) puts onus on theory and modeling to quantitatively predict the populations of atomic clusters and nano/microparticles generated by material spallation, melt expulsion, phase explosion, and/or condensation in the expanding ablation plume.

The application of well-established theoretical tools, such as classical nucleation theory and kinetic description of diffusional phase transformations, provides a common ground for analysis of laser-induced melting, solidification, cavitation, vaporization, and boiling, but also exposes the limitations of the theoretical tools developed for close-to-equilibrium conditions. Indeed, the rapid localized heating by laser irradiation can bring material to a state of strong thermodynamic and mechanical nonequilibrium, thus inducing the structural and phase transformations that cannot be realized in conventional thermal and mechanical processing. The high cooling rates associated with strong spatial localization of the laser excitation and steep temperature gradients, on the other hand, can freeze the unusual metastable phases, defect structures, and surface morphologies. The description of the phase transformations occurring under conditions of extreme heating and cooling rates, when the size of a critical nucleus decreases down to nanometers and a phase transformation either proceeds in an explosive manner (in melting and boiling) or is prevented by rapid quenching (in solidification), is challenging and calls for a critical assessments of the existing theoretical treatments. The progress in the theory of laser material interactions is facilitated by the results of *in situ* experimental probing and multiscale computational modeling of laser-induced processes.

Finally, we note that the same highly nonequilibrium character of material transformations in laser processing that presents a challenge for theoretical and computational treatment also creates unique opportunities for investigation of nonequilibrium phenomena occurring under extreme thermodynamic conditions of high pressure and high temperature. This capability of lasers enables a remarkable comparison between processes that take place in controlled way in the laboratory and possible processes occurring in planetary cores or under warm dense matter conditions. On the practical side, the flexibility of the irradiation parameters of laser sources and the diversity of available laser systems offer opportunities for an effective tailoring of material properties, designing new materials, and fabricating functional structures of interest in various fields, ranging from optics and mechanics to sensors, photocatalysis, and drug delivery.

Cross-References

- ► Acoustic Emission and Ultrasound Monitoring in Laser Micro/Nanofabrication
- ► Generation and Annealing of Crystalline Disorder in Laser Processing of Silicon
- ► Laser Ablation in Liquids for Nanomaterial Synthesis and Applications
- ► Laser Cleaning of Contaminated Substrate Surfaces

- ▶ Laser Coupling and Relaxation of the Absorbed Energy: Metals, Semiconductors, and Dielectrics
- ▶ Laser-Induced Surface Modification for Photovoltaic Device Applications
- ▶ Laser Synthesis of Colloids: Applications
- ▶ Laser-Induced Forward Transfer Applications in Micro-engineering
- ▶ Laser-Induced Non-thermal Processes
- ▶ Laser-Induced Periodic Surface Structures (LIPSS)
- ▶ Laser-Induced Processing of Nanoparticles and Growth of Nanowires
- ▶ Microstructure Modification: Generation of Crystal Defects and Phase Transformations
- ▶ Pulsed Laser Deposition: Fundamentals, Applications, and Perspectives

Acknowledgments M.V.S., M.H., and L.V.Z. acknowledge financial support provided by the National Science Foundation (NSF) through Grants CMMI-1562929, CMMI-1663429, DMR-1610936, and DMR-1708486. Y.L. and N.M.B. acknowledge support of the European Regional Development Fund and the state budget of the Czech Republic (project BIATRI, No. CZ.02.1.01/0.0/0.0/15_003/0000445; project HiLASE CoE, No. CZ.02.1.01/0.0/0.0/15_006/0000674; programme NPU I, project No. LO1602). Computational support enabling large-scale atomistic modeling was provided by the Oak Ridge Leadership Computing Facility (INCITE project MAT130) and NSF through the Extreme Science and Engineering Discovery Environment (project TG-DMR110090). The authors also appreciate the help provided by Mikhail Arefev with preparation of Fig. 16.

References

Abou-Saleh A, Karim ET, Maurice C, Reynaud S, Pigeon F, Garrelie F, Zhigilei LV, Colombier JP (2018) Spallation-induced roughness promoting high spatial frequency nanostructure formation on Cr. Appl Phys A Mater Sci Process 124:308

Agranat MB, Ashitkov SI, Fortov VE, Kirillin AV, Kostanovskii AV, Anisimov SI, Kondratenko PS (1999) Use of optical anisotropy for study of ultrafast phase transformations at solid surfaces. Appl Phys A Mater Sci Process 69:637

Almeida R, Hood ES (1992) Nonequilibrium dynamics in thermal desorption. J Phys Chem 96:3086

Alonso JC, Diamant R, Castillo P, Acosta-García MC, Batina N, Haro-Poniatowski E (2009) Thin films of silver nanoparticles deposited in vacuum by pulsed laser ablation using a YAG:Nd laser. Appl Surf Sci 255:4933

Anisimov SI (1968) Vaporization of metal absorbing laser radiation. Sov Phys JETP 27:182

Anisimov SI, Kapeliovich BL, Perel'man TL (1974) Electron emission from metal surfaces exposed to ultrashort laser pulses. Sov Phys JETP 39:375

Arblaster JW (2016) Thermodynamic properties of gold. J Phase Equilib Diff 37:229

Ashitkov SI et al (2002) Ultrafast laser-induced phase transitions in tellurium. J Exp Theor Phys Lett 76:461

Ashitkov SI, Inogamov NA, Zhakhovskii VV, Emirov YN, Agranat MB, Oleinik II, Anisimov SI, Fortov VE (2012) Formation of nanocavities in the surface layer of an aluminum target irradiated by a femtosecond laser pulse. JETP Lett 95:176

Ashkenazy Y, Averback RS (2010) Kinetic stages in the crystallization of deeply undercooled body-centered-cubic and face-centered-cubic metals. Acta Mater 58:524

Baffou G, Rigneault H (2011) Femtosecond-pulsed optical heating of gold nanoparticles. Phys Rev B 84:035415

Balling P (2020) Laser coupling and relaxation of the absorbed energy: metals, semiconductors and dielectrics. In: Handbook of laser micro- and nano-engineering. Springer, Cham
Barcikowski S, Hahn A, Kabashin AV, Chichkov BN (2007) Properties of nanoparticles generated during femtosecond laser machining in air and water. Appl Phys A Mater Sci Process 87:47
Barin I, Platzki G (1995) Thermochemical data of pure substances. VCH/Weinheim, New York
Baskes MI, Stan M (2003) An atomistic study of solid/liquid interfaces and phase equilibrium in binary systems. Metall Mater Trans A 34:435
Bäuerle D (2000) Laser processing and chemistry. Springer, Berlin/Heidelberg
Bernholc J, Phillips JC (1986) Kinetics of cluster formation in the laser vaporization source: Carbon clusters. J Chem Phys 85:3258
Billings BH, Gray DE (1972) American institute of physics handbook, 3rd edn. McGraw-Hill, New York
Biswas K, Chattopadhyay K (2007) Microstructural evolution during laser resolidification of Fe-25 atom percent Ge alloy. Metall Mater Trans A 38:1395
Bonse J, Rosenfeld A, Krüger J (2009) On the role of surface plasmon polaritons in the formation of laser-induced periodic surface structures upon irradiation of silicon by femtosecond-laser pulses. J Appl Phys 106:104910
Bonse J, Höhm S, Kirner SV, Rosenfeld A, Krüger J (2017) Laser-induced periodic surface structures – a scientific evergreen. IEEE J Sel Top Quantum Electron 23:1
Broughton JQ, Gilmer GH, Jackson KA (1982) Crystallization rates of a Lennard-Jones liquid. Phys Rev Lett 49:1496
Buividas R, Mikutis M, Juodkazis S (2014) Surface and bulk structuring of materials by ripples with long and short laser pulses: recent advances. Prog Quantum Electron 38:119
Bulgakov AV, Bulgakova NM (1998) Gas-dynamic effects of the interaction between a pulsed laser-ablation plume and the ambient gas: analogy with an underexpanded jet. J Phys D 31:693
Bulgakov AV, Bulgakova NM (1999) Thermal model of pulsed laser ablation under the conditions of formation and heating of a radiation-absorbing plasma. Quantum Electron 29:433
Bulgakov AV, Bobrenok OF, Kosyakov VI (2000) Laser ablation synthesis of phosphorus clusters. Chem Phys Lett 320:19
Bulgakov AV, Evtushenko AB, Shukhov YG, Ozerov I, Marin W (2010) Pulsed laser ablation of binary semiconductors: mechanisms of vaporisation and cluster formation. Quantum Electron 40:1021
Bulgakova NM, Bulgakov AV (2001) Pulsed laser ablation of solids: transition from normal vaporization to phase explosion. Appl Phys A Mater Sci Process 73:199
Bulgakova NM, Bulgakov AV (2007) Numerical study of gas-phase cluster synthesis under ns laser ablation. Proc SPIE 6732:67320G
Bulgakova NM, Bulgakov AV, Babich LP (2004) Energy balance of pulsed laser ablation: thermal model revised. Appl Phys A Mater Sci Process 79:1323
Bulgakova NM, Stoian R, Rosenfeld A, Hertel IV, Marine W, Campbell EEB (2005) A general continuum approach to describe fast electronic transport in pulsed laser irradiated materials: the problem of Coulomb explosion. Appl Phys A Mater Sci Process 81:345
Bulgakova NM, Evtushenko AB, Shukhov YG, Kudryashov SI, Bulgakov AV (2011) Role of laser-induced plasma in ultradeep drilling of materials by nanosecond laser pulses. Appl Surf Sci 257:10876
Burke E, Broughton JQ, Gilmer GH (1988) Crystallization of fcc (111) and (100) crystal-melt interfaces: a comparison by molecular dynamics for the Lennard-Jones system. J Chem Phys 89:1030
Buvailo A, Xing Y, Hines J, Borguet E (2011) Thin polymer film based rapid surface acoustic wave humidity sensors. Sensors Actuators B Chem 156:444
Byskov-Nielsen J, Savolainen J-M, Christensen MS, Balling P (2011) Ultra-short pulse laser ablation of copper, silver and tungsten: experimental data and two-temperature model simulations. Appl Phys A Mater Sci Process 103:447
Cahn RW (1989) New ideas for the melting pot. Nature 342:619
Cahn RW (2001) Melting from within. Nature 413:582

Cangueiro LT, Cavaleiro AJ, Morgiel J, Vilar R (2016) Mechanisms of the formation of low spatial frequency LIPSS on Ni/Ti reactive multilayers. J Phys D 49:365103
Černý R, Šáršik R, Lukeš I, Cháb V (1991) Excimer-laser-induced melting and solidification of monocrystalline Si: equilibrium and nonequilibrium models. Phys Rev B 44:4097
Chan W-L, Averback RS, Cahill DG, Lagoutchev A (2008) Dynamics of femtosecond laser-induced melting of silver. Phys Rev B 78:214107
Chan W-L, Averback RS, Cahill DG, Ashkenazy Y (2009) Solidification velocities in deeply undercooled silver. Phys Rev Lett 102:095701
Chase MW, Davies CA, Downey JR, Frurip DJ, McDonald RA, Syverud AN (1985) JANAF thermochemical tables, 3rd edn. J Phys Chem Ref Data 14(Suppl 1)
Cheaito R et al (2015) Thermal boundary conductance accumulation and interfacial phonon transmission: measurements and theory. Phys Rev B 91:035432
Chen J, Chen W-K, Tang J, Rentzepis PM (2011) Time-resolved structural dynamics of thin metal films heated with femtosecond optical pulses. Proc Natl Acad Sci U S A 108:18887
Choi G-M, Wilson RB, Cahill DG (2014) Indirect heating of Pt by short-pulse laser irradiation of Au in a nanoscale Pt/Au bilayer. Phys Rev B 89:064307
Coriell SR, Turnbull D (1982) Relative roles of heat transport and interface rearrangement rates in the rapid growth of crystals in undercooled melts. Acta Metall 30:2135
Creasy WR (1990) Some model calculations of carbon cluster growth kinetics. J Chem Phys 92:7223
Dash JG (1999) History of the search for continuous melting. Rev Mod Phys 71:1737
Denison DR (1969) Phonic desorption. J Vac Sci Technol 6:214
Dolbec R, Irissou E, Chaker M, Guay D, Rosei F, El Khakani MA (2004) Growth dynamics of pulsed laser deposited Pt nanoparticles on highly oriented pyrolitic graphite substrates. Phys Rev B 70:201406
Dow AR, Wittrig AM, Kenttämaa HI (2012) Laser-induced acoustic desorption mass spectrometry. Eur J Mass Spectrom 18:77
Dumitrica T, Burzo A, Dou Y, Allen RE (2004) Response of Si and InSb to ultrafast laser pulses. Phys Status Solidi B 241:2331
Dwyer JR, Hebeisen CT, Ernstorfer R, Harb M, Deyirmenjian VB, Jordan RE, Dwayne Miller RJ (2006) Femtosecond electron diffraction: 'making the molecular movie'. Philos Trans Royal Soc A 364:741
Dzegilenko FN, Uzer T, Herbst E (1996) Classical studies of shock wave-induced desorption for model adsorbates. J Chem Phys 105:10868
Egry I, Ricci E, Novakovic R, Ozawa S (2010) Surface tension of liquid metals and alloys – recent developments. Adv Colloid Interf Sci 159:198
Ehlert S, Walte A, Zimmermann R (2013) Ambient pressure laser desorption and laser-induced acoustic desorption ion mobility spectrometry detection of explosives. Anal Chem 85:11047
Ehrler J et al (2018) Laser-rewriteable ferromagnetism at thin-film surfaces. ACS Appl Mater Interfaces 10:15232
Eliezer S et al (2004) Synthesis of nanoparticles with femtosecond laser pulses. Phys Rev B 69:144119
Elliott WA, Gagliano FP, Krauss G (1972) Rapid cooling by laser melt quenching. Appl Phys Lett 21:23
Fang TH, Li WL, Tao NR, Lu K (2011) Revealing extraordinary intrinsic tensile plasticity in gradient nano-grained copper. Science 331:1587
Feng Q, Picard YN, Liu H, Yalisove SM, Mourou G, Pollock TM (2005) Femtosecond laser micromachining of a single-crystal superalloy. Scr Mater 53:511
Fröhlingsdorf J, Stritzker B (1986) Amorphous gallium produced by pulsed excimer laser irradiation. In: Draper CW, Mazzoldi P (eds) Laser surface treatment of metals. Springer Netherlands, Dordrecht, p 133
Fucke W, Seydel U (1980) Improved experimental determination of critical-point data for tungsten. High Temp High Pressure 12:419

Gäumann M, Trivedi R, Kurz W (1997) Nucleation ahead of the advancing interface in directional solidification. Mater Sci Eng A 226–228:763

Gaumet JJ, Wakisaka A, Shimizu Y, Tamori Y (1993) Energetics for carbon clusters produced directly by laser vaporization of graphite: dependence on laser power and wavelength. J Chem Soc Faraday Trans 89:1667

Giammanco F, Giorgetti E, Marsili P, Giusti A (2010) Experimental and theoretical analysis of photofragmentation of Au nanoparticles by picosecond laser radiation. J Phys Chem C 114:3354

Gill SC, Kurz W (1995) Rapidly solidified Al-Cu alloys – II. Calculation of the microstructure selection map. Acta Mater 43:139

Gill-Comeau M, Lewis LJ (2011) Ultrashort-pulse laser ablation of nanocrystalline aluminum. Phys Rev B 84:224110

Gloor GJ, Jackson G, Blas FJ, de Miguel E (2005) Test-area simulation method for the direct determination of the interfacial tension of systems with continuous or discontinuous potentials. J Chem Phys 123:134703

Gökce B, Rehbock C, Ramesh V, Kohsakowski S, Hupfeld T, Reichenberger S, Barcikowski S (2020) Laser synthesis of colloids: applications. In: Handbook of laser micro- and nano-engineering. Springer, Cham

Goldenfeld N (1992) Lectures on phase transitions and the renormalization group. Addison-Wesley/Advanced Book Program, Reading

Golovlev VV, Allman SL, Garrett WR, Chen CH (1997a) Laser-induced acoustic desorption of electrons and ions. Appl Phys Lett 71:852

Golovlev VV, Allman SL, Garrett WR, Taranenko NI, Chen CH (1997b) Laser-induced acoustic desorption. Int J Mass Spectrom Ion Process 169–170:69

Grabow MH, Gilmer GH, Bakker AF (1988) Molecular dynamics studies of silicon solidification and melting. MRS Proc 141(349):349

Guggenheim EA (1945) The principle of corresponding states. J Chem Phys 13:253

Gurevich EL, Levy Y, Gurevich SV, Bulgakova NM (2017) Role of the temperature dynamics in formation of nanopatterns upon single femtosecond laser pulses on gold. Phys Rev B 95:054305

Gusarov AV, Smurov I (2005) Thermal model of nanosecond pulsed laser ablation: analysis of energy and mass transfer. J Appl Phys 97:014307

Hamilton MF, Il'insky YA, Zabolotskaya EA (1995) Local and nonlocal nonlinearity in Rayleigh waves. J Acoust Soc Am 97:882

Hashimoto K-Y (2000) Surface acoustic wave devices in telecommunications: modelling and simulation. Springer, Berlin/Heidelberg

Hashimoto K, Masumoto T (1983) Corrosion properties of amorphous alloys. In: Hasegawa R (ed) Glassy metals: magnetic, chemical, and structural properties. CRC Press University of California, Boca Raton

Hashimoto A, Kumazawa M, Onuma N (1979) Evaporation metamorphism of primitive dust material in the early solar nebula. Earth Planet Sci Lett 43:13

Hashimoto S, Werner D, Uwada T (2012) Studies on the interaction of pulsed lasers with plasmonic gold nanoparticles toward light manipulation, heat management, and nanofabrication. J Photochem Photobiol C 13:28

He M, Wu C, Shugaev MV, Samolyuk GD, Zhigilei LV (2019) Computational study of short pulse laser induced generation of crystal defects in Ni-based single-phase binary solid solution alloys. J Phys Chem C 123:2202

Hoekstra JG, Qadri SB, Scully JR, Fitz-Gerald JM (2005) Laser surface modification of a crystalline Al-Co-Ce alloy for enhanced corrosion resistance. Adv Eng Mater 7:805

Hopkins PE, Salaway RN, Stevens RJ, Norris PM (2007) Temperature-dependent thermal boundary conductance at Al/Al_2O_3 and Pt/Al_2O_3 interfaces. Int J Thermophys 28:947

Howe JM (1997) Interfaces in materials: atomic structure, thermodynamics and kinetics of solid-vapor, solid-liquid and solid-solid interfaces. Wiley, New York

Hoyt JJ, Asta M (2002) Atomistic computation of liquid diffusivity, solid-liquid interfacial free energy, and kinetic coefficient in Au and Ag. Phys Rev B 65:214106

Hu M, Poulikakos D, Grigoropoulos CP, Pan H (2010) Recrystallization of picosecond laser-melted ZnO nanoparticles in a liquid: a molecular dynamics study. J Chem Phys 132:164504
Huang SM, Hong MH, Lukiyanchuk B, Chong TC (2003) Nanostructures fabricated on metal surfaces assisted by laser with optical near-field effects. Appl Phys A Mater Sci Process 77:293
Huber C, Trügler A, Hohenester U, Prior Y, Kautek W (2014) Optical near-field excitation at commercial scanning probe microscopy tips: a theoretical and experimental investigation. Phys Chem Chem Phys 16:2289
Hultgren R, Desai PD, Hawkins DT, Gleiser M, Kelley KK, Wagman DD (1973) Selected values of the thermodynamic properties of the elements. American Society for Metals, Metals Park
Hunziker O, Kurz W (1997) Solidification microstructure maps in NiAl alloys. Acta Mater 45:4981
Hwang D, Ryu S-G, Misra N, Jeon H, Grigoropoulos CP (2009a) Nanoscale laser processing and diagnostics. Appl Phys A Mater Sci Process 96:289
Hwang TY, Vorobyev AY, Guo C (2009b) Surface-plasmon-enhanced photoelectron emission from nanostructure-covered periodic grooves on metals. Phys Rev B 79:085425
Inoue Y (2007) Effects of acoustic waves-induced dynamic lattice distortion on catalytic and adsorptive properties of metal, alloy and metal oxide surfaces. Surf Sci Rep 62:305
Inoue Y (2019) Acoustic enhancement of surface reactions. MRS Bull 44:361
Inoue Y, Matsukawa M, Sato K (1989) Effect of surface acoustic wave generated on ferroelectric support upon catalysis. J Am Chem Soc 111:8965
Ionin AA, Kudryashov SI, Ligachev AE, Makarov SV, Seleznev LV, Sinitsyn DV (2011) Nanoscale cavitation instability of the surface melt along the grooves of one-dimensional nanorelief gratings on an aluminum surface. JETP Lett 94:266
Ivanov DS, Zhigilei LV (2003a) Combined atomistic-continuum modeling of short-pulse laser melting and disintegration of metal films. Phys Rev B 68:064114
Ivanov DS, Zhigilei LV (2003b) Effect of pressure relaxation on the mechanisms of short-pulse laser melting. Phys Rev Lett 91:105701
Ivanov DS, Zhigilei LV (2004) Combined atomistic-continuum model for simulation of laser interaction with metals: application in the calculation of melting thresholds in Ni targets of varying thickness. Appl Phys A Mater Sci Process 79:977
Ivanov DS, Zhigilei LV (2007) Kinetic limit of heterogeneous melting in metals. Phys Rev Lett 98:195701
Ivanov DS, Lin Z, Rethfeld B, O'Connor GM, Glynn TJ, Zhigilei LV (2010) Nanocrystalline structure of nanobump generated by localized photoexcitation of metal film. J Appl Phys 107:013519
Jackson KA (2002) The interface kinetics of crystal growth processes. Interface Sci 10:159
Jackson KA, Chalmers B (1956) Kinetics of solidification. Can J Phys 34:473
Jeschke HO, Diakhate MS, Garcia ME (2009) Molecular dynamics simulations of laser-induced damage of nanostructures and solids. Appl Phys A Mater Sci Process 96:33
Jin ZH, Gumbsch P, Lu K, Ma E (2001) Melting mechanisms at the limit of superheating. Phys Rev Lett 87:055703
Jo MC, Guldiken R (2013) Dual surface acoustic wave-based active mixing in a microfluidic channel. Sensors Actuators B Chem 196:1
Kanasaki J, Okano A, Ishikawa K, Nakai Y, Itoh N (1995) The DIET from semiconductor surfaces by excitation of valence electrons. Nucl Instrum Methods Phys Res B 101:93
Kapat JS, Wei Z, Kumar A (1998) Role of kinetics in laser processing. Appl Surf Sci 127–129:212
Karim ET, Lin Z, Zhigilei LV (2012) Molecular dynamics study of femtosecond laser interactions with Cr targets. AIP Conf Proc 1464:280
Karim ET, Wu C, Zhigilei LV (2014) Molecular dynamics simulations of laser-materials interactions: general and material-specific mechanisms of material removal and generation of crystal defects. In: Veiko VP, Konov VI (eds) Fundamentals of laser-assisted micro- and nanotechnologies. Springer International Publishing, Cham, p 27
Kaspar J, Luft A (2001) Microstructure formed in body centred cubic metals by laser shock processing. Surf Eng 17:379

Kasuya D, Kokai F, Takahashi K, Yudasaka M, Iijima S (2001) Formation of C_{60} using CO_2 laser vaporization of graphite at room temperature. Chem Phys Lett 337:25
Kato M (1976) Preparation of ultrafine particles of refractory oxides by gas-evaporation method. Jpn J Appl Phys 15:757
Kelling S, King DA (1998) Acoustic wave enhancement of catalytic reaction rates over platinum surfaces. Platin Met Rev 42:8
Kelling S, Mitrelias T, Matsumoto Y, Ostanin VP, King DA (1997) Acoustic wave enhancement of the catalytic oxidation of carbon monoxide over Pt{110}. J Chem Phys 107:5609
Kelling S, Cerasari S, Rotermund HH, Ertl G, King DA (1998) A photoemission electron microscopy (PEEM) study of the effect of surface acoustic waves on catalytic CO oxidation over Pt {110}. Chem Phys Lett 293:325
Kelly A (2000) Crystallography and crystal defects. Wiley, Chichester/New York
Kelly R, Dreyfus RW (1988) On the effect of Knudsen-layer formation on studies of vaporization, sputtering, and desorption. Surf Sci 198:263
Kelly R, Miotello A (1996) Comments on explosive mechanisms of laser sputtering. Appl Surf Sci 96–98:205
Kelly R, Miotello A (1999) Contribution of vaporization and boiling to thermal-spike sputtering by ions or laser pulses. Phys Rev E 60:2616
Knacke O, Kubaschewski O, Hesselmann K (1991) Thermochemical properties of inorganic substances. Springer/Verlag Stahleisen, Berlin/New York/Düsseldorf
Knight CJ (1979) Theoretical modeling of rapid surface vaporization with back pressure. AIAA J 17:519
Koch J, Korte F, Bauer T, Fallnich C, Ostendorf A, Chichkov BN (2005) Nanotexturing of gold films by femtosecond laser-induced melt dynamics. Appl Phys A Mater Sci Process 81:325
Kosyakov VI, Vasil'eva IG (1979) Phosphorous rings, clusters, chains and layers. Russ Chem Rev 48:153
Kozhushko VV, Lomonosov AM, Hess P (2007) Intrinsic strength of silicon crystals in pure- and combined-mode fracture without precrack. Phys Rev Lett 98:195505
Krischer C, Lichtman D (1973) Observation of desorption from quartz induced by surface acoustic waves. Phys Lett A 44:99
Kroto HW, Heath JR, O'Brien SC, Curl RF, Smalley RE (1985) C_{60}: Buckminsterfullerene. Nature 318:162
Kurz W (2001) Solidification microstructure-processing maps: theory and application. Adv Eng Mater 3:443
Kuwata M, Luk'yanchuk B, Yabe T (2001) Nanocluster formation within the vapor plume, produced by nanosecond-laser ablation: effect of initial density and pressure distributions. Jpn J Appl Phys 40:4262
Kuznetsov AI, Unger C, Koch J, Chichkov BN (2012) Laser-induced jet formation and droplet ejection from thin metal films. Appl Phys A Mater Sci Process 106:479
Lapotko D, Lukianova E, Potapnev M, Aleinikova O, Oraevsky A (2006) Method of laser activated nano-thermolysis for elimination of tumor cells. Cancer Lett 239:36
Le Harzic R, Huot N, Audouard E, Jonin C, Laporte P, Valette S, Fraczkiewicz A, Fortunier R (2002) Comparison of heat-affected zones due to nanosecond and femtosecond laser pulses using transmission electronic microscopy. Appl Phys Lett 80:3886
Lee HS, Merte H (1996) Spherical vapor bubble growth in uniformly superheated liquids. Int J Heat Mass Transf 39:2427
Lemaster JE, Jokerst JV (2017) What is new in nanoparticle-based photoacoustic imaging? Wiley Interdiscip Rev Nanomed Nanobiotechnol 9:e1404
Leveugle E, Zhigilei LV (2004) Microscopic mechanisms of short pulse laser spallation of molecular solids. Appl Phys A Mater Sci Process 79:753
Leveugle E, Ivanov DS, Zhigilei LV (2004) Photomechanical spallation of molecular and metal targets: molecular dynamics study. Appl Phys A Mater Sci Process 79:1643

Levy Y, Derrien TJY, Bulgakova NM, Gurevich EL, Mocek T (2016) Relaxation dynamics of femtosecond-laser-induced temperature modulation on the surfaces of metals and semiconductors. Appl Surf Sci 374:157
Lin B, Elsayed-Ali HE (2002) Temperature dependent reflection electron diffraction study of In (111) and observation of laser-induced transient surface superheating. Surf Sci 498:275
Lin CJ, Spaepen F (1983) Metallic glasses and metastable crystalline phases produced by picosecond pulsed laser quenching. MRS Proc 28:75
Lin CJ, Spaepen F (1986) Nickel-niobium alloys obtained by picosecond pulsed laser quenching. Acta Metall 34:1367
Lin Z, Zhigilei LV (2006) Time-resolved diffraction profiles and atomic dynamics in short-pulse laser-induced structural transformations: molecular dynamics study. Phys Rev B 73:184113
Lin Z, Zhigilei LV (2007a) Temperature dependences of the electron–phonon coupling, electron heat capacity and thermal conductivity in Ni under femtosecond laser irradiation. Appl Surf Sci 253:6295
Lin Z, Zhigilei LV (2007b) Time-resolved diffraction profiles and structural dynamics of Ni film under short laser pulse irradiation. J Phys Conf Ser 59:11
Lin C-J, Spaepen F, Turnbull D (1984) Picosecond pulsed laser-induced melting and glass formation in metals. J Non-Cryst Solids 61–62:767
Lin Z, Zhigilei LV, Celli V (2008a) Electron-phonon coupling and electron heat capacity of metals under conditions of strong electron-phonon nonequilibrium. Phys Rev B 77:075133
Lin Z, Johnson RA, Zhigilei LV (2008b) Computational study of the generation of crystal defects in a bcc metal target irradiated by short laser pulses. Phys Rev B 77:214108
Lin Z, Leveugle E, Bringa EM, Zhigilei LV (2010) Molecular dynamics simulation of laser melting of nanocrystalline Au. J Phys Chem C 114:5686
Lindner B, Seydel U (1985) Laser desorption mass spectrometry of nonvolatiles under shock wave conditions. Anal Chem 57:895
Lipp VP, Rethfeld B, Garcia ME, Ivanov DS (2014) Atomistic-continuum modeling of short laser pulse melting of Si targets. Phys Rev B 90:245306
Lomonosov A, Mayer AP, Hess P (2001) Laser-based surface acoustic waves in materials science. In: Levy M, Bass HE, Stern R (eds) Experimental methods in the physical sciences. Academic, New York
Lorazo P, Lewis LJ, Meunier M (2006) Thermodynamic pathways to melting, ablation, and solidification in absorbing solids under pulsed laser irradiation. Phys Rev B 73:134108
Lu Y, Chen SC (2003) Nanopatterning of a silicon surface by near-field enhanced laser irradiation. Nanotechnology 14:505
Lu HM, Jiang Q (2005) Surface tension and its temperature coefficient for liquid metals. J Phys Chem B 109:15463
Lu K, Li Y (1998) Homogeneous nucleation catastrophe as a kinetic stability limit for superheated crystal. Phys Rev Lett 80:4474
Lu Y, Zhang H, Liu F (2005) UV–visible reflectance spectra of nanocrystalline silver compacted under different pressures. Phys Lett A 342:351
Luo S-N, Ahrens TJ, Çağın T, Strachan A, Goddard WA, Swift DC (2003) Maximum superheating and undercooling: systematics, molecular dynamics simulations, and dynamic experiments. Phys Rev B 68:134206
Ma X, Zhang Y, Lei H-R, Kenttämaa HI (2019) Laser-induced acoustic desorption. MRS Bull 44:372
MacDonald CA, Malvezzi AM, Spaepen F (1989) Picosecond time-resolved measurements of crystallization in noble metals. J Appl Phys 65:129
Manzo AJ, Helvajian H (2014) Demonstration of enhanced surface mobility of adsorbate cluster species by surface acoustic wave excitation induced by a pulsed laser. Proc SPIE 8969:896908
Margetic V, Niemax K, Hergenröder R (2003) Application of femtosecond laser ablation time-of-flight mass spectrometry to in-depth multilayer analysis. Anal Chem 75:3435

Marla D, Bhandarkar UV, Joshi SS (2014) A model of laser ablation with temperature-dependent material properties, vaporization, phase explosion and plasma shielding. Appl Phys A Mater Sci Process 116:273

Martynyuk MM (1974) Vaporization and boiling of liquid metal in an exploding wire. Sov Phys Tech-Phys 19:793

Martynyuk MM (1977) Phase explosion of a metastable fluid. Combust Explos Shock Waves 13:178

Martynyuk MM (1983) Critical constants of metals. Russ J Phys Chem 57:494

Mavrikakis M, Hammer B, Nørskov JK (1998) Effect of strain on the reactivity of metal surfaces. Phys Rev Lett 81:2819

Mazevet S, Clérouin J, Recoules V, Anglade PM, Zerah G (2005) Ab-Initio simulations of the optical properties of warm dense gold. Phys Rev Lett 95:085002

Mazzi A, Miotello A (2017) Simulation of phase explosion in the nanosecond laser ablation of aluminum. J Colloid Interface Sci 489:126

Mazzi A, Gorrini F, Miotello A (2015) Liquid nanodroplet formation through phase explosion mechanism in laser-irradiated metal targets. Phys Rev E 92:031301

Mazzi A, Gorrini F, Miotello A (2017) Dynamics of liquid nanodroplet formation in nanosecond laser ablation of metals. Appl Surf Sci 418:601

Mazzi A, Orlandi M, Patel N, Miotello A (2018) Laser-inducing extreme thermodynamic conditions in condensed matter to produce nanomaterials for catalysis and the photocatalysis. In: Ossi PM (ed) Advances in the application of lasers in materials science. Springer International Publishing, Cham, p 89

Melia MA, Serron ML, Florian DC, Weiler JP, Scully JR, Fitz-Gerald JM (2016) Excimer laser processing of cast Mg-Al-Zn (AZ91D) and Mg-Al (AM60B) alloys for improved corrosion resistance. Corrosion 72:1580

Melia MA, Florian DC, Steuer FW, Briglia BF, Purzycki MK, Scully JR, Fitz-Gerald JM (2017) Investigation of critical processing parameters for laser surface processing of AZ31B-H24. Surf Coat Tech 325:157

Merabia S, Shenogin S, Joly L, Keblinski P, Barrat J-L (2009a) Heat transfer from nanoparticles: a corresponding state analysis. Proc Natl Acad Sci U S A 106:15113

Merabia S, Keblinski P, Joly L, Lewis LJ, Barrat J-L (2009b) Critical heat flux around strongly heated nanoparticles. Phys Rev E 79:021404

Meyers MA, Mishra A, Benson DJ (2006) Mechanical properties of nanocrystalline materials. Prog Mater Sci 51:427

Miller GF, Pursey H (1955) On the partition of energy between elastic waves in a semi-infinite solid. Proc R Soc London Ser A 233:55

Miotello A, Kelly R (1995) Critical assessment of thermal models for laser sputtering at high fluences. Appl Phys Lett 67:3535

Miotello A, Kelly R (1999) Laser-induced phase explosion: new physical problems when a condensed phase approaches the thermodynamic critical temperature. Appl Phys A Mater Sci Process 69:S67

Mishin Y (2004) Atomistic modeling of the γ and γ'-phases of the Ni–Al system. Acta Mater 52:1451

Mo MZ et al (2018) Heterogeneous to homogeneous melting transition visualized with ultrafast electron diffraction. Science 360:1451

Molian PA (1989) Surface alloying using lasers. In: Sudarshan TS (ed) Surface modification technologies. Marcel Dekker, New York, p 421

Møller SH, Eriksen EH, Tønning PL, Jensen PB, Chevallier J, Balling P (2018) Femtosecond-laser-induced modifications of $Ge_2Sb_2Te_5$ thin films: permanent optical change without amorphization. Appl Surf Sci 476:221

Morozov AA (2004) Thermal model of pulsed laser ablation: back flux contribution. Appl Phys A Mater Sci Process 79:997

Morozov AA (2006) Back flux at polyatomic gas expansion for pulsed laser evaporation. Appl Surf Sci 252:2978
Murray PT, Shin E (2008) Formation of silver nanoparticles by through thin film ablation. Mater Lett 62:4336
Naghilou A, He M, Schubert JS, Zhigilei LV, Kautek W (2019) Femtosecond laser generation of microbumps and nanojets on single and stacked Cu/Ag thin films. Phys Chem Chem Phys 21:11846
Naghilou A, Armbruster O, Kautek W (2020) Laser-induced non-thermal processes. In: Handbook of laser micro- and nano-engineering. Springer, Cham
Narasaki T (1983) The effect of temperature gradient on the motion of a bubble in reduced gravity. Adv Space Res 3:137
Nerushev OA, Sukhinin GI (1995) Kinetics of fullerene formation by electric-arc vaporization of graphite (in Russian). Pisma Zh Tekh Fiz 21:50
Nishiyama H, Saito N, Chou H, Sato K, Inoue Y (1999) Effects of surface acoustic waves on adsorptive properties of ZnO and NiO thin films deposited on ferroelectric substrates. Surf Sci 433–435:525
Nishiyama H, Rattana N, Saito N, Sato K, Inoue Y (2000) Effects of Rayleigh surface acoustic wave upon adsorptive and surface properties of a thin NiO film. J Phys Chem B 104:10602
Nørskov JK, Bligaard T, Hvolbæk B, Abild-Pedersen F, Chorkendorff I, Christensen CH (2008) The nature of the active site in heterogeneous metal catalysis. Chem Soc Rev 37:2163
Oguz Er A, Chen J, Tang J, Rentzepis PM (2012) Coherent acoustic wave oscillations and melting on Ag(111) surface by time resolved x-ray diffraction. Appl Phys Lett 100:151910
Osipov VV, Platonov VV, Lisenkov VV, Tikhonov EV, Podkin AV (2018) Study of nanoparticle production from yttrium oxide by pulse-periodic radiation of ytterbium fibre laser. Appl Phys A Mater Sci Process 124:3
Paltauf G, Dyer PE (2003) Photomechanical processes and effects in ablation. Chem Rev 103:487
Pan QY, Huang WD, Lin X, Zhou YH (1997) Primary spacing selection of Cu-Mn alloy under laser rapid solidification condition. J Cryst Growth 181:109
Pan QY, Lin X, Huang WD, Zhou YH, Zhang GL (1998) Microstructure evolution of Cu–Mn alloy under laser rapid solidification conditions. Mater Res Bull 33:1621
Papadopoulou EL, Barberoglou M, Zorba V, Manousaki A, Pagkozidis A, Stratakis E, Fotakis C (2009) Reversible photoinduced wettability transition of hierarchical ZnO structures. J Phys Chem C 113:2891
Picard YN, Adams DP, Yalisove SM (2004) Femtosecond laser interactions with Co/Al multilayer films. MRS Proc 850. MM1.9
Pitsillides CM, Joe EK, Wei X, Anderson RR, Lin CP (2003) Selective cell targeting with light-absorbing microparticles and nanoparticles. Biophys J 84:4023
Polushkin NI, Oliveira V, Vilar R, He M, Shugaev MV, Zhigilei LV (2018) Phase-change magnetic memory: rewritable ferromagnetism by laser quenching of chemical disorder in $Fe_{60}Al_{40}$ alloy. Phys Rev Appl 10:024023
Porneala C, Willis DA (2009) Time-resolved dynamics of nanosecond laser-induced phase explosion. J Phys D 42:155503
Prokhorov AM, Konov VI, Ursu I, Mihailescu IN (1990) Laser heating of metals. Adam Hilger, Bristol/Philadelphia/New York
Pronko PP, Dutta SK, Squier J, Rudd JV, Du D, Mourou G (1995) Machining of sub-micron holes using a femtosecond laser at 800 nm. Opt Commun 114:106
Pudell J, Maznev AA, Herzog M, Kronseder M, Back CH, Malinowski G, von Reppert A, Bargheer M (2018) Layer specific observation of slow thermal equilibration in ultrathin metallic nanostructures by femtosecond X-ray diffraction. Nat Commun 9:3335
Pustovalov VK, Smetannikov AS, Zharov VP (2008) Photothermal and accompanied phenomena of selective nanophotothermolysis with gold nanoparticles and laser pulses. Laser Phys Lett 5:775

Qiu TQ, Tien CL (1994) Femtosecond laser heating of multi-layer metals – I. Analysis. Int J Heat Mass Transf 37:2789
Qiu TQ, Juhasz T, Suarez C, Bron WE, Tien CL (1994) Femtosecond laser heating of multi-layer metals – II. Experiments. Int J Heat Mass Transf 37:2799
Ratsch C, Seitsonen AP, Scheffler M (1997) Strain dependence of surface diffusion: Ag on Ag(111) and Pt(111). Phys Rev B 55:6750
Reese SJ, Hurley DH, Rollins HW (2006) Effect of surface acoustic waves on the catalytic decomposition of ethanol employing a comb transducer for ultrasonic generation. Ultrason Sonochem 13:283
Reif J, Varlamova O, Costache F (2008) Femtosecond laser induced nanostructure formation: self-organization control parameters. Appl Phys A Mater Sci Process 92:1019
Rethfeld B, Sokolowski-Tinten K, von der Linde D, Anisimov SI (2002) Ultrafast thermal melting of laser-excited solids by homogeneous nucleation. Phys Rev B 092103:65
Roland C, Gilmer GH (1992) Epitaxy on surfaces vicinal to Si(001). I. Diffusion of silicon adatoms over the terraces. Phys Rev B 46:13428
Rosenberg R (2005) Why ice is slippery?. Phys Today 58:50
Rousse A et al (2001) Non-thermal melting in semiconductors measured at femtosecond resolution. Nature 410:65
Saeta P, Wang JK, Siegal Y, Bloembergen N, Mazur E (1991) Ultrafast electronic disordering during femtosecond laser melting of GaAs. Phys Rev Lett 67:1023
Saito N, Nishiyama H, Inoue Y (2001) Acoustic wave effects on catalysis: design of surfaces with artificially controllable functions for chemical reactions. Appl Surf Sci 169–170:259
Savolainen J-M, Christensen MS, Balling P (2011) Material swelling as the first step in the ablation of metals by ultrashort laser pulses. Phys Rev B 84:193410
Schmera G, Kish LB (2003) Surface diffusion enhanced chemical sensing by surface acoustic waves. Sensors Actuators B Chem 93:159
Schmidt H, Ihlemann J, Wolff-Rottke B, Luther K, Troe J (1998) Ultraviolet laser ablation of polymers: spot size, pulse duration, and plume attenuation effects explained. J Appl Phys 83:5458
Schmidt V, Husinsky W, Betz G (2000) Dynamics of laser desorption and ablation of metals at the threshold on the femtosecond time scale. Phys Rev Lett 85:3516
Schroeder M, Wolf DE (1997) Diffusion on strained surfaces. Surf Sci 375:129
Sedao X, Maurice C, Garrelie F, Colombier J-P, Reynaud S, Quey R, Pigeon F (2014a) Influence of crystal orientation on the formation of femtosecond laser-induced periodic surface structures and lattice defects accumulation. Appl Phys Lett 104:171605
Sedao X, Maurice C, Garrelie F, Colombier J-P, Reynaud S, Quey R, Blanc G, Pigeon F (2014b) Electron backscatter diffraction characterization of laser-induced periodic surface structures on nickel surface. Appl Surf Sci 302:114
Sedao X et al (2016) Growth twinning and generation of high-frequency surface nanostructures in ultrafast laser-induced transient melting and resolidification. ACS Nano 10:6995
Semerok A, Dutouquet C (2004) Ultrashort double pulse laser ablation of metals. Thin Solid Films 453–454:501
Shank CV, Yen R, Hirlimann C (1983) Femtosecond-time-resolved surface structural dynamics of optically excited silicon. Phys Rev Lett 51:900
Shih C-Y, Shugaev MV, Wu C, Zhigilei LV (2017) Generation of subsurface voids, incubation effect, and formation of nanoparticles in short pulse laser interactions with bulk metal targets in liquid: molecular dynamics study. J Phys Chem C 121:16549
Shih C-Y et al (2018) Two mechanisms of nanoparticle generation in picosecond laser ablation in liquids: the origin of the bimodal size distribution. Nanoscale 10:6900
Shugaev MV, Bulgakova NM (2010) Thermodynamic and stress analysis of laser-induced forward transfer of metals. Appl Phys A Mater Sci Process 101:103
Shugaev MV, Zhigilei LV (2019) Thermodynamic analysis and atomistic modeling of subsurface cavitation in photomechanical spallation. Comput Mater Sci 166:311

Shugaev MV, Zhigilei LV (in preparation)
Shugaev MV, Manzo AJ, Wu C, Zaitsev VY, Helvajian H, Zhigilei LV (2015) Strong enhancement of surface diffusion by nonlinear surface acoustic waves. Phys Rev B 91:235450
Shugaev MV, Shih C-Y, Karim ET, Wu C, Zhigilei LV (2017a) Generation of nanocrystalline surface layer in short pulse laser processing of metal targets under conditions of spatial confinement by solid or liquid overlayer. Appl Surf Sci 417:54
Shugaev MV, Gnilitskyi I, Bulgakova NM, Zhigilei LV (2017b) Mechanism of single-pulse ablative generation of laser-induced periodic surface structures. Phys Rev B 96:205429
Shugaev MV, He M, Lizunov SA, Levy Y, Derrien TJY, Zhukov VP, Bulgakova NM, Zhigilei LV (2018) Insights into laser-materials interaction through modeling on atomic and macroscopic scales. In: Ossi PM (ed) Advances in the application of lasers in materials science. Springer International Publishing, Cham, p 107
Shugaev MV, Wu C, Zaitsev VY, Zhigilei LV (2020) Molecular dynamics modeling of nonlinear propagation of surface acoustic waves. J Appl Phys 128:045117
Sibold D, Urbassek HM (1993) Monte Carlo study of Knudsen layers in evaporation from elemental and binary media. Phys Fluids A 5:243
Siders CW et al (1999) Detection of nonthermal melting by ultrafast X-ray diffraction. Science 286:1340
Siems A, Weber SAL, Boneberg J, Plech A (2011) Thermodynamics of nanosecond nanobubble formation at laser-excited metal nanoparticles. New J Phys 13:043018
Silvestrelli PL, Alavi A, Parrinello M, Frenkel D (1996) Ab initio molecular dynamics simulation of laser melting of silicon. Phys Rev Lett 77:3149
Sipe JE, Young JF, Preston JS, van Driel HM (1983) Laser-induced periodic surface structure. I. Theory. Phys Rev B 27:1141
Siwick BJ, Dwyer JR, Jordan RE, Miller RJD (2003) An atomic-level view of melting using femtosecond electron diffraction. Science 302:1382
Skirtach AG, Dejugnat C, Braun D, Susha AS, Rogach AL, Parak WJ, Möhwald H, Sukhorukov GB (2005) The role of metal nanoparticles in remote release of encapsulated materials. Nano Lett 5:1371
Skripov VP, Kondor R, Slutzkin D (1974) Metastable liquids. Wiley/Israel Program for Scientific Translations, New York/Chichester/Jerusalem/London
Smoluchowski M (1916) Drei vorträge über diffusion, brownsche molekularbewegung und koagulation von kolloidteilchen (in German). Phys Z 17:557
Sokolowski-Tinten K, Bialkowski J, Boing M, Cavalleri A, von der Linde D (1998) Thermal and nonthermal melting of gallium arsenide after femtosecond laser excitation. Phys Rev B 58:R11805
Spaepen FA, Lin C-J (1984) Partitionless crystallization and glass formation in Fe-B alloys during picosecond pulsed laser quenching. In: von Allmen M (ed) Amorphous metals and non-equilibrium processing. Les Editions de Physique, Les Ulis
Spaepen F, Turnbull D (1979) Kinetics of motion of crystal-melt interfaces. AIP Conf Proc 50:73
Starikov SV, Pisarev VV (2015) Atomistic simulation of laser-pulse surface modification: predictions of models with various length and time scales. J Appl Phys 117:135901
Starinskiy SV, Shukhov YG, Bulgakov AV (2016) Dynamics of pulsed laser ablation of gold in vacuum in the regime of nanostructured film synthesis. Tech Phys Lett 42:411
Stevens RJ, Zhigilei LV, Norris PM (2007) Effects of temperature and disorder on thermal boundary conductance at solid–solid interfaces: nonequilibrium molecular dynamics simulations. Int J Heat Mass Transf 50:3977
Stolk PA, Polman A, Sinke WC (1993) Experimental test of kinetic theories for heterogeneous freezing in silicon. Phys Rev B 47:5
Su SS, Chang I (2018) Review of production routes of nanomaterials. In: Brabazon D et al. (eds) Commercialization of nanotechnologies – a case study approach. Springer International Publishing AG, Cham, p 15
Sun DY, Asta M, Hoyt JJ (2004) Kinetic coefficient of Ni solid-liquid interfaces from molecular-dynamics simulations. Phys Rev B 69:024108

Thomas DA, Lin Z, Zhigilei LV, Gurevich EL, Kittel S, Hergenröder R (2009) Atomistic modeling of femtosecond laser-induced melting and atomic mixing in Au film – Cu substrate system. Appl Surf Sci 255:9605
Trudeau ML, Ying JY (1996) Nanocrystalline materials in catalysis and electrocatalysis: structure tailoring and surface reactivity. Nanostruct Mater 7:245
Tsao JY, Aziz MJ, Thompson MO, Peercy PS (1986) Asymmetric melting and freezing kinetics in silicon. Phys Rev Lett 56:2712
Turnbull D (1962) On the relation between crystallization rate and liquid structure. J Phys Chem 66:609
Turnbull D (1981) Metastable structures in metallurgy. Metall Trans A 12:695
Turnbull D, Cech RE (1950) Microscopic observation of the solidification of small metal droplets. J Appl Phys 21:804
Turnbull D, Fisher JC (1949) Rate of nucleation in condensed systems. J Chem Phys 17:71
Upadhyay AK, Inogamov NA, Rethfeld B, Urbassek HM (2008) Ablation by ultrashort laser pulses: atomistic and thermodynamic analysis of the processes at the ablation threshold. Phys Rev B 78:045437
Valiev RZ, Alexandrov IV, Zhu YT, Lowe TC (2002) Paradox of strength and ductility in metals processed by severe plastic deformation. J Mater Res 17:5
van der Veen JF (1999) Melting and freezing at surfaces. Surf Sci 1:433–435
Vilar R (2020) Microstructure modification: generation of crystal defects and phase transformations. In: Handbook of laser micro- and nano-engineering. Springer, Cham
Vincenc Oboňa J, Ocelík V, Rao JC, Skolski JZP, Römer GRBE, Huis in 't Veld AJ, Hosson JTMD (2014) Modification of Cu surface with picosecond laser pulses. Appl Surf Sci 303:118
Viswanath DS, Kuloor NR (1966) Latent heat of vaporization, surface tension, and temperature. J Chem Eng Data 11:69
Volkov AN, Sevilla C, Zhigilei LV (2007) Numerical modeling of short pulse laser interaction with Au nanoparticle surrounded by water. Appl Surf Sci 253:6394
Volmer M, Weber A (1926) Nucleation of supersaturated structures. Z Phys Chem 119:277
von Allmen M, Blatter A (1998) Laser beam interactions with materials. Springer, Berlin
von Helden G, Hsu MT, Gotts N, Bowers MT (1993) Carbon cluster cations with up to 84 atoms: structures, formation mechanism, and reactivity. J Phys Chem 97:8182
Vorobyev AY, Guo C (2005) Enhanced absorptance of gold following multipulse femtosecond laser ablation. Phys Rev B 72:195422
Vorobyev AY, Guo C (2007) Effects of nanostructure-covered femtosecond laser-induced periodic surface structures on optical absorptance of metals. Appl Phys A Mater Sci Process 86:321
Vorobyev AY, Guo C (2008a) Femtosecond laser blackening of platinum. J Appl Phys 104:053516
Vorobyev AY, Guo C (2008b) Colorizing metals with femtosecond laser pulses. Appl Phys Lett 92:041914
Vorobyev AY, Guo C (2009) Metal pumps liquid uphill. Appl Phys Lett 94:224102
Vorobyev AY, Guo C (2010) Laser turns silicon superwicking. Opt Express 18:6455
Wang W, Cahill DG (2012) Limits to thermal transport in nanoscale metal bilayers due to weak electron-phonon coupling in Au and Cu. Phys Rev Lett 109:175503
Wang J, Li J, Yip S, Wolf D, Phillpot S (1997) Unifying two criteria of Born: Elastic instability and melting of homogeneous crystals. Physica A 240:396
Wang H, Pyatenko A, Kawaguchi K, Li X, Swiatkowska-Warkocka Z, Koshizaki N (2010) Selective pulsed heating for the synthesis of semiconductor and metal submicrometer spheres. Angew Chem Int Ed 49:6361
Wang Y, Lu Z, Ruan X (2016) First principles calculation of lattice thermal conductivity of metals considering phonon-phonon and phonon-electron scattering. J Appl Phys 119:225109
Watanabe Y, Inoue Y, Sato K (1996) Activation of a thin film Pd catalyst for CO and ethanol oxidation by surface acoustic waves. Surf Sci 357–358:769
Watson KM (1943) Thermodynamics of the liquid state. Ind Eng Chem 35:398

Wellershoff S-S, Hohlfeld J, Güdde J, Matthias E (1999) The role of electron–phonon coupling in femtosecond laser damage of metals. Appl Phys A Mater Sci Process 69:S99
Williamson S, Mourou G, Li JCM (1984) Time-resolved laser-induced phase transformation in aluminum. Phys Rev Lett 52:2364
Woychik CG, Lowndes DH, Massalski TB (1985) Solidification structures in melt-spun and pulsed laser-quenched Cu-Ti alloys. Acta Metall 33:1861
Wu MW, Metiu H (2000) The effect of strain on the adsorption of CO on Pd(100). J Chem Phys 113:1177
Wu C, Zhigilei LV (2014) Microscopic mechanisms of laser spallation and ablation of metal targets from large-scale molecular dynamics simulations. Appl Phys A Mater Sci Process 114:11
Wu C, Zhigilei LV (2016) Nanocrystalline and polyicosahedral structure of a nanospike generated on metal surface irradiated by a single femtosecond laser pulse. J Phys Chem C 120:4438
Wu C, Thomas DA, Lin Z, Zhigilei LV (2011) Runaway lattice-mismatched interface in an atomistic simulation of femtosecond laser irradiation of Ag film–Cu substrate system. Appl Phys A Mater Sci Process 104:781
Wu C, Zaitsev VY, Zhigilei LV (2013) Acoustic enhancement of surface diffusion. J Phys Chem C 117:9252
Wu C, Karim ET, Volkov AN, Zhigilei LV (2014) Atomic movies of laser-induced structural and phase transformations from molecular dynamics simulations. In: Castillejo M, Ossi PM, Zhigilei L (eds) Lasers in materials science. Springer International Publishing, Cham, p 67
Wu C, Christensen MS, Savolainen J-M, Balling P, Zhigilei LV (2015) Generation of subsurface voids and a nanocrystalline surface layer in femtosecond laser irradiation of a single-crystal Ag target. Phys Rev B 91:035413
Xu X, Chen G, Song KH (1999) Experimental and numerical investigation of heat transfer and phase change phenomena during excimer laser interaction with nickel. Int J Heat Mass Transf 42:1371
Yang S, Wang ZJ, Kokawa H, Sato YS (2007) Grain boundary engineering of 304 austenitic stainless steel by laser surface melting and annealing. J Mater Sci 42:847
Yeo LY, Friend JR (2014) Surface acoustic wave microfluidics. Annu Rev Fluid Mech 46:379
Yoo JH, Jeong SH, Greif R, Russo RE (2000) Explosive change in crater properties during high power nanosecond laser ablation of silicon. J Appl Phys 88:1638
Yoshiki N, Tatsuo O, Mitsuo M (2003) Nano-sized hollow bump array generated by single femtosecond laser pulse. Jpn J Appl Phys 42:L1452
Zeldovich YB, Raizer YP (1966) Physics of shock waves and high temperature hydrodynamics phenomena. Academic, New York
Zeng X, Mao XL, Greif R, Russo RE (2005) Experimental investigation of ablation efficiency and plasma expansion during femtosecond and nanosecond laser ablation of silicon. Appl Phys A Mater Sci Process 80:237
Zhang D, Gökce B, Barcikowski S (2017) Laser synthesis and processing of colloids: fundamentals and applications. Chem Rev 117:3990
Zhao Q-Z, Malzer S, Wang L-J (2007) Self-organized tungsten nanospikes grown on sub-wavelength ripples induced by femtosecond laser pulses. Opt Express 15:15741
Zharov VP, Mercer KE, Galitovskaya EN, Smeltzer MS (2006) Photothermal nanotherapeutics and nanodiagnostics for selective killing of bacteria targeted with gold nanoparticles. Biophys J 90:619
Zhigilei LV (2003) Dynamics of the plume formation and parameters of the ejected clusters in short-pulse laser ablation. Appl Phys A Mater Sci Process 76:339
Zhigilei LV, Garrison BJ (2000) Microscopic mechanisms of laser ablation of organic solids in the thermal and stress confinement irradiation regimes. J Appl Phys 88:1281
Zhigilei LV, Helvajian H (2019) Acoustic processes in materials. MRS Bull 44:345
Zhigilei LV, Ivanov DS (2005) Channels of energy redistribution in short-pulse laser interactions with metal targets. Appl Surf Sci 248:433

Zhigilei LV, Ivanov DS, Leveugle E, Sadigh B, Bringa EM (2004) Computer modeling of laser melting and spallation of metal targets. Proc SPIE 5448:505

Zhigilei LV, Lin Z, Ivanov DS (2009) Atomistic modeling of short pulse laser ablation of metals: connections between melting, spallation, and phase explosion. J Phys Chem C 113:11892

Zhigilei LV, Lin Z, Ivanov DS, Leveugle E, Duff WH, Thomas D, Sevilla C, Guy SJ (2010) Atomic/molecular-level simulations of laser-materials interactions. In: Miotello A, Ossi PM (eds) Laser-surface interactions for new materials production: tailoring structure and properties. Springer, New York, p 43

Ziefuß AR, Reichenberger S, Rehbock C, Chakraborty I, Gharib M, Parak WJ, Barcikowski S (2018) Laser fragmentation of colloidal gold nanoparticles with high-intensity nanosecond pulses is driven by a single-step fragmentation mechanism with a defined educt particle-size threshold. J Phys Chem C 122:22125

Zier T, Zijlstra ES, Kalitsov A, Theodonis I, Garcia ME (2015) Signatures of nonthermal melting. Struct Dyn 2:054101

Zinovev AV, Veryovkin IV, Moore JF, Pellin MJ (2007) Laser-driven acoustic desorption of organic molecules from back-irradiated solid foils. Anal Chem 79:8232